# Photorefractive Photonics and Beyond (PR24)

## Interaction of Light with Matter

2-5 July, 2024

# PR24 Proceedings

Palacio de los Infantes | Euroforum

C. del Rey, 38, 28200 San Lorenzo of El Escorial, Madrid

UAM Universidad Autónoma de Madrid

POLITÉCNICA UNIVERSIDAD POLITÉCNICA DE MADRID

CSIC Consejo Superior de Investigaciones Científicas

# Photorefractive Photonics and Beyond (PR24)

## Interaction of Light with Matter

### 2-5 July, 2024

## Scientific Organizing Committee:

- Mercedes Carrascosa (Univ Autónoma de Madrid)
- Ángel García-Cabañes (Univ Autónoma de Madrid)
- Patricia Haro González (Univ Autónoma de Madrid)
- Pablo Molina (Univ Autónoma de Madrid)
- Mercedes Hernando-Pérez (Univ Autónoma de Madrid)
- Angel Alcázar de Velasco, (Univ. Politécnica de Madrid)
- Olga Caballero, Instituto de Micro y Nanotecnología (CSIC)

## International Advisory Board:

- Ali Adibi, Georgia Inst. of Technol., Atlanta (USA)
- Dana Anderson, JILA, Univ. Colorado, Boulder (USA)
- Mercedes Carrascosa Rico, Univ. Autónoma de Madrid (Spain)
- Roger Cudney, CICESE, Ensenada (Mexico)
- Michael Damzen, Imperial College London (UK)
- Cornelia Denz, IAP, Univ. Münster (Germany)
- Dean Evans, Air Force Research Laboratory, Dayton (USA)
- Lambertus Hesselink, Stanford University, Stanford (USA)
- Jean-Pierre Huignard, JPHOpto, Paris (France)
- Mirco Imlau, Univ. Osnabrück (Germany)
- Mojca Jazbinsek, ZHAW, Zurich (Switzerland)
- Detlef Kip, Helmut Schmidt University, Hamburg (Germany)
- Marvin Klein, Intelligent Optical Systems, Torrance (USA)
- Wieslaw Krolikowsky, Australian National University, Canberra (Australia)
- Germano Montemezzani, Université de Lorraine (France)
- David Nolte, Purdue University, West Lafayette (USA)
- Gilles Pauliat, Institut d’Optique Graduate School, Paris (France)
- Demetri Psaltis, EPFL Lausanne (Switzerland)
- Tsutomu Shimura, Univ. of Tokyo (Japan)
- Guoquan Zhang, Nankai University (China)
- Marco Bazzan, University of Padova (Italy)

# Sponsors

M.I. AYUNTAMIENTO
SAN LORENZO DE EL ESCORIAL

UAM | IfiMAC Condensed Matter Physics Center | EXCELENCIA MARÍA DE MAEZTU

DPTO. DE FÍSICA DE MATERIALES
Universidad Autónoma de Madrid

iberoptics
sistemas ópticos

CASIO
División Educativa

izasa
scientific
a werfen company

# Scientific Program

## Tuesday, July 2

| Time | Schedule |
|---|---|
| 16:00 - 20:00h | **Registration** |
| 20.00 | **Welcome party** |

# Wednesday, July 3

| Time | Schedule |
|---|---|
| **8:45 - 9:00 h** | **Opening** |
| **9:00 - 11:00 h** | **Session 1: Holography, imaging and optical processing and computing**<br>**Session chair: Prof. Marco Bazzan** |
| 9:00 -10:00 h | Plenary - 1<br>**David D. Nolte**<br>Holographic Optical Coherence Tomography for Personalized Medicine |
| 10:00 - 10:30 h | Invited talk - 1<br>**Carlos Antón**<br>Emergent materials for quantum photonics |
| 10:30 -10:45 h | Oral presentation - 1<br>**Dahuai Zheng**<br>Real-time Dynamic Holographic Display Based on LN Crystals |
| 10:45 -11:00 h | Oral presentation - 2<br>**Germano Montemezzani**<br>PR recording and nonlinear amplification of conical diffraction vector waves |
| 11.00 - 11:30 h | **COFFEE BREAK** |
| **11:30 - 13:00 h** | **Session 2: Photorefractive and photovoltaic effects and materials A**<br>**Session chair: Dr. Laura Vitadello** |
| 11:30 - 12.00 h | Invited talk - 2<br>**Yongfa Kong**<br>The Photorefraction of lithium niobate: from bulk to thin film |
| 12:00 - 12:15 h | Oral presentation - 3<br>**Marco Bazzan**<br>The thermo-photogalvanic effect in Fe:$LiNbO_3$ and its microscopic interpretation |
| 12:15 - 12:30 h | Oral presentation - 4<br>**Naoto Tsutsumi**<br>Photorefractivity and Transient Photoconductive Dynamics for Triphenylamine-Based Polymers |
| 12:30 - 12:45 h | Oral presentation - 5<br>**Al Grabar**<br>Photorefractive parameters of double-doped $Sn_2P_2S_6$ crystals. |
| 12:45 - 13:00 h | Oral presentation - 6<br>**Gabor Mandula**<br>Photorefractive effect and self-trapped-excitonic photochromism in stoichiometric Bi:Mg:$LiNbO_3$ |
| 13:00 - 14:30 h | **LUNCH** |

| Time | Schedule |
|---|---|
| **14:30 - 16:00 h** | **Session 3: Material micro- and nano engineering and integrated optics**<br>**Session chair: Prof. Germano Montemezzani** |
| 14:30 -15.00 h | Invited talk - 3<br>**Yan Sheng**<br>Nonlinear photonic crystals via all optical poling of ferroelectrics |
| 15:00 -15:15 h | Oral presentation - 7<br>**Carlos Sebastian**<br>Ferroelectric domain reversal in photovoltaic $LiNbO_3$ crystals driven by visible light |
| 15:15 - 15:30 h | Oral presentation - 8<br>**Jörg Imbrock**<br>Structured all-optical domain inversion in iron-doped lithium niobate |
| 15:30 -15:45 h | Oral presentation - 9<br>**Jiaxin Li**<br>Optical Stern-Gerlach effect in two non-parallel slab waveguides |
| 15:45 -16:00 h | Oral presentation - 10<br>**Sanbing Li**<br>N-type and p-type domain walls fabricated by atomic force microscopy |
| 16:00 - 16:30 h | **COFFEE BREAK** |
| 16:30 - 18:00 h | **Session 4: ...and beyond**<br>**Session chair: Prof. David D. Nolte** |
| 16:30 -17:00 h | Invited talk - 4<br>**Simonetta Grilli**<br>The pyroelectric effect in ferroelectric materials: new perspectives for biological applications |
| 17:00 -17:15 h | Oral presentation - 11<br>**Marta Quintanilla**<br>Control of plasmonic heating in biological media following all optical strategies |
| 17:15 -17:30 h | Oral presentation - 12<br>**Lisa Miccio**<br>Photovoltaic Interplay with living cells at Lithium Niobate interface |
| 17:30 -17:45 h | Oral presentation - 13<br>**Niklas Dömer**<br>Long-lived, pulse-induced absorption in $LiNb_{(1-x)}Ta_xO_3$ solid solutions |
| 17:45 -18:00 h | Oral presentation – 14<br>**Sponsor presentation – Izasa scientific** |
| 18:00 - 18:30 h | **COFFEE BREAK** |
| 18:30 - 20:00 h | **POSTER SESSION** |
| 20:00 h | **DINNER** |

# Thursday, July 4

| Time | Schedule |
|---|---|
| **8:45 - 11:00 h** | **Session 5: Non-Linear interaction of light with matter**<br>**Prof. Mathieu Chauvet** |
| 8:45 – 9:45 h | Plenary - 1<br>**Arnan Mitchell**<br>Non-Linear Photonics in $LiNbO_3$ and their applications |
| 9.45 -10:00 h | Oral presentation - 15<br>**Mariola Ramírez**<br>Ferroelectric Domain Control of Second Harmonic Generation in $MoS_2$-$LiNbO_3$ heterostructures |
| 10:00 - 13:00 h | **Visit to the Royal Monastery of San Lorenzo de El Escorial** |
| 13.00 - 14:30 h | **LUNCH** |
| **14:30 -15:30 h** | **Session 5: Non-Linear interaction of light with matter-CONT**<br>**Prof. Mathieu Chauvet** |
| 14:30 -14:45 h | Oral presentation - 16<br>**Tsutomu Shimura**<br>Enhancement of the second harmonic generation using Mie and photonic crystal resonance in Silicon surfaces |
| 14.45 - 15:00 h | Oral presentation - 17<br>**Laura Vittadello**<br>Nonlinear optical properties of low dimensional alkali niobates |
| 15:00 -15:15 h | Oral presentation - 18<br>**Felix Sauerwein**<br>Gap-free Tuning of Second and Third Harmonic Generation in Mechanochemically Synthesized nanocrystalline $LiNb_{1-x}Ta_xO_3$ Studied with Nonlinear Diffuse Femtosecond-Pulse Reflectometry |
| 15:15 - 15:30 h | |
| 15.30 - 16:00 h | **COFFEE BREAK** |

| Time | Schedule |
|---|---|
| **16:00 - 17:30 h** | **Session 6: Photorefractive and photovoltaic effects and materials B: applications**<br>**Session chair: Prof. Tsutomu Shimura** |
| 16:00 - 16:15 h | Oral presentation - 19<br>**Juan Wu**<br>Predator-prey behaviors in photorefractive solitons |
| 16:15- 16:30 h | Oral presentation - 20<br>**Takeo Sasaki**<br>Application of photorefractive liquid crystals to laser ultrasonics |
| 16:30- 16:45 h | Oral presentation - 21<br>**Adolfo Esteban-Martín**<br>Photorefractive optical transient detection with femtosecond pulses |
| 16:45 - 17:00 h | Oral presentation - 22<br>**Victor Reshetnyak - CANCELLED**<br>Two-beam energy exchange in a hybrid photorefractive ferroelectric liquid crystal cell |
| 17:00 - 17:15 h | Oral presentation - 23<br>**Nacera Bouldja**<br>Photorefractive deceleration of light pulses at the visible and infrared wavelengths |
| 17.15 – 17:45 h | **COFFEE BREAK** |
| **18:45 - 19:00 h** | **Session 7: Optical and photovoltaic micro-nano manipulation A**<br>**Session chair: Dr. Jörg Imbrock** |
| 17:45 -18:15 h | Invited talk - 5<br>**Hana Jungová**<br>Applications of light-driven nanomotors and deflecting metagratings in sensing and microscopy |
| 18:15 -18:30 h | Oral presentation - 24<br>**Manuel I. Marqués**<br>Magnetic control of electrically uncharged magneto-optical particles |
| 18:30 – 18:45 h | Oral presentation - 25<br>**Sebastian Cremaschini**<br>Optofluidic platform for the manipulation of water droplets on engineered Fe:LiNbO$_3$ surfaces |
| 18:45-19:00 h | Oral presentation - 26<br>**Riccardo Zamboni**<br>Photovoltaic opto-electrowetting using Fe:LiNbO$_3$ on artificially micropatterned surfaces |
| 19:00 -20:00 h | |
| 20.00 h | **CONFERENCE DINNER** |

# Friday, July 5

| Time | Schedule |
|---|---|
| **8:45 - 11:00 h** | **Session 8: Optical and photovoltaic micro-nano manipulation B**<br>**Session chair: Dr. Hana Jungová** |
| 8:45 - 9:45 h | Plenary - 3<br>**Cinzia Sada**<br>Surfing on the edge of exploring new perspectives: light-driven phenomena as a booster for new applications and scientific progress |
| 9.45 -10:00 h | Oral presentation - 27<br>**Athira Sadavisan**<br>Droplet manipulation on superhydrophobic surfaces enabled by electrostatic charge printing using Fe:LiNbO$_3$ |
| 10:00 - 10:15 h | Oral presentation - 28<br>**Giovanni Bragato / Cinzia Sada**<br>Integrated optofluidics on lithium niobate: effects of photo-induced electric fields on water droplets with dispersed micro-objects |
| 10:15 - 10:30 h | Oral presentation - 29<br>**Esther Rincon**<br>Exploring the electric charge of tumour spheroids through their manipulation on photovoltaic ferroelectric platforms |
| 10:30 -10:45 h | Oral presentation - 30<br>**Sara Coppola**<br>Pyro-electric and photorefractive effect for liquid manipulation and fabrication of 3D polymeric microneedles |
| 10:45 -11:00 h | Oral presentation - 31<br>**Fengchan Zhang**<br>Brownian motion governs the plasmonic enhancement of colloidal upconverting nanoparticles |
| 11.00 - 11:30 h | **COFFEE BREAK** |
| **11:30 - 13:00 h** | **Session 9: Material micro- and nano-engineering and integrated optics**<br>**Session chair: Dr. Lisa Miccio** |
| 11.30 - 12.00 h | Invited talk - 6<br>**Franzette Paz-Buclatin**<br>Design and fabrication of nanostructured diffractive microlenses inside optical crystals by 3D laser nanolithography |
| 12:00 - 12:15 h | Oral presentation - 32<br>**Yu Chen Zhang**<br>Photovoltaic effect in monocrystalline lithium niobate films with nanoscale thickness |

| Time | Schedule |
|---|---|
| 12:15 - 12:30 h | Oral presentation - 33<br>**Mathieu Chauvet**<br>Poling free high-contrast $LiNbO_3$ waveguides for nonlinear optical frequency conversions |
| 12:30 - 12:45 h | Oral presentation - 34<br>**Yuqi Zhang**<br>On-chip rare-earth doped lithium niobate waveguide amplifiers |
| 12:45 - 13:00 h | Oral presentation – 35<br>**Qianqian Kang**<br>Period-halving intensity oscillation in Floquet photonic structures |
| 13:00 -13:15 h | Closing ceremony |
| 13:15 - 14:30 h | **LUNCH** |

# Poster List

1. Accumulation of micro- and nano-plastics by electrohydrodynamic droplet dispensing for sensitive detection in salt-water**. P. Camarero.**

2. Small electron polarons bound to interstitial tantalum defects in lithium tantalate. **J. Koelmann.**

3. Exciton emissión enhancement in 1L-MoS2 on a ferroelectric substrate undergoing a ferro-to paraelectric phase transition. **D. Hernández-Pinilla**.

4. 2-photon polymerization of patterned polarizers in SU-8 and S1805 photoresist alignment surface **B. Ganazhapa**,.

5. Dynamics of a water droplet suspended in paraffin oil and subjected to a photovoltaic electric field**. A. Mendez**.

6. Lithium Niobate for Light-driven Actuation of Droplets. **A. Zaltron.**

7. Unlocking Single-Particle Multiparametric Sensing: Decoupling Temperature and Viscosity through Upconverting Polarized Spectroscopy. **E. Ortiz.**

8. Brownian motion governs the plasmonic enhancement of colloidal upconverting nanoparticles. **F. Zhang.**

9. Microscale Optical Forces: Exploring Size and Electrostatic Influences **A. Dávila.**

10. Submicro patterning in LiNbO3 by Fe ion implantation for the assessment of novel type of photovoltaic optoelectronic tweezers. **S. K. Padhi.**

11. Harnessing Plasmon Resonances in Ni and Bi2Te3 Nanowire Networks for Enhanced Thermoelectric Performance. **O. Caballero-Calero.**

12. Three-dimensionally nanostructured waveguides inside optical crystals for on-chip instrumentation by fs-laser nanolithography. **P. Molina**.

13. Dimensional analysis of Kukhtarev equations for the photorefractive effect. **A Alcazar**.

14. Imprinting micro-patterns of photovoltaic charge onto non-photovoltaic dielectric substrates. **C. Sebastián-Vicente.**

15. Anomalous small polarons mobility in defective oxides: the case of congruent lithium niobate. **L. Vittadello.**

16. Small polaron trapping kinetics in iron-doped congruent lithium niobate. **M. Bazzan.**

17. Exploring the electric charge of tumour spheroids through their manipulation on photovoltaic ferroelectric platforms. **E. Rincón.**

18. Optical control of ferroelectric liquids on ferroelectric solid substrates. **L. Lucchetti**.

# List of contributors

| **Presenting author** | **Affiliation** | **Country** | **Contribution** |
|---|---|---|---|
| **Alcázar, Ángel** | Universidad Politécnica de Madrid | Spain | **Poster 13** |
| **Antón, Carlos** | Universidad Autónoma de Madrid | Spain | **Invited 1** |
| **Bazzan, Marco** | Università di Padova | Italy | **Oral 3, Poster 17** |
| **Bouldja, Nacera** | CentraleSupélec, LMOPS | France | **Oral 23** |
| **Bragato, Giovanni** | University of Padova | Italy | **Oral 28** |
| **Caballero, Olga** | Instituto de Micro y Nanotecnología, CSIC | Spain | **Poster 11** |
| **Camarero, Pablo** | Universidad Autónoma de Madrid | Spain | **Poster 1** |
| **Chauvet, Mathieu** | University of Franche-Comté | France | **Oral 33** |
| **Coppola, Sara** | CNR-ISASI | Italy | **Oral 30** |
| **Cremaschini, Sebastian** | University of Padova | Italy | **Oral 25** |
| **Dávila, Ana** | Universidad Autónoma de Madrid | Spain | **Poster 9** |
| **Dömer, Niklas** | University of Osnabrueck | Germany | **Oral 13** |
| **Esteban-Martín, Adolfo** | Universitat de València | Spain | **Oral 21** |
| **Ganazhapa, Byron** | Universidad Politécnica de Madrid | Spain | **Poster 4** |
| **Grabar, Alexander** | Uzhhorod National University | Ukraine | **Oral 5** |
| **Grilli, Simonetta** | CNR-ISASI | Italy | **Invited 4** |
| **Hernández-Pinilla, David** | Universidad Autónoma de Madrid | Spain | **Poster 3** |
| **Imbrock, Jörg** | University of Münster | Germany | **Oral 8** |
| **Kang, Qianqian** | Nankai University | China | **Oral 35** |
| **Koelmann, Julian** | University of Osnabrück | Germany | **Poster 2** |
| **Kong, Yongfa** | Nankai University | China | **Invited 2** |
| **Li, Jiaxin** | Nankai University | China | **Oral 9** |
| **Li, Sanbing** | Nankai University | China | **Oral 10** |
| **Mandula, Gabor** | HUN-REN Wigner Research Centre for Physics | Hungary | **Oral 6** |
| **Marqués, Manuel I.** | Universidad Autónoma de Madrid | Spain | **Oral 24** |
| **Méndez, Angel** | Universidad Politécnica de Madrid | Spain | **Poster 5** |
| **Miccio, Lisa** | CNR-ISASI | Italy | **Oral 12** |
| **Mitchel, Arnan** | RMIT University | Australia | **Plenary 2** |
| **Molina, Pablo** | Universidad Autónoma de Madrid | Spain | **Poster 12** |
| **Montemezzani, Germano** | Université de Lorraine | France | **Oral 2** |
| **Nolte, David D.** | Purdue University | USA | **Plenary 1** |
| **Ortiz-Rivero, Elisa** | Universidad Autónoma de Madrid | Spain | **Poster 7** |
| **Padhi, Santanu K.** | Centro de Microanálisis de Materiales, UAM | Spain | **Poster 10** |
| **Paz-Buclatin, Franzette** | Universidad de La Laguna | Spain | **Invited 6** |
| **Quintanilla, Marta** | Universidad Autónoma de Madrid | Spain | **Oral 11** |
| **Ramírez, Mariola** | Universidad Autónoma de Madrid | Spain | **Oral 15** |
| **Reshetnyak, Victor** | Taras Shevchenko National University of Kyiv | Ukraine | **Oral 22** |
| **Rincón, Esther** | Universidad Autónoma de Madrid | Spain | **Oral 29, Poster 14** |
| **Sada, Cinzia** | University of Padova | Italy | **Plenary 3** |
| **Sadavisan, Athira** | University of Muenster | Germany | **Oral 27** |

| | | | |
|---|---|---|---|
| **Sasaki, Takeo** | Tokyo University of Science | Japan | **Oral 20** |
| **Sauerwein, Felix** | University of Osnabrueck | Germany | **Oral 18** |
| **Scientific, Izasa** | Sponsor | Spain | **Oral 14** |
| **Sebastián-Vicente, Carlos** | Universidad Autónoma de Madrid | Spain | **Oral 7, Poster 15** |
| **Sheng, Yan** | Ningbo University | China | **Invited 3** |
| **Shimura, Tsutomu** | University of Tokyo | Japan | **Oral 16** |
| **Šípová-Jungová, Hana** | Chalmers University of Technology | Sweden | **Invited 5** |
| **Tsutsumi, Naoto** | Kyoto Institute of Technology | Japan | **Oral 4** |
| **Vittadello, Laura** | University of Osnabrueck | Germany | **Oral 17, Poster 16** |
| **Wu, Juan** | Nankai University | China | **Oral 19** |
| **Zaltron, Anna Maria** | University of Padua | Italy | **Poster 6** |
| **Zamboni, Riccardo** | University of Münster | Germany | **Oral 26** |
| **Zhang, Fengchan** | Universidad Autónoma de Madrid | Spain | **Oral 32, Poster 8** |
| **Zhang, Fengchan** | Universidad Autónoma de Madrid | Spain | **Poster 8** |
| **Zhang, Yu Chen** | Nankai University | China | **Oral 32** |
| **Zhang, Yuqi** | Nankai University | China | **Oral 34** |
| **Zheng, Dahuai** | Nankai University | China | **Oral 1** |

# Holographic Optical Coherence Tomography for Personalized Medicine

David D. Nolte [a, b]

[a] Dept. of Physics and Astronomy, Purdue University, USA
[b] Animated Dynamics, Inc., USA

* nolte@epurdue.edu

The history of holography is dotted with moments of success separated by long stretches of uncertainty as holography struggled to find practical applications. This talk will set the stage for the pursuit of holographic applications by briefly outlining the early history of holography, notably the first practical demonstrations by Emmett Leith at the University of Michigan and photorefractive holography by Alastair Glass and others at Bell Labs [1].

Fast-forward to today and *low-coherence* holography has emerged with advantages for laser ranging applications such as optical coherence tomography (OCT). Holographic OCT was developed by Paul French at Imperial College and by myself at Purdue University in the late 1990’s. Initial applications used the ultra-low-intensity character of photorefractive quantum wells (PRQWs) to peer inside living biological tissues in an OCT format called holographic optical coherence *imaging* (HOCI). No *tomographic* reconstruction was required because the photorefractive Fourier-domain speckle holograms were read-out optically to a video camera for direct viewing.

However, the steady march of advances in digital cameras brought the moment, in the early 2000’s, when direct recording of holograms on the digital sensor plane provided higher signal-to-noise than photorefractive readout, and in 2007 we converted to digital holography for our OCT applications. The speed of the digital cameras, combined with the full-frame holographic acquisition of images from inside living tissue, allowed us to capture for the first time the dynamic contrast of light scattering from living tissue and to monitor the effects of therapeutic drugs [2]. This launched us down a path of holographic applications in biomedical optics as we developed the technique of ultra-low-frequency (ULF) Doppler spectroscopy of intracellular motions [3] based on holographic phase sensitivity.

Holographic OCT has now completed several pilot clinical trials in human cancer research in which we measured the likelihood that a patient would have a useful response to their prescribed chemotherapy. The trial results in human ovarian, esophageal, breast and blader cancers indicate that holographic OCT can steer cancer patients away from ineffective treatments, improving quality of life and overall survival. Commercial launch of this chemoresistance test is now being pursued.

There are also current and future research directions in microbiology. For instance, we use holographic OCT to monitor the infection of living tissue sentinels by pathogenic bacteria and viruses as microbe invasion and proliferation alter the cellular dynamics of the host sentinel tissue earlier than when they can be detected directly by light scattering. This would provide an “early warning” system that may improve survival of patients from sepsis. Other ongoing applications include drug development as well as applications in in-vitro fertilization (IVF), where holographic OCT is used to help select the most viable embryos.

*Acknowledgment:* This work was supported by the National Science Foundation grant CBET-2200186.

## References

[1] D. D. Nolte, *Interference: The history of optical interferometry and the scientists who tamed light*. Oxford, United Kingdom: Oxford University Press, 2023.
[2] K. Jeong, J. J. Turek, and D. D. Nolte, "Volumetric motility-contrast imaging of tissue response to cytoskeletal anti-cancer drugs," *Optics Express,* Article vol. 15, no. 21, pp. 14057-14064, Oct (2007)
[3] D. D. Nolte, "Coherent light scattering from cellular dynamics in living tissues," *Reports on Progress in Physics,* Review vol. 87, no. 3, Mar (2024), Art no. 036601

# Emergent materials for quantum photonics

Carlos Antón Solanas [a,*]

[a] Dep. Física de Materiales, Instituto Nicolás Cabrera, Instituto de Física de la Materia Condensada, Universidad Autónoma de Madrid, 28049 Madrid, Spain

*carlos.anton@uam.es

The control of light-matter interaction at the nanoscale constitutes an avenue for the discovery of new optoelectronic devices and applications. Many emergent materials are gaining prominence, providing novel properties and advantages in quantum information processing applications. Some of these candidates are quantum dots in transition metal dichalcogenides monolayers, defects in hexagonal boron nitride nanocrystals or even perovskite quantum dots. [1]

A fundamental element for the development of the quantum Internet is an efficient source of single photons, capable of emitting photons (1) deterministically or "at the push of a button", (2) one at a time, and (3) with all photons exhibiting identical properties (becoming indistinguishable photons). Obtaining this ideal quantum performance is tremendously challenging and requires a deep understanding of the properties of the quantum material, capable of behaving like an "artificial atom", i.e., confining a single electronic excitation, and delivering a single photon state after spontaneous emission. Controlling this spontaneous emission through light-matter interactions between the quantum emitter and an optical cavity is necessary to approach an optimal performance in single photon emission.

In the first part of the talk, I will discuss recent results to generate single photons based on atomically thin monolayers of $WSe_2$. The local stress in these monolayers produces a potential capable of trapping single excitons and thus producing single photon emission. These quantum dots can be easily coupled to Fabry-Pérot optical cavities, which improve the emitter performance and makes them state-of-the-art competitive sources of single photons. [2] First quantum communication testbed-applications with these emitters are being implemented, promising a “*bright future*” for these quantum photonic devices. [3]

In the last part of the talk, I will also show our experimental progress on another material platform: single defects in hexagonal boron nitride. This system, operating at ambient conditions, and interfaced with an optical cavity, is a suitable candidate in quantum optical applications, such as free-space quantum key distribution.

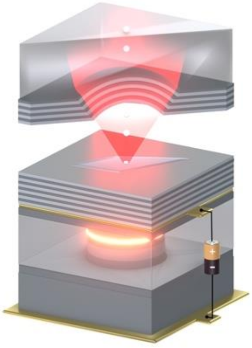

*Figure* – Schematic of the single photon device, composed by a quantum emitter embedded in an optical cavity.

## References

[1] M. Esmann, S. C. Wein, and C. Antón-Solanas, *Solid-State Single-Photon Sources: Recent Advances for Novel Quantum Materials*, Advanced Functional Materials **n/a**, 2315936 (2024).
[2] J.-C. Drawer et al., *Monolayer-Based Single-Photon Source in a Liquid-Helium-Free Open Cavity Featuring 65% Brightness and Quantum Coherence*, Nano Lett. **23**, 8683 (2023).
[3] T. Gao, M. von Helversen, C. Antón-Solanas, C. Schneider, and T. Heindel, *Atomically-Thin Single-Photon Sources for Quantum Communication*, Npj 2D Mater Appl **7**, 1 (2023).

# Real-time Dynamic Holographic Display Based on LN Crystals

Shuolin Wang [a], **Dahuai Zheng [a,*]**, Yuqi Zhang [a], Hongde Liu [a], Yongfa Kong [a], Jingjun Xu [a]

[a] MOE Key Laboratory of Weak-Light Nonlinear Photonics, TEDA Institute of Applied Physics and School of Physics, Nankai University, Tianjin 300457, China

* dhzheng@nankai.edu.cn

Real immersion experience makes three-dimensional (3D) display a huge market demand. The dreamed 3D display in future should be viewed without auxiliary wearing devices. Holographic 3D display has become an ultimate technique that can display the complete information of objects and bring people an unprecedented sense of presence. At the same time, the realization of holographic 3D display faces many difficulties and challenges, especially the lack of refreshable holographic materials. A real-time refresh of a video requires at least 25 frame per second, that is, the response time of the material should be less than 20 ms. The shorter of the response time, the higher of a refresh rate can be obtained, which is conducive to reducing the flicker of the screen, reducing the visual fatigue of the eyes, making the display more stable and smoother, and obtaining a better viewing experience. Here, a bismuth and magnesium co-doped lithium niobate (LN:Bi,Mg) crystal is reported, with a response time of 7.2 ms. The crystal has been used to demonstrate a real-time holographic display with a refresh rate of 60 Hz, as that of television. In addition, a reasonable calculation indicate that the electron mobility while Bi occupying Nb-site is significantly greater than that in Li-site, which directly induces the fast response of LN:Bi,Mg crystals when the concentration of Mg is above its doping threshold. This work provides an ideal candidate material for holographic 3D display and expands the technique for performance control of LN crystals.

## References

[1] D. Zheng, W. Wang, S. Wang, D. Qu, H. Liu, Y. Kong, S. Liu, S. Chen, R. Rupp and J. Xu, , Appl. Phys. Lett. 114:241903(2019).

[2] S. Wang, Y. Shan, W. Wang, D. Zheng, H. Liu, S. Liu, Y. Kong, J. Xu, Lone-pair electron effect induced a rapid photorefractive response in site-controlled LiNbO3:Bi,M (M = Zn, In, Zr) crystals, Appl. Phys. Lett. 118:191902(2021).

[3] S. Wang, Y. Shan, D. Zheng, S. Liu, F. Bo, H. Liu, Y. Kong, J. Xu, The real-time dynamic holographic display of LN:Bi,Mg crystals and defect-related electron mobility, Opto-Electron. Adv. 5:210135(2022).

# Photorefractive recording and nonlinear amplification of conical diffraction vector waves

**G. Montemezzani** [a,b], M. W. Iqbal [a,b], Y. Shiposh [c], A. Kohutych [c],
N. Marsal [a,b], and A. A. Grabar [c]

[a] Université de Lorraine, CentraleSupélec, LMOPS, 57000 Metz, France
[b] Chair in Photonics, CentraleSupélec, LMOPS, 57000 Metz, France
[c] Inst. for Solid State Physics and Chemistry, Uzhhorod National Univ., 88000 Uzhhorod, Ukraine

* germano.montemezzani@univ-lorraine.fr

Internal conical diffraction (CD) is a well-known linear optical effect observable upon focused-light propagation along an optic axis of an optically biaxial crystal (BC) [1,2]. In the standard configuration involving a unique BC and uniformly polarized input wave, CD creates a double circular ring with spatially varying linear polarization (vector wave), where two diametrically opposite points always possess orthogonal linear polarizations [1,2]. CD beams have recently demonstrated compelling capabilities for various applications in contemporary photonics, such as, optical trapping, free-space optical communication, super-resolution imaging, or polarimetry [2]. In this context novel cascaded configurations where the optical wave traverses several aligned BCs [3] play an important role. They lead to versatile techniques for the tailoring of multiple-ring-shaped vector waves and their optical angular momentum, up to the case where the output pattern loses its intrinsic circular symmetry in so-called conjugate cascades [4].

While few recent studies have combined CD with nonlinear optical frequency conversion, none has addressed a combination with the photorefractive effect. Here we introduce this possibility by combining the CD effect with the recording and read-out of holograms as well as local two-wave mixing amplification in a photorefractive material, where all processes are occurring within the same medium [5]. The experiments use nominally undoped and optically biaxial photorefractive $Sn_2P_2S_6$ and are performed at the 633 nm wavelength.

The above-mentioned spreading of the linear polarizations along the double ring by the CD effect has a remarkable consequence. Provided that the object wave propagates along an optical axis and gives rise to CD, it is possible to record a photorefractive hologram or achieve two-wave mixing local amplification of the CD waves with any combination of the object and reference wave input polarizations, including mutually orthogonal ones. An example applying to two-wave mixing is shown in Fig. 1(a). Here the gaussian input object wave is right circularly polarized and propagates along one of the optical axes to give rise to CD. Interaction with a reference wave of various input polarization leads to amplification including the case of the orthogonal left circular polarization.

In Fig. 1(b-e) we illustrate a case where a photorefractive hologram is recorded and read-out by the interaction of a circular polarized object wave and a horizontally (H) or vertically (V) linearly polarized reference wave (in the laboratory frame). Figure 1(b) shows the full ring of the transmitted object wave subjected to CD as obtained prior to hologram recording, while Fig. 1(c) (resp. 1(d)) show the reconstructed object wave after recording. This upon illumination of the crystal by the horizontally (vertically) polarized reference wave that was used for recording. Clearly, the section of the ring that is most strongly reconstructed depends on the input polarization of the reference wave, as seen also in Fig. 1(e) which shows the local reconstructed power as a function of the azimuthal position of the double-ring.

Even though not all required anisotropic material parameters of $Sn_2P_2S_6$ are known, it is shown that this kind of behavior can be qualitatively accounted by a simplified model for the involved complex physical contributions related to the photorefractive response and the dielectric and electro-optic properties. For the case above the approach is based on the evaluation of the coupling strengths between a plane reference wave with a fixed polarization and components of the object wave with all possible polarization directions taken as a variable parameter.

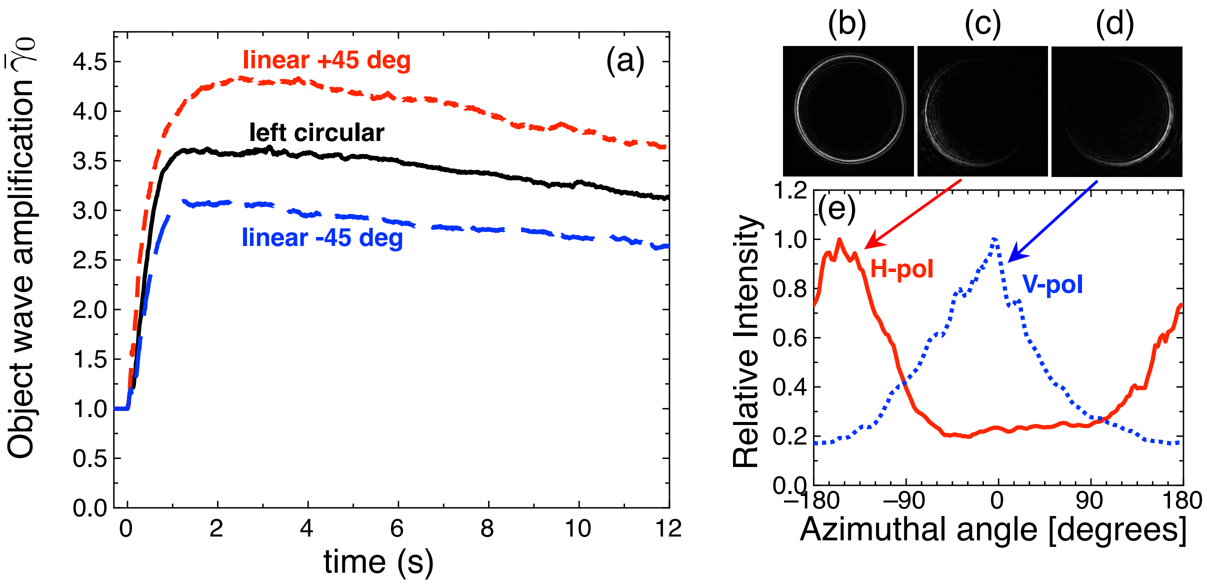

Figure 1: (a) Average two-wave mixing object wave amplification over the ring as a function of time for various combination of the input polarizations of object and reference waves. The black curve corresponds to mutually orthogonal input polarizations. (b)-(e) CD holography with circularly polarized input object wave and linearly polarized reference wave [horizontal (H) or vertical (V) in laboratory frame]. (b) CD object wave transmission prior to hologram recording; (c) object wave reconstruction for H- polarized reference; (d) object wave reconstruction for V-polarized reference; (e) normalized azimuthal dependence of local power on the reconstructed ring for cases (c) and (d).

It is worth noticing that the observation described above are specific to the case where the object wave is producing CD. Upon misalignment the object wave leads to standard double refraction and the behavior corresponds to the usually expected one with virtually no effect in the case where the two interacting waves have mutually orthogonal polarizations. One may say that the holographic recording process possesses a kind of angular resonance for the object wave direction parallel to one of the optical axes. The present approach opens interesting perspectives for the tailoring of the reconstructed and/or amplified CD vector waves and their static or dynamic manipulation, both in single BC and in cascaded configurations.

## References

[1] M. V. Berry, J. Opt. A: Pure Appl. Opt., 6, 289–300 (2004).
[2] A. Turpin, Y. V. Loiko, T. K. Kalkandjiev and J. Mompart, Laser Photonics Rev., 10, 750 (2016).
[3] M. V. Berry, J. Opt., 12, 075704, (2010).
[4] M. W. Iqbal, N. Marsal and G. Montemezzani, Opt. Express, 31, 29859 (2023).
[5] M. W. Iqbal, Y. Shiposh, A. Kohutych, N. Marsal, A. A. Grabar and G. Montemezzani, J. Opt. Soc. Am. B, 41, 1091-1098 (2024).

# The Photorefraction of lithium niobite: from bulk to thin film

**Yongfa Kong**[a,*], Dahuai Zheng[a], Shuolin Wang[b], Hongde Liu[a], Shiguo Liu[a], Jingjun Xu[a]

[a]MOE Key Laboratory of Weak-Light Nonlinear Photonics, TEDA Institute of Applied Physics and School of Physics, Nankai University, Tianjin 300457, China
[b]School of Science, Jiangsu University of Science and Technology, Zhenjiang 212100, China

* kongyf@nankai.edu.cn

Lithium niobite ($LiNbO_3$, LN) is a synthetic crystal that has excellent electro-optical, nonlinear optical, acoustic optical and photorefractive performance, and it is thus prominent in various optoelectronic applications. Recent breakthroughs in the fabrication of thin film lithium niobate (TFLN) combine the unique features of the bulk crystal onto an integrated platform with submicron light confinement. Revolutionary performances are expected by moving from bulk to TFLN in the form of lithium-niobate-on-insulator (LNOI) optical communication and wireless communication devices, and this trend may also lead to fundamental breakthroughs in optical computation, microwave photonics, and quantum optics. Here we report several recent progresses in the photorefraction of $LiNbO_3$ from bulk to thin film. It was found the optical damage resistance and photorefraction can be simultaneously enhanced in MgO and $Bi_2O_3$ co-doped $LiNbO_3$ (LN:Bi,Mg). The experimental results indicate that photorefraction doesn’t equal to optical damage. The underground mechanism was analyzed and attributed to that diffusion dominates the transport process of charge carriers, that is to say photorefraction causes only slight optical damage under diffusion mechanism. Furthermore, a photorefractive response time of 7.2 ms was measured at 442 nm laser in a LN:$Bi_{1.25}$,$Mg_{6.0}$ crystal, a binary-electron photorefractive center model was proposed, that is when excited by suitable light, the two lone-pair electrons of $Bi^{3+}$ ions are much easier to lose, which cause the fast response speed. On the other hand, in applications such as second harmonic generation, frequency comb generation, and microwave-to-optics conversion, the device performance is strongly impeded by the photorefractive effect in TFLN.

## References

[1] Z. Xie and S. Zhu, Adv. Photonics 4, 030502 (2022).

[2] D. Zheng, Y. Kong, S. Liu, M. Chen, S. Chen, L. Zhang, R. Rupp and J. Xu, Sci. Rep. 6, 20308 (2016).

[3] D. Zheng, W. Wang, S. Wang, D. Qu, H. Liu, Y. Kong, S. Liu, S. Chen, R. Rupp and J. Xu, Appl. Phys. Lett. 114, 241903 (2019).

[4] S. Wang, Y. Shan, W. Wang, D. Zheng, H. Liu, S. Liu, Y. Kong, J. Xu, Appl. Phys. Lett. 118, 191902 (2021).

[5] S. Wang, Y. Shan, D. Zheng, S. Liu, F. Bo, H. Liu, Y. Kong, J. Xu, Opto-Electron. Adv. 5, 210135 (2022).

[6] H. Jiang, R. Luo, H. Liang, X. Chen, Y. Chen, and Q. Lin, Opt. Lett. 42, 3267 (2017).

[7] Y. Xu, M. Shen, J. Lu, J. Surya, A. Sayem, and H. Tang, Opt. Express 29, 5497 (2021).

# The thermo-photogalvanic effect in Fe:$LiNbO_3$ and its microscopic interpretation

**Marco Bazzan** [a], Michel Aillerie [b], Edvard Kokanyan [c, d]

[a] Università di Padova - Dipartimento di Fisica e Astronomia, Via Marzolo 8, 35131 Padova, Italy
[b] Laboratoire Matériaux Optiques, Photonique et Systèmes, Université de Lorraine et CentraleSupéléc, 2 rue E. Belin, F-57070 Metz, France
[c] Institute for Physical Research, National Academy of Sciences of Armenia, Ashtarak-2, 0203, Armenia
[d] Armenian State Pedagogical University after Kh. Abovyan, Tigran Metsi Ave., 17, Yerevan, Armenia

* marco.bazzan@unipd.it

Iron – doped lithium niobate (Fe:$LiNbO_3$) is one of the first materials displaying the photogalvanic effect (PGE), also known as bulk photovoltaic effect (BPVE). This effect consists in the generation of a current density inside the material without any electrical bias, when the former is exposed to light. Interestingly, the effect is not established by the presence of any interfaces or gradients such as in the case of p-n junctions in semiconductors. Instead it derives from a structural property of the lattice, i.e. the absence of an inversion center. Glass [1] was the first to propose a simple explanation of the PGE in terms of a preferential emission direction of photo-excited charges. In Fe:$LiNbO_3$ the donor centers are $Fe^{2+}$ impurities sitting at the Li site, which occupies a non-centrosymmetric position. These donor centers create localized defect states in the band-gap that can be excited by a photon in the visible. Thus, when the material is illuminated with visible light, an electron is photo-excited in the conduction band. However the emission probability along the $\pm c$ direction is not equal, due to the non-centrosymmetric lattice potential at the Fe site. Thus a net current is established.

Since Fe:$LiNbO_3$ is an insulator, in an open-circuit configuration the photocurrent accumulates charges at the crystal' surfaces and a large electric field is eventually built up, which may significantly exceed the bandgap of the material overcoming the well-known Shockley – Quiesser limit of semiconductor photovoltaics. For this reason, the PGE has attracted significant interest as an alternative approach for light energy conversion [2]. In the case of Fe:$LiNbO_3$, Nadupalli and co-workers [3] reported an interesting coupling between the BVPE effect and the mechanical stress load applied to the sample. It is therefore very natural asking whether a similar enhancement can be obtained by other external fields. In this contribution, we report, to our knowledge for the first time, the dependence of the PGE effect in Fe:$LiNbO_3$ on the sample temperature, which we may call thermo-photogalvanic effect (TPGE).

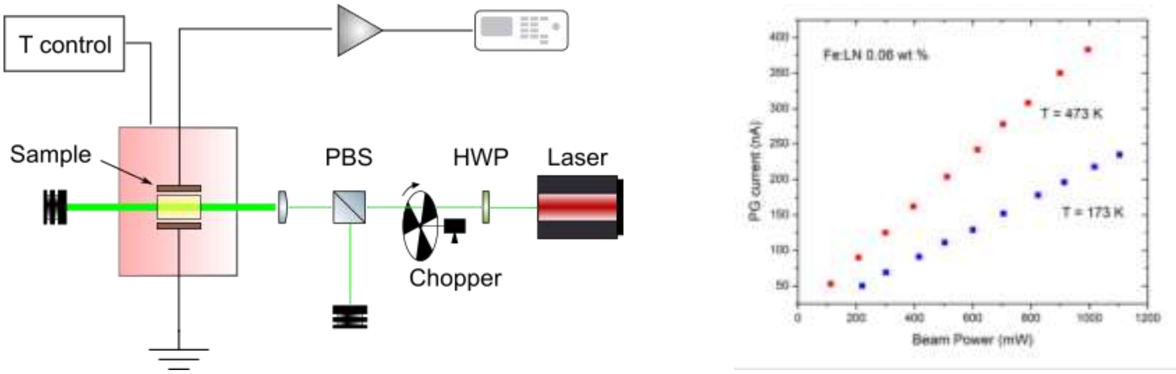

*Fig. 1 (Left) Scheme of the experimental setup. (Right) PG current vs beam power at two different temperatures.*

The setup is relatively simple, see Fig. 1 (left). A Ti:Sapphire laser emitting at 532 nm is modulated by a mechanical chopper. The beam power is adjusted by means of a half-waveplate (HWP) and a polarizing beamsplitter (PBS). The beam is shaped by a lens so to provide a uniform illumination along the sample. The latter is a Fe:$LiNbO_3$ sample 0.06 wt% grown by the Czochralski technique, cut and polished in the form of a cube. A couple of Ag electrodes has been painted on the $\pm c$ faces to collect the photocurrent, which is measured by a transimpedance amplifier. The frequency of the chopper has been set at 30 Hz which is enough to rule out the slow pyroelectric contribution to our measurement. The sample is contained inside a Linkam ® cell which allows the sample temperature to be set between 150 and 500 K.

In fig. 1 (right) are reported two exemplary dataset obtained at different temperatures. As it can be seen the slope of the photocurrent increases markedly with temperature, indicating that the PGE coefficients are temperature- dependent, in agreement with previous findings [1]. In order to interpret this effect, we consider a polaron model for the PGE effect [4]. As said, the PGE effect consists of an initial stage when electrons are emitted as Bloch waves from the Fe$^{2+}$ centers. After being emitted, the electrons lose energy by interaction with the lattice and finally self-localize into a lattice site as a small electron polaron. After this stage, polarons can move by thermally activated hopping among the lattice sites with a Marcus-Holstein’s jump frequency of the form:

$$W(r_{ij},T) = w_{ij}(T)e^{-2r_{ij}/L_{ij}} \qquad w_{ij}(T) = \left(\frac{\pi}{kT\lambda_{if}}\right)^{\frac{1}{2}} \frac{I_{if}{}^{2}}{\hbar} \exp\left(-\frac{U_{if}}{kT}\right) \tag{1}$$

Where $i(j) = F, P, T$ are labels indicating the type of initial and final hopping sites: $F$ for polarons sitting on the Nb$_{\text{Nb}}$ regular site, $P$ for polarons sitting on an antisite Nb$_{\text{Li}}$ defect and $T$ for polarons trapped at the Fe$_{\text{Li}}$ site. $r_{ij}$ and $L_{ij}$ are the distance between the hopping sites and a characteristic hopping length specific for the choice $(ij)$. Here, $I_{if}$ is the resonance integral, $\lambda_{if} = E_i + E_f$ is the lattice reorganization energy equal to the sum of the lattice elastic deformation energy in the initial and final states, and $U_{ij} = \left(2E_i + \varepsilon_i - \varepsilon_f\right)^2/4\left(E_i + E_f\right)$ is the hopping barrier equal to the activation energy of the hop from the initial to the final state, $\varepsilon_i, \varepsilon_f$ being additional energies for the Coulomb attraction of impurity centers. For the system under consideration, several of these parameters have been estimated [5]. After emitting the electron, the donor centers become Fe$^{3+}$ and act as traps for electrons. In this process, there is a fraction $\phi$ of polarons that can be retrapped by the same Fe center they came from and thus do not contribute effectively to the photogalvanic current. By combining the Marcus-Holstein’s equations (1,2) for polaron hopping with a simple phenomenological model describing the probability distribution function (PDF) of the newly formed polarons around the initial Fe$^{2+}$ site, we calculate the fraction $\phi$ of re-trapped electrons as a function of temperature. The PGE is proportional to the efficiency of the photo-generation process, i.e. $\eta = 1 - \phi(T)$. Our results are in good agreement with data.

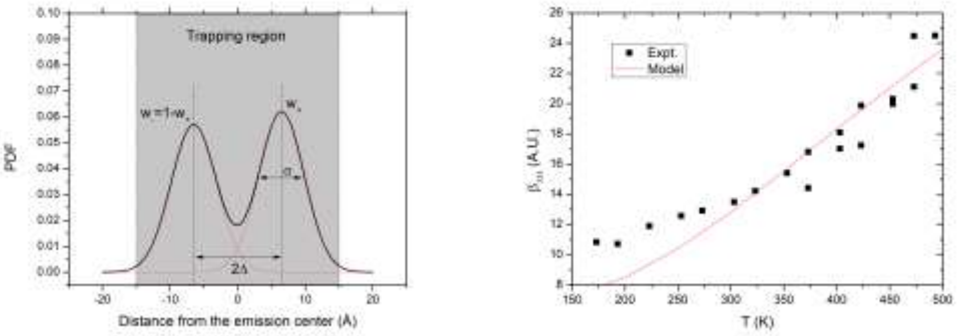

*Fig. 2: (Left): phenomenological PDF for newly created polarons. (Right): experiment and theory comparison.*

## References

[1] Glass, A. M., et al. *Applied Physics Letters* 25.4 (1974): 233-235.

[2] Paillard, Ch. et al. Advanced Materials 28.26 (2016): 5153-5168.

[3] Nadupalli, Sh. et al. Science advances 5.3 (2019): eaau9199.

[4] Schirmer, O. F., et al., Physical Review B 83.16 165106 (2011).

[5] Guilbert, L., et al. *Journal of Physics: Condensed Matter* 30.12 (2018): 125701.

# Photorefractivity and Transient Photoconductive Dynamics for Triphenylamine-Based Polymers

**Naoto Tsutsumi**[a*], Takafumi Sassa[b], Tam Van Nguyen[c,d], Sho Tsujimura[d], Giang Ngoc Ha[d,e], Yusuke Mizuno[d], Boaz Jessi Jackin[f], Kenji Kinashi[a], Wataru Sakai[a]

[a] Faculty of Materials Science & Engineering, Kyoto Institute of Technology, Sakyo, Kyoto 606-8585, Japan
[b] Photonics Control Technology Team, Riken Center for Advanced Photonics, Wako 351-0198, Japan
[c] Institute of Applied Science and Technology, Van Lang University, Ho Chi Minh City, Vietnam (present)
[d] Graduate School of Science and Technology, Kyoto Institute of Technology, Sakyo, Kyoto, 606-8585, Japan
[e] Faculty of Chemical Technology, Ho Chi Minh City University of Food Industry, Ho Chi Minh City, Vietnam (present)
[f] Materials Innovation Laboratory, Kyoto Institute of Technology, Sakyo, Kyoto, 606-8585, Japan
* tsutsumi@kit.ac.jp

## INTRODUCTION

Photorefractive (PR) polymers have an advantage of making a large scale holographic display device because of easy processing and high optical diffraction properties [1-3]. To design PR polymers, commonly photoconductive polymer, sensitizer, optical nonlinear chromophore, and photoconductive plasticizer are properly selected. Each component has clear role when we design PR polymer on the table, and we have common understanding that PR properties for polymer composites are characterized by the space charge field induced optical diffraction and optical gain. On the other hand, the photorefractive properties of the practical PR polymers prepared are significantly affected by, for example, the choice of organic solvent for preparing PR mixture [4, 5], processing temperature [6], and the glass transition of obtained PR polymers [4], etc. Those are because the microscopic behavior of components including solvent would be unclear and affect each properties and also final PR properties. Furthermore the microscopic behavior is not fully quantitatively analyzed, and thus the resulting photorefractive dynamics are also complicated. The analysis of transient photocurrents of PR composites is useful tool to understand the complicated photorefractive dynamics. Here we focus on the transient photocurrents of PR polymer composites with different composition ratios and those preparing different solvents.

## RESULTS AND DISCUSSION

Recently we measured transient photocurrent with two major peaks, one is in time region between 0.1 and 1 ms and the other is in time region between 0.1 and 1 s for the PR polymer consisted of poly((4-diphenylamino)benzyl acrylate) (PDAA), (4-diphenylamino)phenyl)methanol (TPAOH), (4-(azepan-1-yl)-benzylidene)malononitrile (7-DCST), and [6,6]-phenyl-C61-butyric acid methyl ester (PCBM) with various composition ratios prepared from chloroform [4]. We could not simulate the complicated transient photocurrent with two peaks using conventional single-trapping site model [7] and two-trapping site model [8]. To analyze these transient photocurrents with two major peaks, we propose the two-trap model with two recombination rates [4] which is expanded from the conventional two-trap with one recombination rate [8]. On the other hand, the same PR polymers prepared from tetrahydrofuran (THF) shows the transient photocurrent well simulated using the conventional two-trapping site model [5]. The key for these difference is the solubility of PCBM in solvent for preparing. Interesting results have been reported that the solubility of PCBM in chloroform is much greater than that in THF [9]. We assume that it is easier to form the charge transfer (CT) complex between PCBM and PDAA in chloroform than that in THF [4]. Thus, CT complex in addition to only PCBM work as photocarrier generation and recombination site. Thus, PCBM only and CT complex between PCBM and PDAA are considered as two carrier generation and recombination sites in the PR polymer prepared from chloroform, and PCBM only as single photocarrier generation and recombination sites in the PR polymer prepared from THF. Hole mobility (μ) of hole carriers are estimated from the width of density of states (DOS) measured using a photoelectron yield spectroscopy (PYS). Quantum efficiency (QE) of photocarrier generation is evaluated from the initial slope of the transient photocurrent. Trapping rates for shallow and deep trap, and two recombination rates are evaluated from the analysis of transient photocurrent using expanded model with evaluated μ and QE. PR trap density measured from the photorefractive optical diffraction and optical gain corresponds well to QE for all PR composites. The detailed contents of the current presentation is published in the recent paper [4].

## FUTURE PERSPECTIVES

In PR polymers, in addition to intensity coupling, phase coupling is expected because of the phase shift $\neq 90°$ ($\pi/2$). These unique properties of PR polymers will provide us with interesting phenomena and this is another interesting issue to be resolved in future. Furthermore, complex signal generation and detection in PR two wave mixing with perturbation [10] is unknown field for PR polymers. The time region of the transient photocurrent analyzed in the present report is those in this nonlinear dynamics region and thus we think present fundamental analysis are very important to develop new phenomena of PR polymers in future.

## References

1. P.-A.Blanche, J.-W. Ka, N. Peyghambarian, Review of organic photorefractive materials and their use for updateable 3D display’. *Materials* **14**, 5799. (2021). https://doi.org/10.3390/ma14195799
2. H. N. Giang, K. Kinashi, W. Sakai, N. Tsutsumi, Photorefractive response using composite based on poly(4-(diphenylamino)benzyl acrylate) and real-time holographic application. *Polym. J.* **46**, 59–66. (2014). https://doi.org/10.1038/pj.2013.68
3. S. Tsujimura, K. Kinashi, W. Sakai, N. Tsutsumi, Recent advances in photorefractivity of poly(4-diphenylamino)styrene composites: Wavelength dependence and dynamic holographic images, *Jpn. J. Appl. Phys*. **53**, 082601 (2014) http://dx.doi.org/10.7567/JJAP.53.082601
4. N. Tsutsumi, T. Sassa, T. V. Nguyen, S. Tsujimura, G. N. Ha, Y. Mizuno, B. J. Jackin, K. Kinashi, W. Sakai, Photorefractivity and photocurrent dynamics of triphenylamine-based polymer composites, *Scientific Reports* **14**, 11286 (2024). https://doi.org/10.1038/s41598-024-61756-2
5. N. Tsutsumi, Y. Mizuno, B. J. Jackin, K. Kinashi, T. Sassa, H. N. Giang, W. Sakai, Photoelectron yield spectroscopy and transient photocurrent analysis for triphenylamine-based photorefractive polymer composites, *Photonics* **9**, 996 (2022). https://doi.org/10.3390/photonics9120996
6. S. Tsujimura, T. Fujihara, T. Sassa, K. Kinashi, W. Sakai, K. Ishibashi, N. Tsutsumi, Characterization of carrier transport and trapping in photorefractive polymer composites using photoemission yield spectroscopy in air, *Macromol. Chem. Phys.* **217**, 1785-1791 (2016). https://doi.org/10.1002/macp.201600070
7. J. S.Schildkraut, A. V. Buettner, Theory and simulation of the formation and erasure of space charge gratings in photoconductive polymers. *J. Appl. Phys*. **72**(5), 1888–1893. (1992). https://doi.org/10.1063/1.351662
8. O. Ostroverkhova, K. D. Singer, Space-charge dynamics in photorefractive polymers. *J. Appl. Phys*. **92**, 1727–1743. https://doi.org/10.1063/1.1491279 (2002).
9. J. Kniepert, *et al.* Effect of solvent additive on generation, recombination, and extraction in PTB7:PCBM solar cells: A conclusive experimental and numerical simulation study. *J. Phys. Chem. C* **119**, 8310–8320. (2015). https://doi.org/10.1021/jp512721e
10. S. Saju, K. Kinashi, N. Tsutsumi, W. Sakai, B. J. Jackin, Period doubling route to chaos in photorefractive two wave mixing, *Photonics* **11(6)**, 521 (2024). https://doi.org/10.3390/photonics11060521

# Photorefractive parameters of double-doped $Sn_2P_2S_6$ crystals

**A. Grabar**, K. Glukhov, M. Tsyhyka, V. Voloshyn

Institute for Solid State Physics and Chemistry, Uzhhorod National University,
88000 Uzhhorod, Ukraine

* alexander.grabar@uzhnu.edu.ua

$Sn_2P_2S_6$ crystals are attractive photorefractive materials, exhibiting sensitivity to light in the red and near-infrared spectral ranges, with relatively short response times and high sensitivity. These amplitude parameters and the dynamics of the photorefractive response can be varied by goaled doping [1], and our recent works were directed to a search for the new efficient dopants and their combinations. Two methods were employed to modify the samples: firstly, growth by vapor-transport technique in the presence of two types of impurities, and secondly, thermal indiffusion of the metals (Cu, Ag) into previously grown samples. This report presents data on the variation in photorefractive properties, dielectric and optical spectra achieved as a result of doping with pairs of elements, including Te-Cu, Te-Ag, Sb-Cu and Cu-Ag combinations.

The experiments on the photorefractive two-wave mixing were carried out using He-Ne laser irradiation (633 nm). A comparison of the parameters of the various double-doped crystals shows that, among all the studied compounds, the Sb-Cu dopants combination (1 mol.% of the both), obtained in the process of growing the $Sn_2P_2S_6$ crystal, forms a complex defect that provides two main advantages: a sufficiently high photorefractive sensitivity and relatively high stability of the photorefractive gratings (Fig. 1, 2). The measurements of the optical transmission spectra in these co-doped samples show that they are similar to the case of the Sb1%-doped $Sn_2P_2S_6$ crystals. The measured max values of the two-wave mixing gain are $\Gamma = 15\ cm^{-1}$ (at ~1 um grating period and $0.3\ W{\cdot}cm^{-2}$ light beam intensity, see Fig. 1). The gain value depends on the light intensity and reduces down to $\sim 10\ cm^{-1}$ at $0.1\ W{\cdot}cm^{-2}$, that is less as compared with the case of the $Sn_2P_2S_6$:Sb1% crystal [1]. The grating build-up time is in order of 10-100 ms, and is characterized by almost single-exponential type of the grating formation and high temporal stability of the amplified signal beam (Fig. 2). This is the main advantage of this crystal, in comparison with the various single-doped (Sb, Te, Cu, …) compounds, where the formation of the space-charge grating occurs with the substantial compensation processes and also exhibit instabilities of the signal beam after long-time sample exposure.

The obtained experimental results correlate well with the modelling performed using *ab initio* calculations of the electron spectra in the $Sn_2P_2S_6$ lattice with various defects. The calculations provide information regarding the energy of the defect levels in the gap and the most probable positions of the dopant within the lattice. The latter can be determined by minimising the total energy of the cell at various defect positions. Furthermore, this model enables the estimation of the variations in the physical parameters of the crystal induced by the impurity. Besides, the model calculation of the electron spectra in the $Sn_2P_2S_6$ lattice with two defects (Cu and Sb) in the same cell provides a possible explanation for the absence of compensatory processes in this double-doped crystal. As demonstrated by previous photo-EPR studies [3], the $Sb^{3+}$ impurity replaces the $Sn^{2+}$ cations and becomes charge-compensated due to the appearance of Sn vacancies $(3Sn^{2+} + 2V_{Sn}^{2-})^0$. This leads to the formation of two types of defects, which may be a potential reason for the electron-hole compensation observed during the formation of photorefractive holograms in Sb-doped crystals. The $Cu^{1+}$ impurity, situated in close proximity to $Sb^{3+}$, can compensate for the appearance of the Sn vacancy. The calculated electron spectra indicate that the additional electron states originating from the Sb and Cu adatoms have the same energy and thus form a single defect electron level in the gap. This is consistent with the single-exponential dynamics of the space-charge grating formation predicted by a single-level model of the photorefractive effect.

The advantages of this dual-doped Sb + Cu compound are illustrated by means of examples of typical photorefractive schemes. These include the dynamic interferometer with phase-modulated signal beam (Fig. 3 and 4) and also the efficiency of multi-beam interactions, such as semi-linear and mirrorless photorefractive oscillators. The experiments with the phase-modulated signal beam demonstrate that the photorefractive response is quadratic in modulation frequency, confirming the existence of a 90°-shifted photorefractive phase grating and thus the dominance of a purely diffusive mechanism of space charge formation.

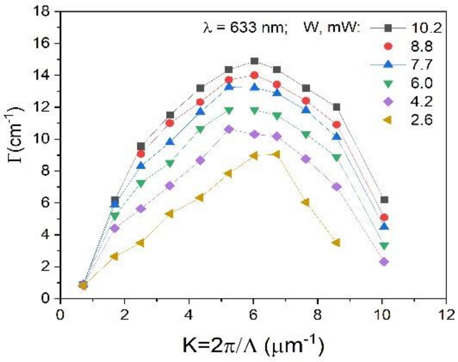

Figure 1: The dependences of the gain coefficient Γ on the wave vector of the photorefractive gratings, measured at various laser beam powers (633 nm).

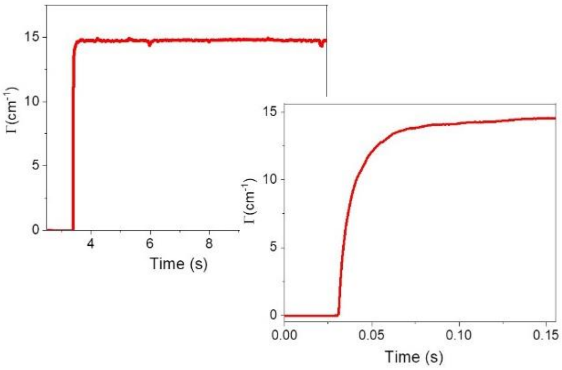

Figure 2: The typical dynamic of the photorefractive grating formation (at 10 mW laser power, 0.8 um grating period) in two time scales.

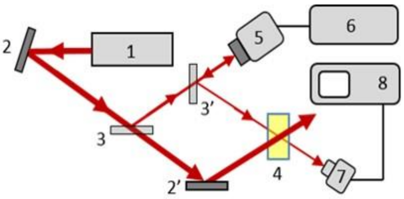

Figure 3: Scheme of the dynamic interferometer: here 1 - laser, 2 - mirrors, 3 - splitter, 4 - $Sn_2P_2S_6$ doped sample, 5 - piezo mirror, 6 - generator, 7 - photodiode, 8 - digital oscilloscope.

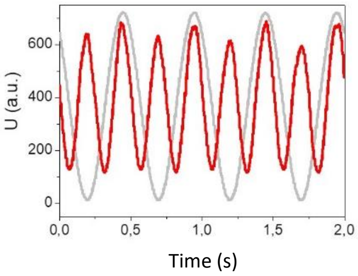

Figure 4: A typical oscillogram (red line) obtained in the dynamic interferometer at 11 Hz modulation frequency. Gray line - the signal on the piezo mirror.

Consequently, the co-doping of $Sn_2P_2S_6$ crystals with Sb and Cu represents a promising avenue for enhancing their photorefractive parameters. This modification enables the fabrication of a photorefractive grating that is stable over time and does not exhibit significant compensation processes.

## References

[1] A. A. Grabar, M. Jazbinšek, A. N. Shumelyuk, Yu. M. Vysochanskii, G. Montemezzani and P. Günter. Photorefractive effects in $Sn_2P_2S_6$. In: "Photorefractive Materials and Their Applications II". Springer, New York 327 (2007).
[2] V. Shvalya, J. Zavašnik, V. Nasretdinova, H. Uršič, J. Kovač, A. Grabar, A. Kohutych, A. Molnar, D. R. Evans, D. D. Mihailović, U. Cvelbar, J. Mater. Chem. C 8, 9975 (2020).
[3] B. E. Kananen, E. M. Golden, S. A. Basun, D. R. Evans, A. A. Grabar, I. M. Stoika, W. McClory, N. C. Giles, L. E. Halliburton, Optical Materials Express 6(12), 3992 (2016).

# Photorefractive effect and self-trapped-excitonic photochromism in Bi-doped and (Bi,Mg)-codoped stoichiometric $LiNbO_3$

**G. Mandula***, L. Kovács, G. Corradi, Zs. Szaller, L. Bencs, and K. Lengyel

HUN-REN Wigner Research Centre for Physics, 1121 Budapest, Konkoly-Thege M. út 29-33, Hungary

* mandula.gabor@wigner.hun-ren.hu

Recently extremely promising research has been published on the realization of real-time dynamic holographic display using (Bi,Mg)-codoped congruent lithium niobate crystals [1, 2]. To understand the microscopic processes of the build-up and erasure of light-induced holographic gratings in this material we have performed systematic investigations by means of low-intensity near-UV irradiation and absorption spectroscopy in the IR to near-UV region [3], completed by two-wave mixing methods. Bi- and Mg-codoped, as well as Bi single-doped stoichiometric $LiNbO_3$ (SLN) single crystals were grown with various dopant concentrations. Tracking down the incorporation of dopants and impurities including Fe and H by chemical and IR–UV spectroscopic analyses we assigned the various spectroscopic features to specific defect complex types. Absorption bands near 4 eV in all cases are ascribed to the generation of self-trapped excitons (STEs) pinned to dipolar defects consisting of $Bi^{3+}$ ions and their charge-compensators, becoming exceptionally long-lived due to the presence of lone pairs on $Bi^{3+}$. Near-UV illumination in Bi-single-doped crystals induces additional absorption bands at ≈2.7 and ≈3.4 eV persistent on the month scale and annealing near 150 °C. Double-doped crystals show similar but slightly blue-shifted photochromic bands with slightly higher thermal stability up to ≈250 °C and an additional stable band at ≈3.2 eV.

To investigate the role of the photochromism in holographic applications, a series of kinetic absorbance measurements have also been carried out at the fixed wavelength 405 nm (3.06 eV) as a function of temperature and intensity, using a diode laser with various dark delay times between 1-minute exposures (see Fig. 1, also showing the stretched-exponential buildup and partial decay of the absorption).

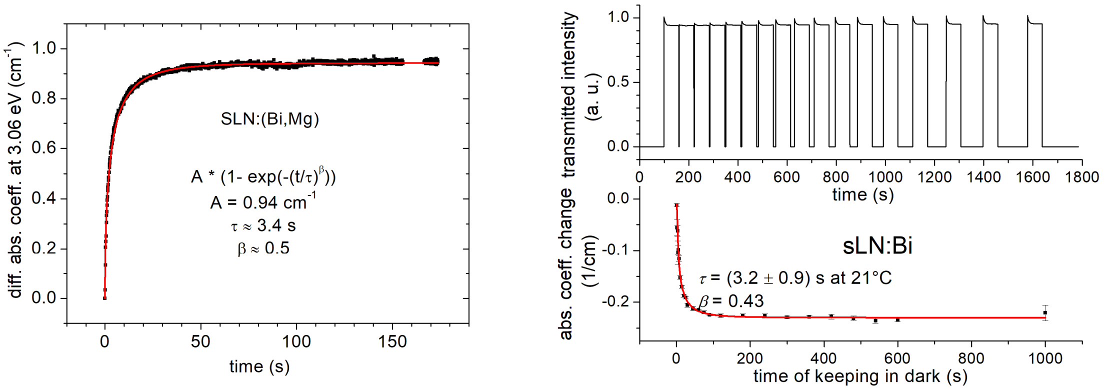

*Figure 1* – Left: build-up of the photochromic effect at 3.06 eV and 70 mW/cm$^2$ intensity in SLN:(Bi,Mg). Right: transmission in a typical measurement and fast stage relaxation of the absorption after a single UV pulse.

From the temperature dependence of the time constants in SLN:(Bi,Mg) activation energies of ≈0.3 eV and ≈0.4 eV could be determined for the buildup and fast stage relaxation of the photochromism, respectively (Fig. 2). In the case of SLN:Bi, both activation energies were ≈0.3 eV higher. In addition to changes on the timescale of minutes, absorbance was found to further decay significantly on the timescale of months. After a one-hour thermal treatment at 300 °C, the absorption coefficient $\alpha$ increased by ≈0.9 cm$^{-1}$ during illumination, while after keeping the sample in dark for some hours, $\alpha$ decreased by only ≈0.25 cm$^{-1}$. Fitting the time evolution of the absorption coefficient by a stretched exponential function resulted in values between 0.4 and 0.8 of the stretching parameter $\beta$, depending on sample composition and temperature, indicating that this process is a complex one consisting of many processes with different characteristic times. Intensity dependent measurements indicated a changing ratio of two- and one-photon processes.

From two-wave mixing experiments at a wavelength of 405 nm, in SLN:(Bi,Mg), energy transfer has been detected from the stronger beam to the weaker one (34 and 17 mW/cm$^2$ input intensities, respectively). The typical response time was near 100 ms at 25 °C, and followed an Arrhenius' law with an activation energy of 0.1 eV. Since at this wavelength the absorption coefficient of our samples of thickness 3 mm is rather high ($\alpha$ = 24 cm$^{-1}$), the intensities passing through the sample decrease by 3 orders of magnitude. We tried to explain the energy transfer by a purely photochromic effect, however, numerical calculations predict a much smaller energy transfer than obtained experimentally, indicating that charge transfer plays a more important role. The role and the ratio of the amplitude and phase hologram components in real time holographic display applications, as well as undesirable slower charge transfer processes will be discussed in the lecture.

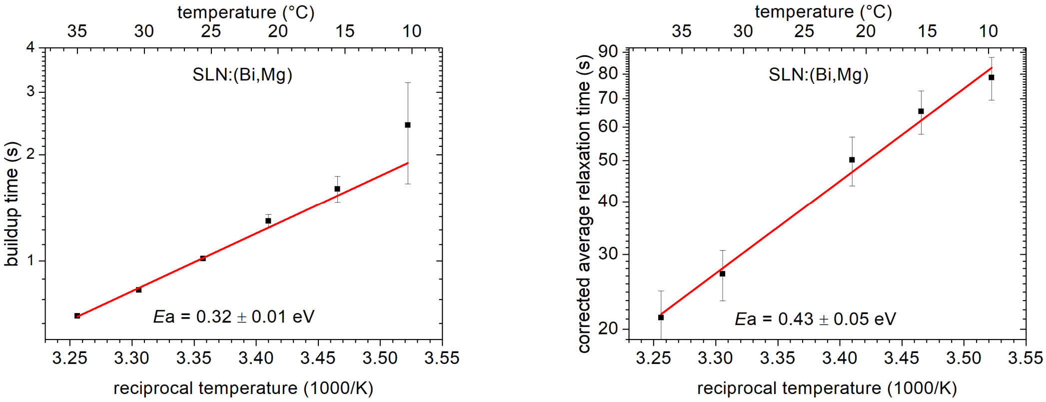

*Figure 2* – Arrhenius-fits for photochromic buildup (left) and relaxation times (right) in SLN:(Bi,Mg).

Based on our spectroscopic, photochromic and photorefractive measurements, we modify and complete the current structural and dynamic excitation model of SLN:(Bi,Mg). Earlier photorefractive experiments and hybrid-DFT electron structure calculations have only been interpreted in terms of relaxed Bi$^{3+}$ and Bi$^{5+}$-type centers, implying two-particle processes and charge separation. In the case of low-intensity irradiations, however, one-photon excitations and the consequences of the stability of exchange-coupled lone pairs have to be considered: instead of breaking up the lone pair, we assume the generation of long-lived STEs pinned to charge-compensated dipolar Bi$^{3+}$ defects. Accordingly, the formation of long-lived pinned STEs corresponding to the 4 eV absorption band can be modelled by charge transfer along a specific O–Nb bond singled out by the geometry of the adjacent pinning defect consisting of a Bi$^{3+}$ ion and its adjacent charge compensator(s), details depending on the Mg concentration. While this transfer does not directly result in separated electrons and holes, an option for charge separation is given by further excitation via the photoinduced bands of pinned-STEs. For the explanation of the enhanced photorefractive properties of the (Bi,Mg)-codoped crystals the shorter time constants of the photochromic bands and the active role of locally neutral Bi$^{5+}$ defects at Nb sites, weakly coupled to the lattice, serving also as efficient electron traps as suggested by the additional stable 3.2 eV band, is proposed. Optimizing growth procedures, stoichiometry and doping may further improve the application potential of the system.

## References

[1] D. Zheng, W. Wang, S. Wang, D. Qu, H. Liu, Y. Kong, S. Liu, S. Chen, R. Rupp, J. Xu, Real-time dynamic holographic display realized by bismuth and magnesium co-doped lithium niobate, *Appl. Phys. Lett.* **114**, 241903 (2019).

[2] S. Wang, Y. Shan, D. Zheng, S. Liu, F. Bo, H. Liu, Y. Kong, J. Xu, The real-time dynamic holographic display of LN:Bi,Mg crystals and defect-related electron mobility, *Opto-Electronic Advances* **5**, 210135 (2022).

[3] L. Kovács, G. Corradi, Zs. Szaller, L. Bencs, G. Mandula, and K. Lengyel, Lone-pair-delayed persistent excitonic UV-photochromism and charge transfer in Bi-doped and (Bi,Mg)-codoped stoichiometric lithium niobate single crystals, *Phys. Rev. B* (2024) (*in press*).

# Nonlinear photonic crystals via all optical poling of ferroelectrics

**W. Krolikowski**[a*], S. Liu[a], Y. Sheng[b]
[a] Department of Quantum Science and Technologies, Research School of Physics,
Australian National University, Canberra 2601 Australia
[b]Laboratory of Infrared Materials and Devices, Research Institute of Advanced Technologies,
Ningbo University, Zhejiang 315211 China

* Wieslaw.Krolikowski@anu.edu.au

The concept of nonlinear photonic crystal (NPC) introduced by Berger in 1998 [1], represents a medium with constant refractive index but spatially varying quadratic nonlinearity. NPCs are widely used in studies of nonlinear wave interaction offering potential applications in nonlinear optical control, wave shaping [3], entanglement etc. They have been commonly realized in ferroelectric crystals where electrical poling enables to modulate quadratic nonlinearity in one and two dimensions. However, this technique cannot be employed to create 3-dimensional structures. On the other hand, 3D NPCs would greatly increase their potential applicability.

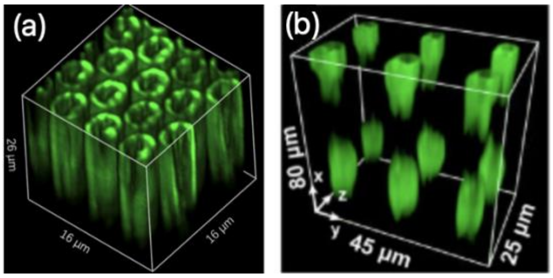

**Figure:** Optically induced domain patterns. **a)** Hexagonal domain pattern in CBN crystal; (b) 3-dimensional NPC in barium calcium titanate (BCT) crystal

We have shown recently that complex domain patterns can be formed in ferroelectrics using all optical poling [3]. In it, the short pulse infrared beam is focused inside the material leading to its local heating via two photon absorption. Resulting thermoelectric field may invert spontaneous polarization hence creating localized domains and their pattern. Consequently, formation of transparent 3D nonlinear photonic crystals became possible.

In this work we will discuss the all-optical poling technique and its application to form individual ferroelectric domains and their complex pattern in few ferroelectric crystals including, e.g. strontium barium niobate SBN, calcium barium niobate (CBN), and PMN:38PT. We will present our recent experimental results on nonlinear wave shaping using NPC formed via laser poling in ferroelectric crystals. In particular, we will demonstrate formation of second harmonic optical vortices and optical bottle beam [4].

**References:**

[1]. V. Berger, Phys. Rev. Lett. **81,** 4136 (1998).
[2] S Liu, et al., Nat. Commun. **10** (1), 3208 (2019).
[3] T. Xu, K. Switkowski, et al., Nat. Photonics **12**, 591 (2018).
[4] X. Hu et al, Opt. Lett **48**, 5527 (2023).

# Ferroelectric domain reversal in photovoltaic $LiNbO_3$ crystals driven by visible light

**C. Sebastián-Vicente** [a], J. Imbrock [b], S. Laubrock [b], O. Caballero-Calero [c], A. García-Cabañes [a], M. Carrascosa [a]

[a] Departamento de Física de Materiales and Instituto Nicolás Cabrera, Universidad Autónoma de Madrid, c/ Francisco Tomás y Valiente 7, 28049 Madrid, Spain
[b] Institute of Applied Physics, University of Münster, Corrensstraβe 2, 48149 Münster, Germany
[c] Instituto de Micro y Nanotecnología, IMN-CNM, CSIC (CEI UAM+CSIC) Isaac Newton, 8, Tres Cantos, E-28760 Madrid, Spain

* carlos.sebastian@uam.es

## Introduction

Iron-doped $LiNbO_3$ (Fe:$LiNbO_3$) is a promising ferroelectric platform thanks to its prominent bulk photovoltaic effect. Over the past ~15 years, this material has garnered significant attention for a wide range of optoelectronic applications: assembly of micro/nano-objects, optofluidics or manipulation of liquid crystals, among many others. So far, only monodomain crystals have been explored in the literature for such photovoltaic applications of Fe:$LiNbO_3$, overlooking the additional degree of freedom provided by domain-engineered Fe:$LiNbO_3$ substrates in combination with the bulk photovoltaic effect. Nonetheless, the traditional electrical method for domain engineering is complex and costly, involving lithography steps [1]. As an alternative, light-assisted poling methods are promising candidates with some advantages over standard electrical poling [2-4]. Herein, we present a novel all-optical approach for local domain inversion, only using continuous-wave visible light ($\lambda$ = 532 nm) [5].

## All-optical domain inversion in Fe:$LiNbO_3$ and $LiNbO_3$ crystals: results and discussion

The implementation of the all-optical method reported in this work is straightforward. The *z*-cut Fe:$LiNbO_3$ and undoped $LiNbO_3$ crystals are irradiated while enclosed in a conductive liquid, using a continuous-wave visible light source (see Figure 1a). Here, Milli-Q water has been used as the surrounding medium in most of our experiments, with a nominal resistivity of 18.2 MΩ·cm.

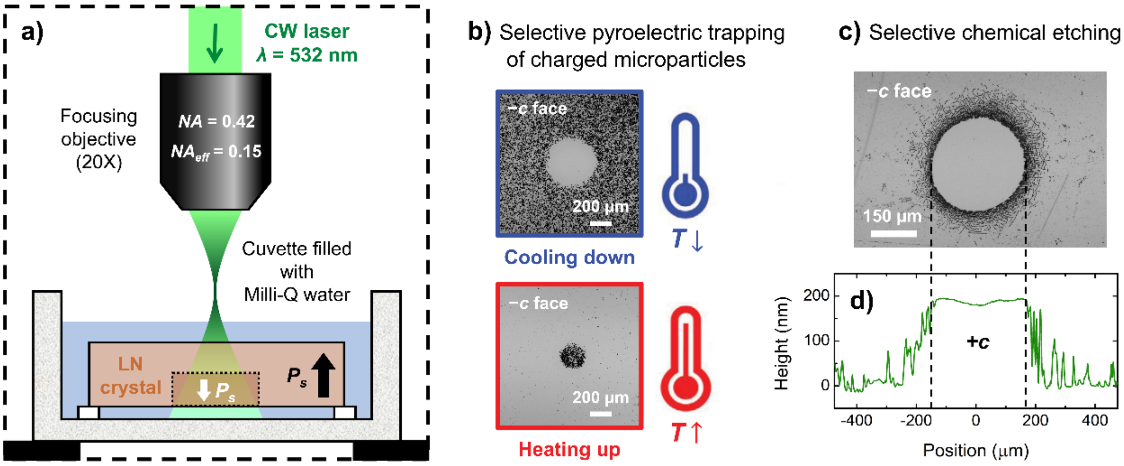

*Figure 1* – a) Schematic diagram of the setup. b) Trapping/repulsion of positively-charged toner microparticles induced by the pyroelectric effect at the laser-irradiated area (intensity $I$ = 86.4 W/cm$^2$, exposure time $t$ = 1 min, diameter $d$ = 280 µm) of an Fe:$LiNbO_3$ crystal. The top image shows the result upon crystal cooling ($\Delta T = -12\pm1$ °C), whereas the bottom image corresponds to crystal heating ($\Delta T = 12\pm1$ °C). c) Bright-field image after etching with HF acid. d) Measurement of the surface topography profile along the domain diameter after etching.

We have robustly demonstrated light-induced domain inversion using various techniques. First of all, pyroelectric trapping of positively charged toner microparticles confirms the reversal of the pyroelectric charge sign at the irradiated area (see Figure 1b). Then, selective chemical etching in HF acid clearly reveals the existence of an inverted ferroelectric domain (see Figure 1c). Surface profilometry along the diameter of the etched spot is consistent with the expected differential etch rate of +*c*/−*c* faces (see Figure 1d). Furthermore, Čerenkov SHG microscopy has been used to characterize the depth and 3D morphology of the inverted domains.

After the experimental demonstration of all-optical polarization switching, we have studied the impact of light intensity, exposure time, laser focusing conditions, incident crystal face, and surrounding medium on the size, morphology and depth of the light-inverted domains (see some examples in Figure 2). By tuning these parameters, ensembles of nanodomains, intricate self-assembled nanostructures or quasi-circular micro-domains may be generated. Furthermore, the applicability of our all-optical approach is also successfully showcased in undoped congruent $LiNbO_3$.

Importantly, we have found that the surrounding medium plays a critical role in the inversion process. In particular, the surrounding medium must be electrically conductive. Based on these results, we propose a novel qualitative model to explain light-induced domain inversion, which stems from a singular interplay between the bulk photovoltaic effect and external electrostatic screening.

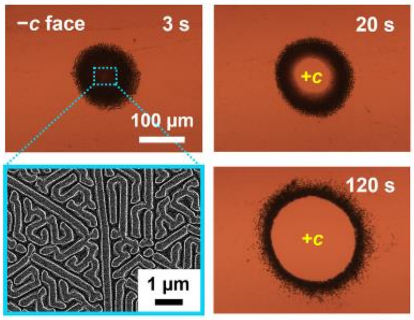

*Figure 2* – Inverted spots in Fe:$LiNbO_3$ after selective chemical etching in HF acid. In the experiments, a continuous-wave Gaussian laser beam was employed (diameter $d$ = 150 µm, intensity $I$ = 0.82 kW/cm$^2$) with different exposure times, indicated at the top-right corner of each image. The grayscale image corresponds to a scanning electron microscope (SEM) inset of the top-left experiment.

## Conclusions

The spontaneous polarization of photovoltaic $LiNbO_3$ crystals can be locally switched upon visible light excitation when the crystals are surrounded by an electrically conductive medium, such as water. This novel phenomenon, arising from the synergy between the bulk photovoltaic effect and external electrostatic screening, may be exploited for ferroelectric domain engineering of Fe:$LiNbO_3$ and undoped $LiNbO_3$ crystals. The method is extremely simple, low-cost, and easy to implement, avoiding high-voltage supplies, electrode patterning by lithography procedures and clean room facilities.

*Acknowledgments* − Financial support for this research project is gratefully acknowledged: grant PID2020-116192RB-I00 by MCIN/AEI/10.13039/501100011033 and grant TED2021-129937B-I00 by MCIN/AEI/10.13039/501100011033 and EU (FEDER, FSE). C. Sebastián-Vicente also thanks financial support through his FPU contract (FPU19/03940) and his grant for a stay in Münster (EST23/00644). Also, we acknowledge the service from the MiNa Laboratory at IMN, and funding from CM (project S2018/NMT-4291 TEC2SPACE), MINECO (project CSIC13-4E-1794) and EU (FEDER, FSE).

## References

[1] V. Ya. Shur, A. R. Akhmatkhanov, I. S. Baturin, Applied Physics Reviews, 2, 040604 (2015).

[2] C. Y. J. Ying, A. C. Muir, C. E. Valdivia, H. Steigerwald, C. L. Sones, R. W. Eason, E. Soergel, S. Mailis, *Laser & Photonics Reviews*, *6*, 526 (2012).

[3] X. Chen, P. Karpinski, V. Shvedov, K. Koynov, B. Wang, J. Trull, C. Cojocaru, W. Krolikowski, Y. Sheng, Applied Physics Letters, 107, 141102 (2015).

[4] X. Xu, T. Wang, P. Chen, C. Zhou, J. Ma, D. Wei, H. Wang, B. Niu, X. Fang, D. Wu, S. Zhu, M. Gu, M. Xiao, Y. Zhang, Nature, 609, 496 (2022).

[5] C. Sebastián-Vicente, J. Imbrock, S. Laubrock, O. Caballero-Calero, A. García-Cabañes, M.Carrascosa, arXiv:2312.13291 [cond-mat.mtrl-sci] (2023).

# Structured all-optical domain inversion in iron-doped lithium niobate

E. Asché [a], C. Sebastián-Vicente [b], O. Caballero-Calero [c], A. García-Cabañes [b],
M. Carrascosa [b], **J. Imbrock** [a]

[a] Institute of Applied Physics, University of Münster, Corrensstr. 2, 48149 Münster, Germany
[b] Departamento de Física de Materiales and Instituto Nicolás Cabrera, Universidad Autónoma de Madrid, c/ Francisco Tomás y Valiente 7, 28049 Madrid, Spain
[c] Instituto de Micro y Nanotecnología, IMN-CNM, CSIC (CEI UAM+CSIC) Isaac Newton, 8, Tres Cantos, E-28760 Madrid, Spain

* imbrock@uni-muenster.de

*Abstract* – Spatial customization of domain orientation in lithium niobate ($LiNbO_3$) is pivotal for many applications. Recent advances demonstrate light-assisted domain formation, notably using continuous-wave lasers for spatially structured domains. We extend this approach by modulating the intensity and shape of the light beam to form various domain patterns. We analyze the induced structures by second-harmonic generation microscopy and chemical etching. The dynamics and morphology of domain formation can be controlled by adjusting the light exposure.

## Introduction

Domain-engineered $LiNbO_3$ finds many applications, such as in quasi-phase matched parametric processes [1,2], surface acoustic wave devices, conductive domain walls for nanoelectronics, particle trapping [3], and many more. Ferroelectric domains cannot only be inverted by a high external electric field, but formation can also be induced or assisted by light. For example, focused infrared laser pulses can directly invert domains [4] or can assist domain formation together with an additional pyroelectric field [5]. Recently, a novel all-optical approach to locally invert domains was presented that uses continuous-wave (cw) laser light [6]. A Gaussian laser beam is focused in z-cut $LiNbO_3$, while the crystal is enclosed in a conductive medium such as water. The domains are inverted in bulk by the interaction between the photovoltaic effect and the external electrostatic screening. Here, we extend this new concept to form spatially structured ferroelectric domains.

## Structured Domain Inversion

Using an amplitude spatial light modulator, the transverse shape and intensity $I$ of a cw laser light field (532 nm) are customized and subsequently focused on the -c-side of a z-cut iron-doped $LiNbO_3$ crystal. The crystal was submerged in a reservoir filled with deionized water during this process. Although the light field was always focused on the -c face, the incident side of the laser was varied between the +c and -c face. Various intensity patterns, such as stripes, squares, triangles, circles, and grids, arranged in different orientations, were used. Figure 1 (a, d) shows two illumination fields incident directly on the -c face: a homogeneous ring (a) with $I \approx 536$ W/cm² and four squares of different intensities (d) with $I \approx \{134, 268, 402, 536\}$ W/cm². For the squares, a short exposure time of $t = 6$ s was chosen, while the ring-shaped illumination was applied for $t = 30$ s. Domain formation was examined by second-harmonic generation (SHG) microscopy (b, e) and bright-field microscopy images of the chemically etched surface (c, f). The SHG image in (b) was taken at the surface of the crystal. Due to the phase transition at the surface-air interface and the domain interfaces, the domain walls appear black in the reconstructed microscope image. The inner and outer edges of the ring are sharp and even, indicating uniform induction in the illuminated area at the surface. These observations are confirmed by recordings taken after chemical etching. The domain walls are clearly visible, and the undisturbed area between becomes evident, proving the optimal configuration of the exposure used. To reveal the mechanism of domain formation, we used a lower exposure with four squares of varying intensity and a shorter exposure time. For the lowest illumination intensity, shown in the top left of Figure 1 (e), the inversion process begins with the formation of single strains oriented preferentially along the $y$ crystallographic directions, appearing as dark domain walls in the image. With increasing exposure,

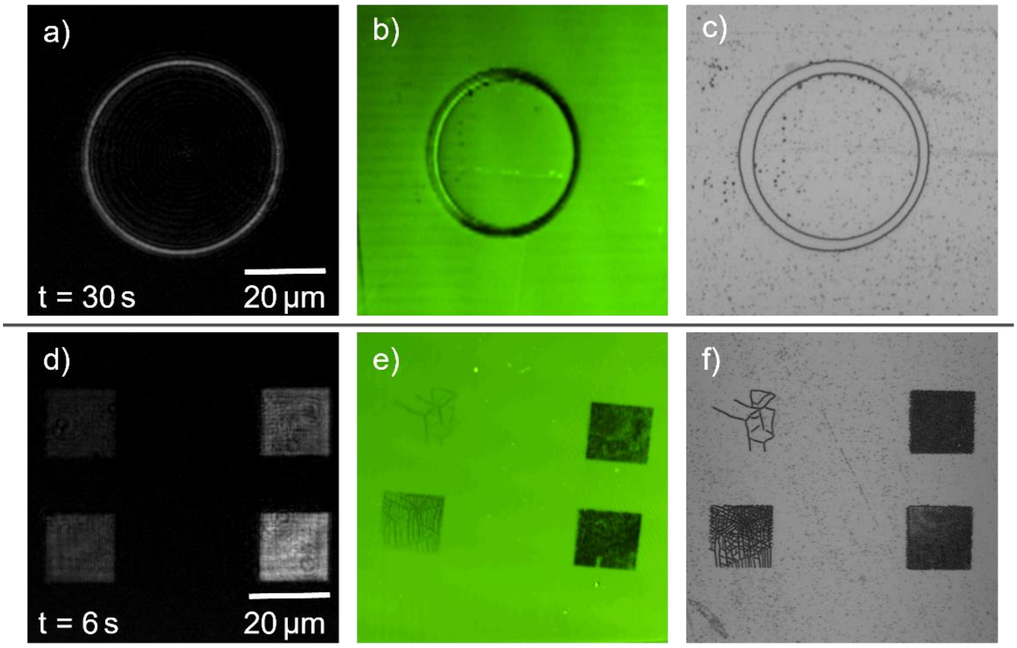

*Figure 1* – Inverted ferroelectric domains after illumination of 30 s (a-c) and 6 s (d-e), respectively, with two structured light patterns (λ = 532 nm). For a ring-shaped illumination (a), an SHG microscope image of the -c surface (b) and a bright-field microscope image after selective chemical etching in HF acid (c) are shown. The illumination pattern in (d) consists of four squares of different intensities with the respective SHG (e) and bright field image (f).

these strains grow and multiply within the illuminated area. Consequently, the squares of higher intensity become darker as the strain density increases. In the bright field image (f), this phenomenon is even more pronounced, to the point where the strains are so densely connected that the whole area is filled. If the exposure is further increased in time or intensity, all of the strains connect to form a fully developed single domain, as observed for the ring-shaped domain.

## Conclusions

We analyzed the shape and development of structured all-optical ferroelectric domain inversion in dependence on the amplitude of the light field and illumination time. The final domain shape can be controlled by light exposure for a given light pattern. The smallest thickness of a ring-shaped domain achieved so far is below 2 µm and not optimized yet. Customizing multiple structured domains simultaneously offers an efficient method, paving the way for novel applications in optoelectronic research.

## References

[1] L. E. Myers, W. R. Bosenberg, *Applied IEEE Journal of Quantum Electronics*, *33*(10), 1663 (1997).

[2] J. Y. Chen, Y. M. Sua, Z. H. Ma, C. Tang, Z. Li, Y. Huang, *OSA Continuum*, *2*(10), 2914 (2019).

[3] M. Esseling, A. Zaltron, C. Sada, C. Denz, *Applied Physics Letters*, *103*(6), 061115 (2013).

[4] X. Chen, P. Karpinski, V. Shvedov, K. Koynov, B. Wang, J. Trull, C. Cojocaru, W. Krolikowski, Y. Sheng, *Applied Physics Letters*, *107*(14), 141102 (2015).

[5] J. Imbrock, H. Hanafi, M. Ayoub, C. Denz, *Applied Physics Letters*, *113*(25), 252901 (2018).

[6] C. Sebastián-Vicente, J. Imbrock, S. Laubrock, O. Caballero-Calero, A. García-Cabañes, M. Carrascosa*, arXiv*:2312.13291 [cond-mat.mtrl-sci] (2023).

[7] M. Ayoub, P. Roedig, K. Koynov, J. Imbrock, C. Denz, *Optics Express*, *21*(7), 8220 (2013).

# Optical Stern-Gerlach effect in two non-parallel slab waveguides

Jiaxin Li, Zhaoyuan Wang, Yi Hu, Jingjun Xu

The MOE Key Laboratory of Weak-Light Nonlinear Photonics, TEDA Applied Institute and School of Physics, Nankai University, Tianjin 300457, China

## Introduction

Stern-Gerlach (SG) effect, initially found for unveiling the existence of quantized electron spins, is now a general concept describing a state-dependent separation. It has been widely explored in optics to achieve a function of optical splitting, but the current schemes always require a polarization- or wavelength-dependent process [1-3], thus showing limitations for broader applications.

In this work, we utilize the spatial modes of light as a new degree of freedom to demonstrate an optical splitting via the SG effect in a two-waveguide system. The splitting of spatial modes is realized by setting the system to have a spatially inhomogeneous coupling coefficient, which functions as a non-uniform magnetic field in analogy. This optical SG effect is experimentally verified by probing a pair of non-parallel slab waveguides.

## Results and discussion

We first build an equivalence between the Pauli equation governing the SG experiment and the coupled mode equations of a two-waveguide system. In two coupled waveguides, symmetric and anti-symmetric eigenstates exist, offering the basis to form a 2-by-2 Hilbert space required for describing spin states. A pair of coupled waveguides are set with spatially varied coupling coefficient $C(x)$ in the $x$-axis, in which the light evolution along the $z$-axis is governed by the following coupled equations:

$$\begin{aligned} i\frac{\partial A_1}{\partial z} &= -\frac{1}{2k}\frac{\partial^2 A_1}{\partial x^2} + C(x)A_2, \\ i\frac{\partial A_2}{\partial z} &= -\frac{1}{2k}\frac{\partial^2 A_2}{\partial x^2} + C(x)A_1, \end{aligned} \tag{1}$$

where $A_1$ and $A_2$ are electric field amplitudes in each waveguide, and $k$ is the wave vector of light. In order to relate the optical system to a two-level quantum system, Eq. (1) is rewritten in a matrix form, i.e., $i\partial\psi/\partial z = [-\partial_x^2/2k \cdot \sigma_x^2 + C(x)\cdot\sigma_x]\psi$, where $\psi = (A_1\,, A_2)^T$ and $\sigma_x$ is the $x$ component of Pauli operator. Then it is plain to see that the new form has a mathematical structure similar to the transverse Pauli equation governing the SG experiment [1]: the diffraction and the coupling correspond to the kinetic energy of electrons and a magnetic field, respectively. Thus, the spatially varied $C(x)$ is adapted in place of the nonuniform magnetic field in the SG effect. In quantum mechanics, spin is a degree of freedom that is independent of spatial coordinates in which the SG splitting occurs. This picture holds in our case in an analogous way. The space dimension of the $y$-axis, employed for constructing two spatial modes in analogy to spin states, is orthogonal to the other two space dimensions where light splitting will take place. The two analogous spin states have forms of $|A_\uparrow\rangle = (1,1)^T/\sqrt{2}$ and $|A_\downarrow\rangle = (1,-1)^T/\sqrt{2}$, typical eigenstates in the $\sigma_x$ representation. They correspond to the symmetric and anti-symmetric modes of the two coupled waveguides.

To study the state evolution in the above coupled equations, a Gaussian profile distributed in the $x$-axis, i.e., $\exp(-x^2/\omega^2)$ (where $\omega$ is a constant), is imparted to both the symmetric and anti-symmetric modes. As a representative example, $C(x)$ is preset to be a linear function. For an incident light formed only by $|A_\uparrow\rangle$ ($|A_\downarrow\rangle$), it deflects towards a place subject to a larger (smaller) coupling coefficient along the $x$-axis [Figs. 1(a, b)], accompanied with a diffraction-induced expansion. From these results, one can infer that the two modes can be separated through our structure if they are injected simultaneously. In a simple configuration, the two modes are launched with the same intensity, thus leading to an input condition of $(|A_\uparrow\rangle + |A_\downarrow\rangle)/\sqrt{2} = (1,0)^T$ or $(|A_\uparrow\rangle - |A_\downarrow\rangle)/\sqrt{2} = (0,1)^T$ in a normalized form. In either case, only one waveguide needs to be excited. Figure 1(c) presents the simulations by inputting light into waveguide #1. At the onset of the propagation, the optical field hops between the two waveguides back and forth, which is similar to the dynamics commonly seen in parallel waveguides. After a sufficient distance, a splitting occurs. The symmetric and anti-symmetric modes move upwards and downwards, respectively. They are featured with the same intensity after the separation, which is predetermined by the equal combination of them at the input. Identical dynamics is found for the case of exciting waveguide #2 only. It is worth noting that the mode splitting stems from a non-zero gradient of $C(x)$. It exists even if $C(x)$ deviates from a linear function.

Figure 1(d) schematically plots our setup to realize optical SG effect. Two coupled non-parallel slab waveguides manifest a “Λ” shape that is invariant along the propagation direction (i.e., the $z$-axis), while their spacing varies in the $x$-axis, resulting in a spatially dependent coupling coefficient. This construction is produced in a crystal by the photorefractive effect [4, 5]. Under a positive biased electric field, two crossing light sheets laterally illuminating the crystal can induce the “Λ” shaped waveguide structure (refractive index distribution). The beam dynamics in this structure is probed by injecting a properly shaped beam at the input. Both the writing and probe beams are controlled at ease by a programmable spatial light modulator. Limited by the length of the crystal, the measurement is performed instead in momentum space, where light deflection and splitting are less influenced by diffraction-induced beam expansion. For this purpose, a lens (L), positioned between the output of the crystal and a charge coupled device (CCD), is employed for a Fourier transform.

We employed two elliptical Gaussian beams with identical phase or a π phase difference to excite the symmetric or anti-symmetric modes, respectively. Figures 1(e-h) illustrate output spatial spectra for different input conditions. At the output, the symmetric mode exhibits a momentum change towards the crossing of the two waveguides [Fig. 1(e)], indicating a beam deflection along the same direction in real space. The anti-symmetric mode tends to move in the opposite direction [Fig. 1(f)]. The measured light profile manifests with two intensity spots in Fourier space, stemming from its out-of-phase configuration in real space. For one-site excitations (using either one of the elliptical Gaussian beams only, which can be regarded as a coherent superposition of the two waveguide modes), its spatial spectrum presents three intensity parts [Figs. 1(g, h)]. This process indeed involves a splitting of the two modes, as shown in the previous simulations. The upper one and bottom two spectral parts are associated with the symmetric and anti-symmetric modes, respectively, as inferred by comparing them with the results in the case of the two-site excitation plotted in Figs. 1(e, f).

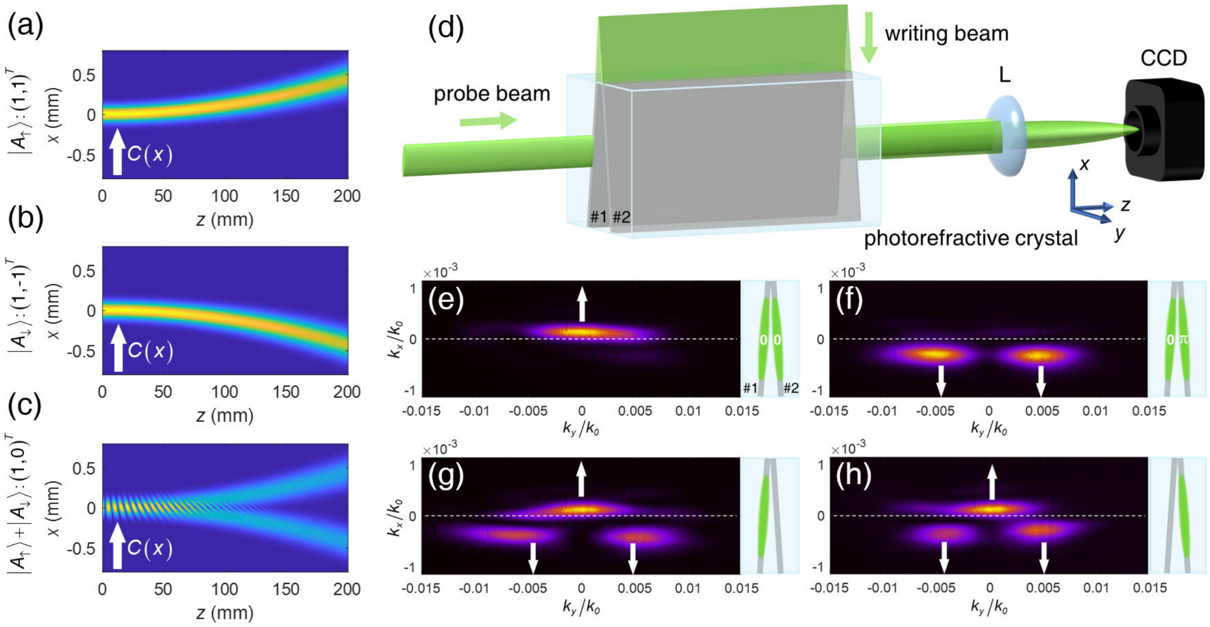

Fig. 1. (a-c) Simulated beam propagations in two non-parallel slab waveguides schematically shown in (d) under different input conditions: (a) symmetric, (b) anti-symmetric modes, and (c) their superposition are injected. (d) Schematic experimental setup showing how to write and probe the non-parallel slab waveguides. (e-h) Output intensity profiles in momentum space under different input conditions (see the insets: gray and green shadings stand for waveguides and input beams, respectively, and 0 and π are phases).

## References

[1] A. Karnieli and A. Arie, Phys. Rev. Lett. **120**, 053901 (2018).
[2] M. Król, et al., Phys. Rev. Lett. **127**, 190401 (2021).
[3] O. Yesharim, et al., Nat. Photonics **16**, 582 (2022).
[4] Z. Wang, et al., Phys. Rev. A **106**, 053107 (2022).
[5] Z. Wang, et al., Laser Photonics Rev. **17**, 2300037 (2023).

# N-type and p-type domain walls fabricated by atomic force microscopy

**S. B. Li** [a], M. L. Li [a], J. J. Xu [a], G. Q. Zhang [a].

[a] The MOE Key Laboratory of Weak-Light Nonlinear Photonics,
School of Physics and TEDA Applied Physics Institute, Nankai University, Tianjin 300071, China

* sanbingli@mail.nankai.edu.cn

**Abstract:**

Lithium niobate (LiNbO$_3$) is an excellent optical material platform with various applications in electro-optics, acousto-optics and frequency conversion. The advent of the lithium niobate on insulator (LNOI) platform has catalyzed significant advancements in optoelectronic integration using lithium niobate, leading to breakthroughs such as efficient second harmonic generation[1], high-speed electro-optical modulators[2], and on-chip lasers through rare earth ion doping[3]. Nevertheless, the challenge of low conductivity (approximately $10^{-12}\ \Omega^{-1}\text{cm}^{-1}$ for 5 mol% MgO-doped LN) and the hurdle in achieving p-type doping have rendered the fabrication of p-n junctions, a critical component for optoelectronics, on LNOI nearly unfeasible. Encouragingly, the possibility of creating n-type and p-type ferroelectric domain walls opens new avenues[4-6].The successful integration of both types of domain walls could make the fabrication of p-n junctions possible.

In our study, we have engineered n-type and p-type ferroelectric domain walls on a 600-nm thick, x-cut, 5-mol% MgO-doped LN film using litho PFM mode, which is a versatile module of atomic force microscopy (AFM), capable of fabricating micro and nano-scale domains of arbitrary shapes. Therefore, by employing this technology, it is possible to align domain walls, originally only a few nm width, as closely as possible, to create a p-n junction without an intrinsic intermediate region. First, the probe tip with a high-voltage generates a lateral electric field component that can reverse the domain near the probe. As the probe scans over a square area of 20 μm × 20 μm, it reverses the spontaneous polarization of that area. As shown in Fig. 1(a), the spontaneous polarizations are pointing away from the domain wall on the left side of the inverted area, leading to negative bound charges at the domain wall, which can be compensated by holes, and resulting in a p-type domain wall. On the other hand, the spontaneous polarizations are pointing towards the domain wall on the right side of the inverted area, resulting in positive bound charges at the domain wall, which can be compensated by electrons, and producing a n-type domain wall. One notes that, with a maximum poling voltage of 150 V, the domain inversion may occur only near the surface of the film[6]. In order to reveal the depth of the domain wall, a slope was fabricated by FIB milling, and the two-dimensional (2D) and three-dimensional (3D) cross-section PFM image of the inverted domain are shown in Figs. 1(b) and 1(c), respectively. One sees that the inverted domain does not penetrate through the entire thickness of the film, and the domain wall is not straight. The depth of the inverted domain was estimated to be approximately 200 nm.

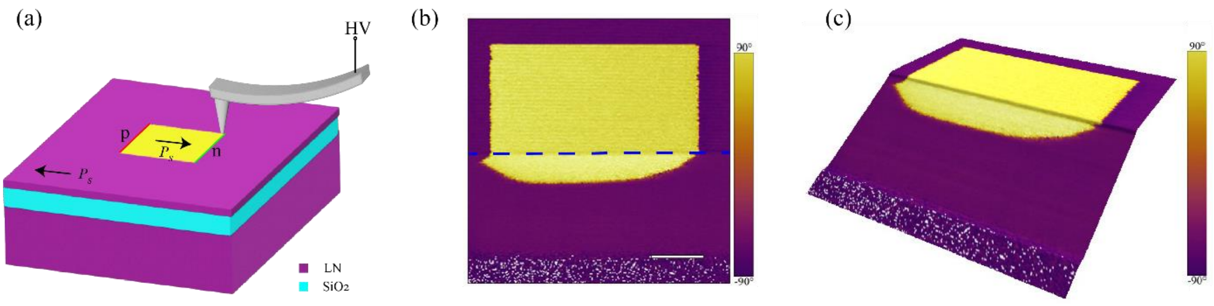

*Figure 1* (a) Schematic diagram of domain inversion through an AFM probe tip. (b) 2D cross-section PFM image after FIB milling, the scalebar is 5 μm and the blue dashed line represents the boundary line between the flat plane and the inclined plane milled by the FIB. (c) 3D cross-section PFM image after FIB milling.

For measurement of the electrical conductivity of domain wall, UV photolithography and magnetron sputtering techniques were employed to deposit pairs of electrodes exactly covering the domain walls with a gap distance of 8 μm. The *I-V* curves of a single n-type and p-type domain walls are shown in Figs. 2(a) and 2(b), respectively. From the measured data in Fig. 2, the conductivity $\sigma$ could be calculated through the formula $\sigma = S\,l/\,(wd)$, where $S$ represents the slope of the *I-V* curve, $w$, $d$, and $l$ correspond to the width, the depth, and the length of the domain wall, respectively. The slope of each I-V curve is linearly fitted with both positive and negative bias, and the slope with the positive bias voltage is listed in Fig. 2. For $w$ = 10 nm, $d$ = 200 nm and $l$ = 8 μm, the conductivity is estimated to be $\sigma_n$ = 2.92 ×10$^{-5}$ $\Omega^{-1}$cm$^{-1}$ for n-type domain walls and $\sigma_p$ =1.20 ×10$^{-7}$ $\Omega^{-1}$cm$^{-1}$ for p-type domain walls, which represents at least five orders of magnitude higher than that of the bulk LN crystal. Although the presented conductivities of n-type and p-type domain walls are still too low for practical applications, further improvement on conductivity might be achievable through targeted element doping[7,8].

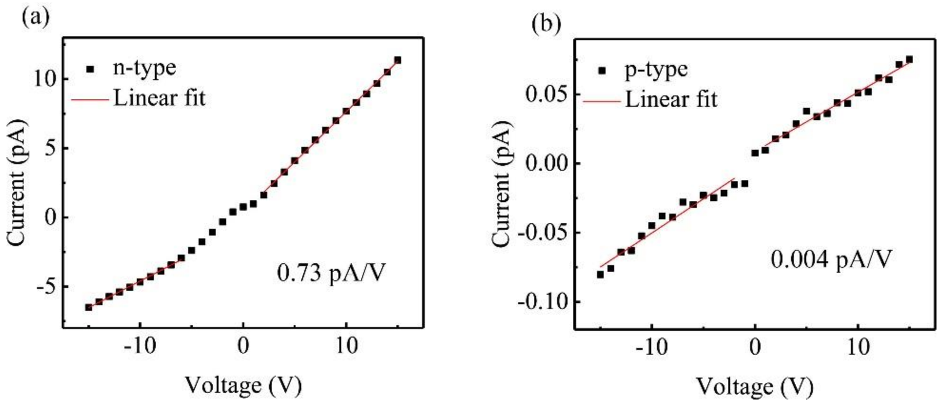

*Figure 2* (a) Measured *I-V* curve of a n-type domain wall. (b) Measured *I-V* curve of a p-type domain wall.

## References

[1] J. Lin, N. Yao, Z. Hao, J. Zhang, W. Mao, M. Wang, W. Chu, R. Wu, Z. Fang, L. Qiao, W. Fang, F. Bo and Y. Cheng, Physical Review Letters **122**(17), 173903 (2019).

[2] M. He, M. Xu, Y. Ren, J. Jian, Z. Ruan, Y. Xu, S. Gao, S. Sun, X. Wen, L. Zhou, L. Liu, C. Guo, H. Chen, S. Yu, L. Liu and X. Cai, Nature Photonics **13**(5), 359-364 (2019).

[3] Q. Luo, F. Bo, Y. Kong, G. Zhang and J. Xu, Advanced Photonics **5**(03), 034002 (2023).

[4] A. V. Ievlev, D. O. Alikin, A. N. Morozovska, O. V. Varenyk, E. A. Eliseev, A. L. Kholkin, V. Y. Shur and S. V. Kalinin, ACS Nano **9**(1), 769-777 (2015).

[5] Y. Qian, Y. Zhang, J. Xu and G. Zhang, Phys. Rev. Appl. **17**(4), 044011 (2022).

[6] Y. Qian, Z. Zhang, Y. Liu, J. Xu and G. Zhang, Phys. Rev. Appl. **17**(5), 054049 (2022).

[7] J. Schaab, A. Cano, M. Lilienblum, Z. Yan, E. Bourret, R. Ramesh, M. Fiebig and D. Meier, Adv. Electron. Mater. **2**(1), 1500195 (2016).

[8] W. Li, J. Cui, W. Wang, D. Zheng, L. Jia, S. Saeed, H. Liu, R. Rupp, Y. Kong and J. Xu, Materials (Basel) **12**(5),819 (2019).

# The pyroelectric effect in ferroelectric materials: new perspectives for biological applications

Simonetta Grilli

Ferroelectrics are functional materials with stable spontaneous polarization that can be reversed by an external electric field. They are the first-choice materials for a wide variety of applications including nonvolatile memories, field-effect transistors, solar cells, sensors, photonics devices, just to cite some. Only in the recent years the interest in potential applications of these materials for biological applications has risen. Here we present the possibility to use a specific property of these materials, i.e. the pyroelectric effect in lithium niobate (LN), for innovative manipulation methods for soft and biological matter. It is well known that in pyroelectric crystals a thermal energy is converted into electricity through the variation of the internal spontaneous polarization. We use periodically poled LN for a dynamic skin-over-liquid platform at microscale or for producing ordered arrays of fiber mats through a pyro-electrospinning process. In all cases the micropatterns have a potential application to address the behaviour of live cells at microscale with the overall advantage to be free from electrodes, nozzles and masks.

## References

- L. Qi, S. Ruan, Y.J. Zeng, Advanced Materials 33, 2005098 (2021)
- B. Castro, A. G. Cabanes, M. Carrascosa, Applied Physics Reviews 5, 041101 (2018)
- D. Zhang, H. Wu, C. R. Bowen, Y. Yang, Small 17, 2103960 (2021)
- V. Marchesano, O. Gennari, L. Mecozzi, S. Grilli, P. Ferraro, ACS Applied Materials and Interfaces 7, 18113 (2015)
- R. Rega, O. Gennari, L. Mecozzi, S. Grilli, V. Pagliarulo, P. Ferraro, Advanced Materials 28, 454 (2016)
- O. Gennari, R. Rega, M. Mugnano, E. Oleandro, L. Mecozzi, V. Pagliarulo, E. Mazzon, A. Bramanti, A. Vettoliere, C. Granata, P. Ferraro, S. Grilli, NPG Asia Materials 11, 1 (2019)
- R. Rega, O. Gennari, L. Mecozzi, V. Pagliarulo, A. Bramanti, P. Ferraro, S. Grilli, ACS Applied Materials and Interfaces 11, 3382 (2019)

# Control of plasmonic heating in biological media following all optical strategies

P. Camarero[a,b], N. Caetano[a,b,c], A. Benayas, [a,b,c] P. Haro[a,b,c], E. Cantelar[a,b], **M. Quintanilla**[a,b]

[a] Dept. of Materials Physics, Universidad Autónoma de Madrid. 28019, Madrid (Spain)
[b] Instituto de Ciencia de Materiales Nicolás Cabrera (INC), Universidad Autónoma de Madrid. 28019, Madrid (Spain)
[c] Institute for Advanced Research in Chemical Sciences, Universidad Autónoma de Madrid. 28019, Madrid (Spain)

* marta.quintanilla@uam.es

Photons reaching plasmonic nanoparticles and tuned to their resonance may be absorbed or scattered. Subsequently, the absorbed energy is typically released to the surroundings in the form of heat.[1] Absorption, thus, induces a local heating that can be used to aid chemical reactions at the nanoscale, in water remediation or, largely, in photothermal therapy against cancer or bacterial infections.[2] All these applications must be performed in aqueous media; though water may absorb part of the excitation wavelength, thus reducing the number of photons reaching the nanoparticles and heating up the optical path. This problem is extreme in the biomedical case, since other components (hemoglobin, melanin, lipids, etc.) contribute not only to absorption, but also to light scattering.[3] To face this lack of control on the illumination, we have tuned the resonance of plasmonic nanoparticles based on gold to the so-called biological windows (regions of the near-infrared range in which light attenuation by tissues is lower). Their heating performance has been characterized. To have access to local thermal information, we have applied luminescent nanothermometry techniques based on the emission of $CaF_2:Nd^{3+}$ nanoparticles. Our experiments illuminating through a model biological tissue or in tumoral spheroids show to what extent the interaction between light and tissue is relevant. In fact, it plays an important role for heating, but also for thermometry, as light emission needs to be recorded after travelling through the tissue. We have solved this second problem through an *in situ* recalibration of the thermometers.

## References

[1] G. Baffou, R. Quidant, C. Girard, Applied Physics Letters, 94, 153109 (2009)

[2] X. Cui, Q. Ruan, X. Zhuo, X. Xia, J. Hu, R. Fu, Y. Li, J. Wang, H. Xu, Chemical Reviews, 123, 6891 (2023)

[3] M. Quintanilla, M. Henriksen-Lacey, C. Renero-Lecuna, L.M. Liz-Marzán, Chemical Society Reviews, 51, 4223 (2022)

# Photovoltaic Interplay with living cells at Lithium Niobate interface

**L. Miccio** [a*], V. Bianco [a], M. Schiavo [a], F. Borrelli [a], P. Memmolo [a], C. Sada [b], P. Ferraro [a]

[a] CNR-ISASI, Istituto di Scienze Applicate e Sistemi Intelligenti "E. Caianiello", Via Campi Flegrei 34, 80078 Pozzuoli, Napoli, Italy
[b] Dipartimento di Fisica e Astronomia "G. Galilei" Università degli studi di Padova, Via Marzolo 8 - 35131 Padova (IT)

* lisa.miccio@cnr.it

Electric fields generated by Photovoltaic (PV) effect in ferroelectric crystals as Lithium Niobate (LN) have been deeply studies and modelled in the last 30 years, also in relation to the type and quantities of doping materials [1]. One of the research field developed in this framework concerns the activation and exploitation of the evanescent fields on the surface of such crystals for application as parallel trapping of microparticles or liquid/fluid handling [2]. Also polymer structures have been realized by exploiting evanescent field on the surface of LN [3]. Indeed, PV effect is responsible of the activation of virtual electrodes in LN by means of the interaction with light at suitable wavelength and power. The creation of PV electrodes avoids integration of different materials, typically needed for printed electrodes, thus simplifying the fabrication processes. Moreover, virtual electrodes present an intrinsic flexibility in terms of spatial geometry when diffractive optical elements are integrated in the illumination setup. Recently, it has been demonstrated also the possibility to interface biological samples achieving cell patterning and biological fluid manipulation [4,5]. In this work some examples of interaction of PV field with biological matter will be presented and, also, new perspectives of interaction with neuronal model cell populations will be described. Moreover, some results on Quantitative Phase Imaging of neuronal culture on LN will be showed.

In Figure 1(a) and (b) Dielectrophoretic trapping for polymer and particles is showed, respectively. PV field are able to shape the PDMS directly on the surface of the crystal thus creating microchannel whose wall are made in PDMS while the bottom side is the crystal itself (Figure 1(a)). In this way the underneath crystal can also activate PV forces to trap particle flowing into the channels (Figure 1(b)). Shaping liquids\polymers directly on the surface of the active material has many advantages, the most important is the avoiding of bonding process of fabrication thus reducing the percentage of leaking at the interfaces. The strength and the physical extension of PV fields allow to extend its applicability also bio-medical field. In Figure 1(c) it's displayed the trapping and orienting of E. coli bacteria on iron doped LN. The percentage of alignment changes depending on the characteristic length of the induced space electric field, higher alignment percentage is reached when 25µm, and 100µm linear phase gratings are inscribed inside the crystal volume corresponding to similar characteristic lengths for the evanescent fields on the surface. The effect of the evanescent fields on the surface in case of x-cut LN or the exposed charges in case of z-cut LN have an important role also on the adhesion and migration features of adherent cells [5].

Furthermore, a new interplay of biological samples with LN samples is possible where single cells can be used as microlenses to transfer into LN their own phase imprint. Indeed single cells behave as bio-lenses with proper focal length and magnification and can be modeled as linear combination of Zernike polynomials. We demonstrate that Red Blood Cells behave as microlenses and can be used to focus light into LN substrate thus transferring into the material their phase signature.

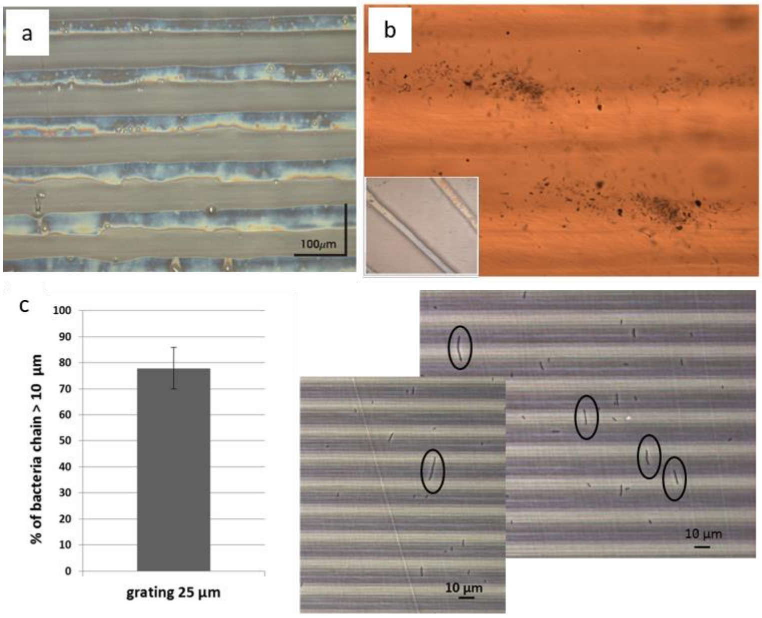

*Figure 1:* PV trapping of PDMS on LN surface thus creating all-optical fabricated microchannels. (b) the bottom side of the channel is still made by the LN crystal that behaves as active material to trap particle flowing inside. Also in this case the trapping is induced optically. (c) Immobilization and orientation of Escherichia Coli bacteria under the effect of PV fields.

## Conclusions

PV trapping is possible on the surface of ferroelectric crystals thanks to the PV effect. Liquid\polymer shaping and microparticle trapping has been demonstrated by all-optical approaches. Recently, the possibility to use LN substrate for cell culturing has been investigated by studying the biocompatibilities of doped or undoped crystals also in relation to the intrinsic polarization. Moreover the handling of biological matter has been demonstrated such as in case of passive immobilization and orientation of bacteria by exploiting the PV fields. The active interaction of single cell with LN has been also provided by developing a bio-photo-lithographic approach that uses Red Blood Cells to imprint phase modulation in the LN crystals. The development of LN platforms for cell manipulation would be revolutionary to address reconfigurable electric cues thus providing an intelligent culturing substrate.

## Acknowledgement

The work is supported by PRIN 2022 – ASSONE - All-optical Stimulation and Sensing Of Neurons on fErroelectric platform; (CUP MASTER C53D23000360006; CUP B53D23002390006; “founded by European Union – Next Generation EU”;

## References

[1] F. Agulló-López. Fundamentals of photorefractive phenomena, vol. 113, (2006).

[2] M. Esseling, Appl. Phys. Lett. 103, 6, (2013).

[3] L. Miccio et al. Lab Chip 12, 4449–54, (2012).

[4] L. Miccio et al ACS Applied Bio Materials 2 4675-4680 (2019).

[5] V. Marchesano. ACS Appl. Mater. Interfaces 7, 18113–18119, (2015).

# Long-lived, pulse-induced absorption in $LiNb_{(1-x)}Ta_xO_3$ solid solutions: the case of three intrinsic defect sites for electron localization with strong coupling

**Niklas Dömer** [a], Julian Koelmann [a], Anton Pfannstiel [a], Steffen Ganschow [b], Mirco Imlau [a]

[a] University of Osnabrueck
[b] Leibniz-Institut für Kristallzuechtung (IKZ), Berlin

mirco.imlau@uni-osnabrueck.de

Femto- and nanosecond pulse-induced, red and near-infrared transient absorption in $LiNb_{1-x}Ta_xO_3$ (LNT) solid solutions is studied with the goal to probe the intrinsic defect structure via the formation, transport and recombination of small bound electron polarons[1]. The resulting long-lived transients in LNT exhibit lifetimes orders of magnitude longer compared to those in congruent $LiNbO_3$ (LN, x=0) and congruent $LiTaO_3$ (LT, x=1), indicating a significant influence of the composition on the polaron dynamics. LNT might provide the possibility to control the optical and especially polaron-based photorefractive properties of a crystal through its composition between the photorefractive edge compositions LN and LT.

For this purpose, small polaron densities are generated in LNT on (ultra-)short time scales via two-photon absorption using short, intense pump laser pulses in the blue-green spectral range (photon energy $E_p$=3.1 eV, pulse duration $\tau_p \approx 50$ fs and $E_p$=2.33 eV, $\tau_p \approx 6$ ns) while the relaxation kinetics are probed with continuous-wave laser light in the red and near-infrared spectrum ($E_{probe}$ = 1.6 eV/1.96 eV) on time scales from $10^{-8} - 10^{2}$ s. The transmitted signal was recorded using Si-PIN photo diodes, connected to a fast digital storage oscilloscope. The obtained transients for LN and LT at 290 K and LNT for the composition x ≈ 50% are depicted in Figure 1a. The straight lines (black) represent the results of a fitting procedure using stretched exponential decay functions.

Long-lived transients are uncovered with lifetimes of τ ≈ 350 ms (LNT, x ≈ 50%), that are by a factor of up to 40 larger in comparison with the widely studied near-infrared transients. The fitted lifetimes are plotted in an Arrhenius plot (Figure 1b) for LN, LT and LNT in comparison. Here the activation energies are found in the range of (0.60 ± 0.05) eV for all three samples. The 1/e lifetimes measured with the ns-setup are depicted in the insert of Figure 1b and show a dramatic increase for the solid solutions.

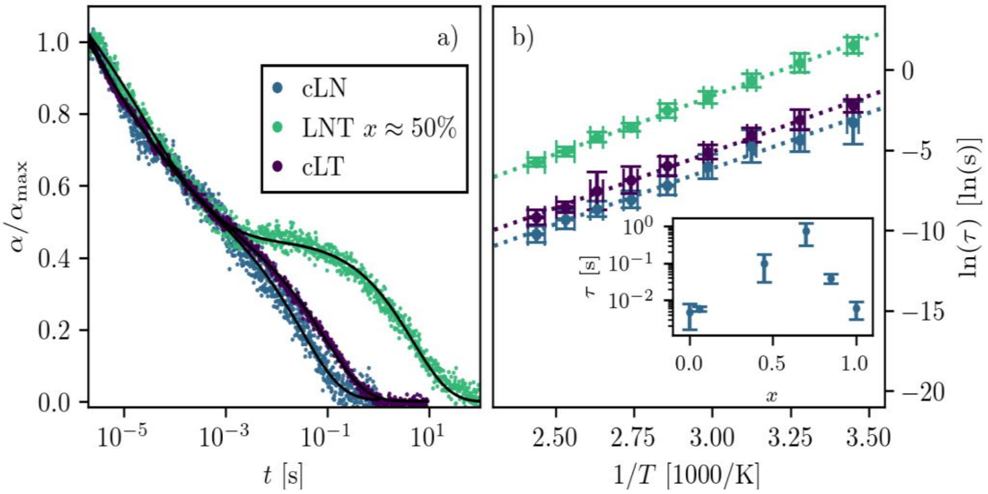

Figure 1: a) Transients of cLN, cLT and LNT with x ≈ 50% at T = 290 K upon fs-pulse exposure and probe light at wavelength of 633 nm. b) Lifetime τ as a function of temperature T in an Arrhenius plot for cLN, cLT and LNT. The insert shows the 1/e-lifetimes of the transient absorption signal as a function of composition.

The transients of different LNT samples are depicted in Figure 2 as a function of temperature (compositions: a: x ≈ 6%, b: x ≈ 50%, c: x ≈ 89%), showing that all samples of different composition show Arrhenius-like recombination behavior.

The starting amplitudes of LNT are determined in the range of $\alpha^0_{li} \approx 10 - 100\ \mathrm{m}^{-1}$ depending on the composition x and, thus, exceed those of congruent LN and congruent LT by a factor of up to ten [1]. The results of LN and LT are interpreted in the well-established model of three-dimensional small polaron hopping transport considering one type of small bound polaron in LN ($Nb_{Li}^{4+}$), two types in LT ($Ta_{Li}^{4+}$, $Ta_V^{4+}$) [2] and the simultaneous presence of all three types in the solid solutions. The coexistence of these defect sites in LNT leads to a complex landscape for polaron formation and transport, affecting the recombination dynamics and resulting in the observed long-lived transients.

We conclude that the differences between LNT, LN, and LT may be interpreted by changes in the 3D hopping transport mechanisms due to a different number of intrinsic defect centers, i.e. model systems consisting of one (LN), two (LT) and three (LNT) intrinsic defect centers for electron localization [2]. This unique, composition-dependent behavior suggests that LNT could serve as a versatile material platform for photonic applications where defect engineering and control of polaron dynamics are crucial.

Funded by DFG FOR5044 (Grant No. 426703838, IM37/12-1).

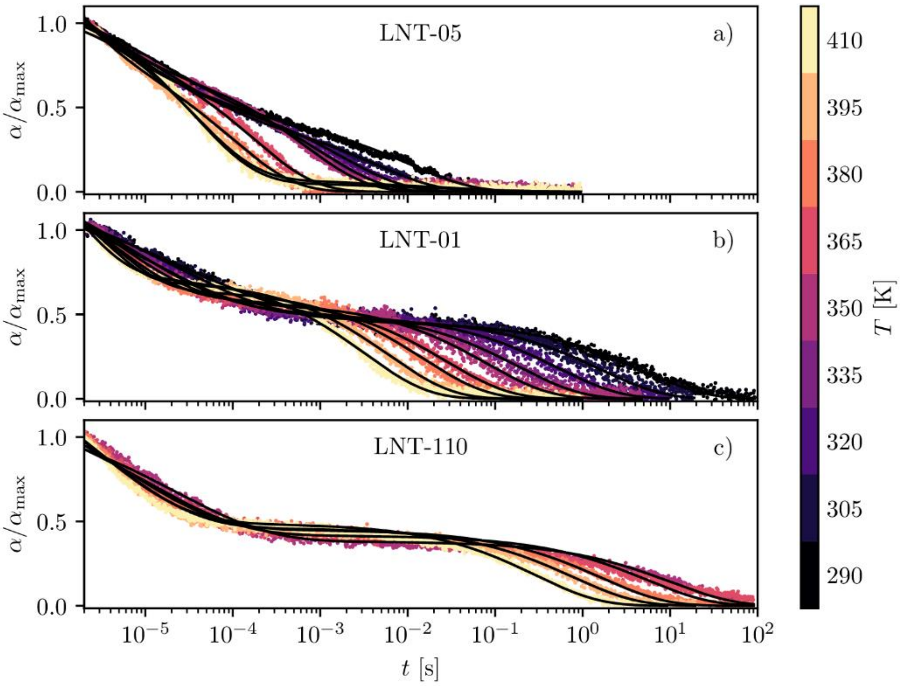

Figure 2: temperature dependent transients of LNT samples of different composition:
a: x ≈ 6%, b: x ≈ 50%, c: x ≈ 89%.

## References

[1] N. Dömer, J. Koelmann, M. Hesselink, T. Hehemann, A. Pfannstiel, J. Klenen, F. Sauerwein, Laura Vittadello, S. Ganschow and M. Imlau: Long-lived, pulse-induced absorption in $LiNb_{1-x}Ta_xO_3$ solid solutions: the case of three intrinsic defect sites for electron localization with strong coupling. https://doi.org/10.48550/arXiv.2403.16274 (2024)
[2] A. Pfannstiel, T. Hehemann, N. Schäfer, S. Sanna, Y. Suhak, L. Vitadello, F. Sauerwein, N. Dömer, J. Koelmann, H. Fritze and M. Imlau: Small electron polarons bound to interstitial tantalum defects in lithium tantalite. Journal of Physics: Condensed Matter (2024)

# "Lithium Niobate Integrated Circuits for Optical Microcombs: Science, Technology and Applications"

**Arnan Mitchell** [a,b],

[a] ARC Centre of Excellence in Optical Microcombs for Breakthrough Science (COMBS)
[b] School of Engineering, RMIT University, Melbourne, Victoria 3001, Australia

* arnan.mitchell@rmit.edu.au

Optical frequency combs were invented more than 20 years ago and have revolutionized precision measurement [1]. Their significance was recognized with the award of the 2005 Nobel Prize in physics, but since then have remained largely within sophisticated laboratories. Recent advances have made it possible to realize optical frequency combs in the form of micro-chips which can be manufactured cheaply, are compact and efficient [2]. The science and technology of microcombs is advancing rapidly but as these platforms become established and begin to standardize, it is the potential of these platforms to transform a diverse array of applications that becomes the new frontier.

Our team has been exploring the applications of optical microcombs for nearly a decade [3]. We have pioneered the use of microcombs for photonic signal processing and have shown record breaking data transmission and pattern recognition capabilities [4].

Silicon nitride has been the platform of choice for microcombs due to its strong waveguide confinement, extraordinarily low optical loss and compatibility with existing silicon electronics manufacturing infrastructure [2]. Thin-film lithium niobate has emerged as a platform that can offer similar confinement, compactness and optical loss but can also offer electro-optic, acousto-optic and nonlinear optical properties [5] which could offset the more specialized manufacturing requirements.

We have recently established a major research center to advance the science and technology of optical microcombs and explore the diverse opportunities for their application. This talk will present an overview of the research of our microcombs centre and will particularly compare silicon nitride and lithium niobate as photonic integration platforms for microcomb systems as well as an outlook for industrialization.

## References

[1] S.A. Diddams, K. Vahala, T. Udem "Optical frequency combs: Coherently uniting the electromagnetic spectrum," Science 369, eaay3676 (2020)

[2] D.J. Moss, R. Morandotti, A.L. Gaeta, M. Lipson "New CMOS-compatible platforms based on silicon nitride and Hydex for nonlinear optics," Nat. Phot. 7, 597-607 (2013)

[3] Y. Sun, J. Wu, M. Tan, X. Xu, Y. Li, R. Morandotti, A. Mitchell, D.J. Moss "Applications of optical microcombs" Adv. Optics and Phot. 15, 86-175 (2023)

[4] X. Xu, M. Tan, B. Corcoran, J. Wu, A. Boes, T. Nguyen, S. Chu, B.E. Little, D. Hicks, R. Morandotti, A. Mitchell, D.J. Moss "11 TOPS photonic convolutional accelerator for optical neural networks" Nature 589, 44-51 (2021)

[5] I. Kabakova, J. Zhang, Y. Xiang, S. Caponi, A. Bilenca, J. Guck, G. Scarcelli "Brillouin microscopy". Nature Reviews Methods Primers. 4, 8 (2024)

# Ferroelectric Domain Control of Second Harmonic Generation in $MoS_2$-$LiNbO_3$ heterostructures

**M.O Ramírez** [a,b,c], D. Hernández-Pinilla [a,b], M. Cherta [a], C. Hernando [a], G. López-Polin [a,c] , L.E Bausá[a,b,c]

[a] Dept. Física de Materiales, Universidad Autónoma de Madrid, Madrid, Spain
[b] Instituto de Ciencia de Materiales “Nicolás Cabrera” (INC), Madrid, Spain
[c] Condensed Matter Physics Center (IFIMAC), Universidad Autónoma de Madrid, Madrid, Spain

* mariola.ramirez@uam.es

The atomically thin nature of 2D-Transition Metal Dichalcogenide materials (TMDs) offers unprecedented control to adjust their optoelectronic properties by external fields. Among the different approaches, an actively pursued strategy is based on the integration of these low-dimensional materials on ferroelectric substrates. The remnant spontaneous polarization inherent to ferroelectrics offers intriguing interaction mechanisms to locally modulate the physical properties of ultrathin 2D materials and add desired functionalities for the next-generation photonic and opto-electronic functional 2D devices [1,2]. However, despite intensive research on their electrical and linear optical properties, the nonlinear optical performance of 2D/ferroelectric heterostructures remains almost unexplored.

Here, we show the possibility to spatially modulate the quadratic Second Harmonic Generation (SHG) of monolayer $MoS_2$ through the underneath spontaneous polarization provided by a periodically poled $LiNbO_3$. Different factors affecting the SHG spatial modulation such as the fundamental wavelength, pump power and polarization of the incident light will be discussed with particular emphasis on the role of light induced interfacial charge-transfer processes in TMDs based ferroelectric heterostructures.

The results contribute to the fundamental understanding of the nonlinear properties of TMDs under external stimuli and offer additional insights for the electrical control of harmonic generation in ultrathin integrated devices.

## References

[1] Q. Liu, S. Cui, R. Bian, E. Pan, G. Cao, W. Li, F. Liu, ACS Nano, 18, 1778, (2024)
[2] T. Jin, J. Mao, J. Gao, C. Han, K. P. Loh, A. T. S. Wee, W. Chen, ACS Nano, 16, 13595, (2022).

# Enhancement of the second harmonic generation using Mie and photonic crystal resonance in Silicon surfaces

Kotaro Ueda [a], Soki Hirayama [a], Ryushi Fujimura [a,b], **Tsutomu Shimura** [a]

[a] Institute of Industrial Science, The University of Tokyo, Japan
[b] Graduate School of Regional Development and Creativity, Utsunomiya University, Japan

* shimura@iis.u-tokyo.ac.jp

In silicon photonics, it is difficult to realize wavelength conversion devices due to the spatial inversion symmetry of silicon. We have attempted to enhance the surface second harmonic generation[1] in silicon using surface nanostructures. Using nanostructures similar to metasurfaces, we have numerically demonstrated that the efficiency of second harmonic generation can be significantly increased by simultaneously inducing Mie resonances at each meta-atom and photonic crystal resonances due to the two-dimensional arrangement of meta-atoms. The structure consists of a two-dimensional array of submicron-order amorphous silicon equilateral triangular prisms on a silicon dioxide substrate. Finite-element methods and FDTD were used for the simulations. First, we determined the conditions under which the total scattering cross section is maximized when a plane wave of wavelength 1500 nm is incident from directly above, and found the height and bottom size conditions of the equilateral triangular columns. It is assumed that the wavelength that gives the peak scattering cross section coincides with that of the Mie resonance peak. Next, the equilateral triangular prisms obtained here were arranged in a two-dimensional rectangular lattice, and the lattice spacing in the x- and y-directions was varied to search for the condition that maximizes the second harmonic generation efficiency. As a result, it was found that an increase in the second harmonic generation efficiency of about five orders of magnitude at the maximum was realized. It was found that the two-dimensional array of meta-atoms functions as a photonic crystal and resonance occurs at the Γ point.

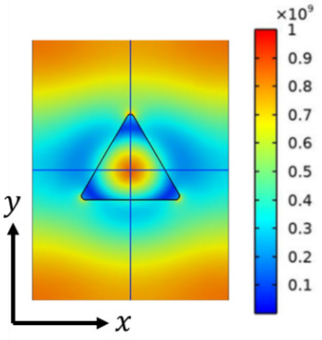

*Figure* Enhanced optical field of fundamental frequency by Mie and photonic crystal resonances. Incident light has y polarization.

## References

[1] Y. R. Shen, Annu. Rev. Phys. Chem., **40** 327-350 (1989)

# Nonlinear optical properties of low dimensional alkali niobates

**L. Vittadello** [a,b], F. Sauerwein [a,b], J. Klenen [a,b] and M. Imlau [a,b]

[a] Institute of Mathematics/Informatics/Physics, Osnabrueck University
[b] Research Center for Cellular Nanoanalytics, Osnabrueck, Osnabrueck University

* laura.vittadello@uni-osnabrueck.de

The recent progress in the synthesis methods made available today in nano form well-established photorefractive crystals like LiNbO$_3$ (LN), KNbO$_3$ (KN) and LiTaO$_3$ (LT). The new synthesis routes allow for nanosized niobate and tantalate structures of different dimensionality (nanodots: D=0; nanorods: D=1; ultrathin films: D=2) at a high degree of crystallographic quality. This includes nanocrystallites with sizes down to 10 nm as well as more complex periodic arrangements in the form of two-dimensional photonic crystals [1]. The growing interest for these materials is rooted in their multi-faceted, pronounced physical characteristics, such as ferroelectric, photovoltaic, piezoelectric, photovoltaic and nonlinear optical properties and the related applications in various fields. For instance, nonlinear optics with nanosized crystals allows for a unique type of multiphoton imaging (non-bleaching, non-blinking, high-contrast, gap-free tuning, etc.) where established and widely applied fluorescent nanomarkers fail [2,3]. Moreover, an additional use of the (bulk) photovoltaic effect could be promising in the context of optogenetics, e.g. in the framework of a manipulation of cellular environments via photo-induced electrostatic fields.

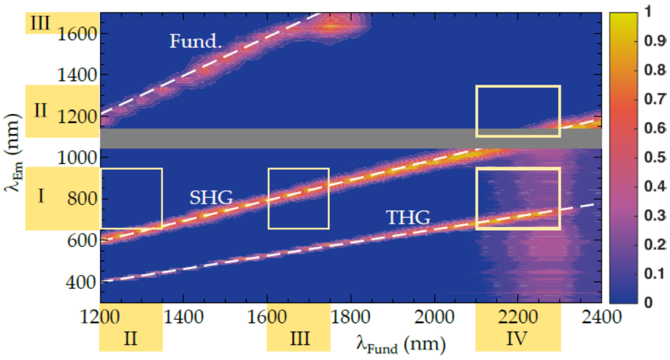

Fig. 1: Normalized intensity of the harmonic emission obtained for LN:Mg nanoparticles in the wavelength range from 266 - 1720 nm as a function of the pump wavelength in the range from 1200 - 2400 nm [4].

Among all the cited effects, we here focus on the nonlinear optical one based on second and third harmonic generation (SHG and THG). The results reported in Fig. 1, combined with the one of Ref [3], demonstrate that these two effects can be excited in nanoparticles continuously in the wavelength range of $800 < \lambda_{\mathrm{Fund}} < 2400$ nm. SHG is then generated continuously in the range of $400 < \lambda_{\mathrm{Em}} < 1200nm$ while THG in the range of $400 < \lambda_{\mathrm{Em}} < 800nm$.

The yellow boxes marked in Figure 1 correspond to the four biological optical windows (NIR-I to IV), that are spectral regions with comparable low transmission loss and, thus, of high interest for deep tissue applications. It is worth to note that only few biocompatible nanomaterials can be excited via wavelengths belonging to the NIR-III range and up to now only niobate materials can be excited in NIR-IV, opening the use of this unexplored biological window. The results show that also SHG and THG can be generated in the three optical windows NIR-I, II and III, i.e., contrary to most used nanomarkers which are still limited to light emission in the visible spectral regime, where the biological sample is absorbing at the most.

Nanocrystalline niobates therefore foster novel applications in the context of nanobiophotonics, here for in-vivo imaging [4,5] as an example. Indeed, the possibility to shift the excitation and emission wavelength far in the NIR, where the skin tissue shows reduced light scattering and absorption, contribute to perform deep-tissue imaging with the lowest light induced damage to the biological sample under study.

These properties can be extended from nanoparticles of zero deminsion to more complex structures, like nonlinear two-dimensional photonic crystals as depicted in Figure 2a). The structure presented here is made of $LiNbO_3$ on Indium Tin Oxide (ITO) having rims of ≈ 400nm which are surrounding holes with a diameter of ≈1µm. The thickness of the structure is 100 nm, i.e. in the sub-micron range. The image reports the SHG emission at a wavelength of 500 nm upon excitation to laser pulses at 1000 nm and acquired via a tunable high-energy (TIGER) nonlinear optical microscope [1]. As in the nanoparticle case, SH can be generated in the same extended wavelength range.

Such type of structure has several advantages. Indeed, despite of the optical features proper on photonic crystals, the holes allow for an easy functionalization with a conductive nanomaterial via electrodeposition. Figure 2b) shows that the coupling between $LiNbO_3$ and gold nanoparticles allows to increase the SHG output of a factor of 5 when the surface localized plasmon resonance of the gold is exploited.

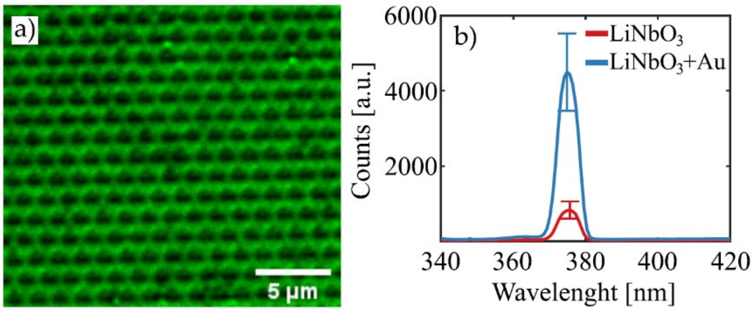

Fig. 2. a) SHG obtained with a nonlinear laser scanning microscope on nonlinear two-dimensional photonic crystals made of $LiNbO_3$. b) Spectroscopy SHG measurement prior and after gold electrodeposition in the holes of the structure presented in Fig. 2a).

Further examples of new synthesized low-dimensional alkali niobates and the respective unique photophysical properties will also be presented and discussed in respect of their potential for applications in various fields of optics and photonics.

(Funded by the Deutsche Forschungsgemeinschaft (DFG) within the research training group RTG2900 'nanomaterials@biomembranes' and research unit FOR 5022 'Periodic low-dimensional defect structures in polar oxides' (project IM37/12-1)).

**References**

[1] F. Alarslan, L. Vittadello, J. Klein, Q. A. Khan, C. Kijatkin, M. Haase, H. Schäfer, M. Imlau and M. Steinhart. Adv. Eng. Mater., 24: 2101159 (2022).

[2] L. Bonacina. Molecular Pharmaceutics, Vol. 10, No. 3 American Chemical Society (ACS) p. 783-792

[3] J. Vuilleumier, et al. Helvetica Chimica Acta, Vol. 103, No. 1 Wiley

[4] L. Vittadello, J. Klenen, K. Koempe, L. Kocsor, Z. Szaller, M. Imlau. Nanomaterials 2021, 11, 3193.

[5] L. Vittadello, C. Kijatkin, J. Klenen, D. Dzikonski, K. Kömpe, C. Meyer, A. Paululat, M. Imlau, Opt. Mater. Express 2021, 11, 1953

# Gap-free Tuning of Second and Third Harmonic Generation in Mechanochemically Synthesized nanocrystalline $LiNb_{1-x}Ta_xO_3$ Studied with Nonlinear Diffuse Femtosecond-Pulse Reflectometry

J. Klenen [a,b], **F. Sauerwein** [a,b], L. Vittadello [a,b], K. Kömpe [b,c], V. Hreb [d], V. Sydorchuk [e], U. Yakhnevych [d], D. Sugak [d,f], L. Vasylechko [d] and M. Imlau [a,b]

[a] Department of Mathematics, Informatics and Physics, Osnabrueck University, Barbarastraße 7, 49076 Osnabrueck, Germany
[b] Research Center for Cellular nanoanalytics, Osnabrueck (CellNanOs), Osnabrueck University, Barbarastraße 11, 49076 Osnabrueck, Germany
[c] Department of Biology/Chemistry, Osnabrueck University, 49076 Osnabrueck, Germany
[d] Department of Semiconductor Electronics, Lviv Polytechnic National University, 79013 Lviv, Ukraine
[e] Institute for Sorption and Problems of Endoecology, National Academy of Sciences of Ukraine, 13 Gen. Naumov St., 03164 Kyiv, Ukraine
[f] Scientific Research Company 'Electron-Carat', 79031 Lviv, Ukraine

* felix.sauerwein@uni-osnabrueck.de

The gap-free tuning of second (SHG) and third (THG) harmonic emission is studied in the model system $LiNb_{1-x}Ta_xO_3$ between the established photorefractive edge compositions lithium niobate ($LiNbO_3$, x=0, LN) and lithium tantalate ($LiTaO_3$, x=1, LT) [1]. The purpose of our study is to demonstrate the existence of optical nonlinearities of the second and third order in the ferroelectric solid solution system, but also to address the question about the suitability of LNT in the field of nonlinear and quantum optics, in particular as a promising nonlinear optical material for frequency conversion with tunable composition.
For this purpose, harmonic generation is studied in nanosized crystallites of mechanochemically synthesized LNT using nonlinear diffuse reflectometry with wavelength-tunable fundamental femtosecond laser pulses from 1200 nm to 2000 nm. As a result, a gap-free harmonic emission is observed (cf. Fig. 1 for $LiNb_{0.5}Ta_{0.5}O_3$,).

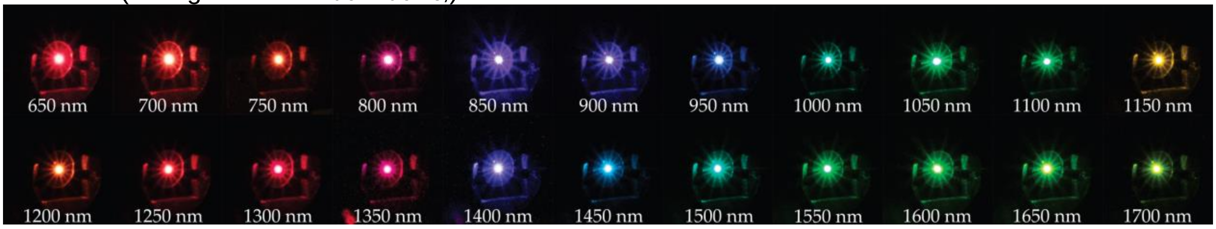

**Figure 1:** Digital images of diffuse remission of $LiNb_{0.5}Ta_{0.5}O_3$ nanoparticles under exposure to a train of fs-pulses tuned from 650 to 1700 nm in steps of 50 nm. The respective fundamental wavelengths are given below each image.

The interplay of simultaneous second and third harmonic emission is validated by the spectral inspection of the emission (cf. Fig. 2 left) for fundamental pulses between 1200 and 2000 nm. The intensity dispersion of the second harmonic signal (cf. Fig. 2 right) demonstrates the tuning of the harmonic emission from 1200 nm to 1800 nm without any resonance behavior [3] or gap. Fitting all individual dispersion features according to $I_{SHG} \propto 1/(\lambda - \lambda_{GAP})^m$ validates $m \gg 2$ for the experimental dataset as expected from theory based on the interplay of the wavelength dependencies of the second-order susceptibility tensor, the indices of refraction for fundamental and harmonic waves as well as the fundamental wavelength itself.

While the accurate modeling of the absolute intensity dispersion behavior requires further theoretical, especially numerical, efforts, the intensity dependencies $\boldsymbol{I_{(SHG,THG)}(I_{FUND})}$ can be analysed by the simplified relations $\boldsymbol{I_{SHG} \propto I_{FUND}^2}$ and $\boldsymbol{I_{THG} \propto I_{FUND}^3}$ as demonstrated in Figure 3 (left) for the LNT composition $\boldsymbol{x = 0.5}$ and $\boldsymbol{\lambda_{FUND} = 1400\ nm}$. Simultaneously, one can apply the intensity dependence to calculate the harmonic ratio $f_R$ as a reliable indicator for the polarity of the crystal symmetry and indicates polar symmetry if $\boldsymbol{f_R \gg 1}$ [2]. In our case (cf. Fig.3 right) $\boldsymbol{f_R \gg 10^6}$ is observed for all intensities and compositions, i.e., a clear indication for the presence of a ferroelectric polarization in the LNT nanoparticles can be concluded.

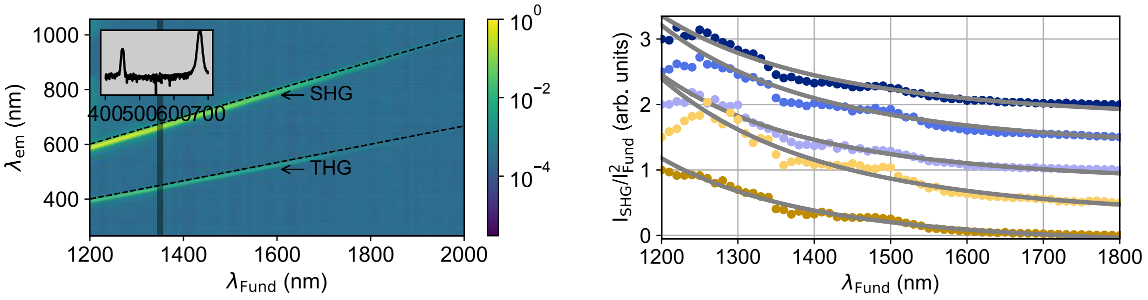

**Figure 2:** Left: Two-dimensional colormap measurements of $LiNb_{0.5}Ta_{0.5}O_3$. The inset shows the remission spectrum at a fundamental wavelength of 1350 nm. Right: Intensity dependence of the second harmonic signal as a function of the fundamental wavelength $\lambda_{Fund}$ for all compositions. The five plots were mutually displaced to each other along the signal axis.

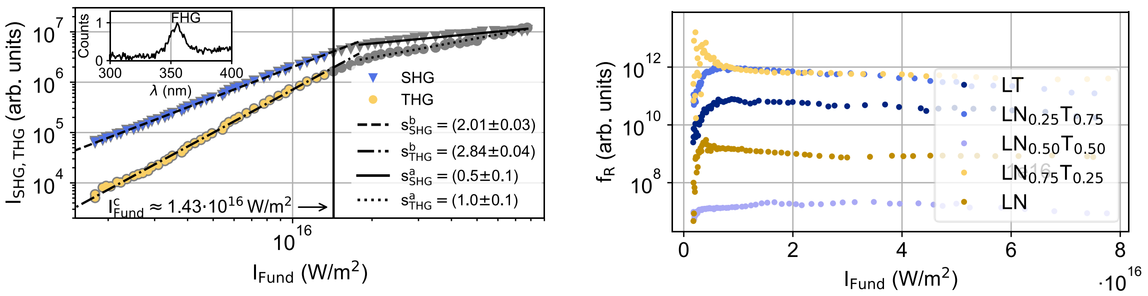

**Figure 3:** Left: Intensity dependence of SHG and THG of $LiNb_{0.5}Ta_{0.5}O_3$ at a fundamental wavelength of 1400 nm: The values of the derived slopes correspond with the exponent inside the power dependence of the harmonic generation. Right: Harmonic ratio $f_R$ at a fundamental wavelength of 1400 nm [1].

According to the polar characteristics of the LNT nanoparticles, the harmonic ratio resembles the volume nature of the harmonic generation, and it cannot be attributed to surface SHG effects. Considering the present work, we assume that findings on the dispersion features can be transferred to bulk crystals without restriction. However, the complex extrinsic and intrinsic defect structure, including defect clusters, may affect the magnitude of the nonlinear optical response. Compared with the edge compositions LN and LT, all results are found in accordance with the expectations. The recently reported success in poling LNT represents a further step towards promising applications in the field of nonlinear optics [3]. Hence, we can conclude that LNT is particularly attractive for applications in nonlinear optics that benefit from the possibility of a composition-dependent control of mechanical, electrical, and/or optical properties.

The authors acknowledge funding of the work by the Deutsche Forschungsgemeinschaft (DFG) within the research group “*Periodic low-dimensional defect structures in polar oxides*”, FOR 5044, project IM37/12-1.

## References

[1] J. Klenen, F. Sauerwein, L. Vittadello, K. Koempe, V. Hreb, V. Sydorchuk, U. Yakhnevych, D. Sugak, L. Vasylechko and M. Imlau, Gap-Free Tuning of Second and Third Harmonic Generation in Mechanochemically Synthesized Nanocrystalline $LiNb_{1-x}Ta_xO_3$ ($0 \leq x \leq 1$) Studied with Nonlinear Diffuse Femtosecond-Pulse Reflectometry, *Nanomaterials*, **14**, 317 (2024)

[2] C. Kijatkin, J. Eggert, S. Bock, D. Berben, L. Oláh, Z. Szaller, Z. Kis and M. Imlau, Nonlinear Diffuse fs-Pulse Reflectometry of Harmonic Upconversion Nanoparticles, *Photonics*, **4**, 11 (2017)

[3] F. Alarslan, L. Vittadello, J. Klein, Qaiser A. Khan, C. Kijatkin, M. Haase, H. Schäfer, M. Imlau, M. Steinhart, Thin Patterned Lithium Niobate Films by Parallel Additive Capillary Stamping of Aqueous Precursor Solutions, *Adv. Eng. Mater,*. **24**, 2101159 (2022)

[4] A.A. Mololkin, D.V. Roshchupkin, E.V. Emelin, R.R. Fahrtdinov, High-temperature poling treatment of congruent ferroelectric $LiNb_{0.5}Ta_{0.5}O_3$ solid solution single crystals, *Mod. Electron. Mater*, **7**, 17-20 (2021)

# Predator-prey behaviors in photorefractive solitons

**Juan Wu***, Yuhui Zhuang, Jiaxin Li, Siyu Li, Chenyang Zhan, Yi Hu, Jingjun Xu

The MOE Key Laboratory of Weak-Light Nonlinear Photonics, TEDA Applied Physics Institute and
School of Physics, Nankai University, Tianjin 300457, China

## Introduction

Chase-and-escape motion, typical behavior between a predator and a prey, is an important dynamic in living systems. It can be equivalently described by a two-body model, where one object attracts the other one, while the latter repels the former. This physical picture is found to be essential in various kinds of collective motion in biological phenomena, which further inspires people to synthesize predator-prey particles or droplets in inanimate matters, aiming to achieve life-like adaptive organizations and functionalities. In optics, light interactions also exhibit similar predator-prey dynamics. But thus far, this optical counterpart was realized only in one dimension, manifested as self-propulsion of two interacting light beam [1-4]. One possible challenge to realize its two-dimensional counterpart is that a sufficient nonlinear interaction is prevented in a long distance, because the self-defocusing nonlinearity experienced by one of the two interacting beams typically expands the beam and further weakens the nonlinear interactions.

## Result

In this work, by means of the photorefractive crystal applied alternative current voltage, we realize a photorefractive soliton mutually confined by two beams subject to a non-reciprocal interaction. Furthermore, we employ the realistic model [4] to study optical predator-prey dynamics in two transverse dimensions, as shown below:

$$i\frac{\partial \varphi_R}{\partial z} = -\frac{1}{2n_0 k_0}\nabla_\perp^2 \varphi_R - k_0 \Delta n \varphi_R, \tag{1a}$$

$$i\frac{\partial \varphi_F}{\partial z} = -\frac{1}{2n_0 k_0}\nabla_\perp^2 \varphi_F - k_0 \Delta n \varphi_F, \tag{1b}$$

where $\varphi_R$ and $\varphi_F$ are complex amplitudes of two interacting optical beams (accordingly denoted as R-beam and F-beam that play the roles of a prey and a predator, here typically represented by a rabbit and a fox, respectively), $\nabla_\perp^2$ is Laplace operator, $z$ is the propagation direction of the beams, $k_0$ is wavenumber in vacuum and $n_0$ is a linear refractive index. $\Delta n = \gamma |\varphi_R|^2 / 1 + |\varphi_R|^2 - \gamma |\varphi_F|^2 / 1 + |\varphi_F|^2$ ($\gamma$ is a nonlinear coefficient) is a nonlinear term that allows R-beam and F-beam to feel self-focusing and -defocusing nonlinearities, respectively. During nonlinear propagation, F-beam tends to be delocalized due to the self-defocusing nonlinearity, but one can employ the wave guiding effect of R-beam to confine it. The ideal condition is that the two beams are mutually confined to form a soliton, as presented in Fig. 1a. When the two components in the soliton are given a separation at the input, for instance, along the *x*-axis, they feel forces towards the same direction to support a chase-escape motion. That is because that R-beam, experiencing a self-focusing nonlinearity, induces a waveguide to attract F-beam, while F-beam, feeling a self-defocusing nonlinearity, induces an anti-waveguide to repel R-beam. Once one of the two beams is given an initial tilt, an oblique spiral dynamic takes place, exhibiting a travelling motion transversely (Fig. 1b, c). The spiral trajectory has a similar orientation with the initial tilt given to R-beam (Fig. 1b). In the other case of tilting F-beam only, the transverse travelling motion is reversed to the direction of the initially applied momentum (Fig. 2c), leading to a counterintuitive orientation of the oblique spiral trajectory.

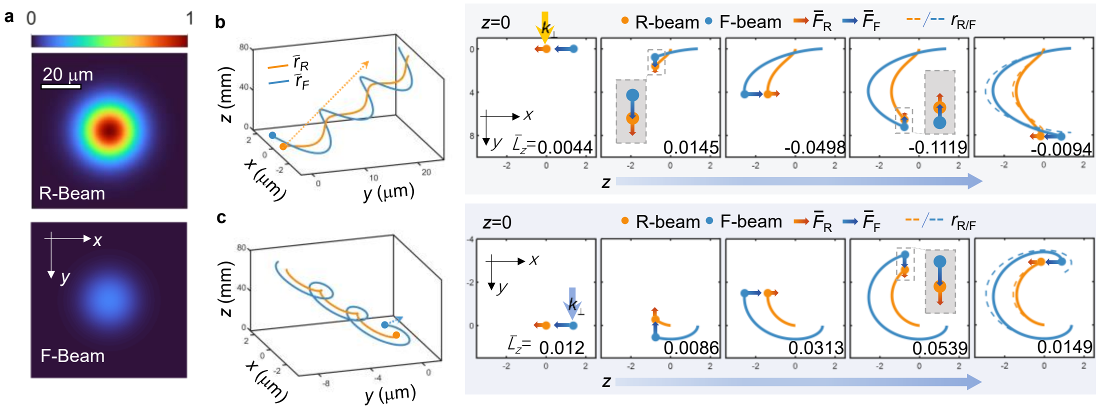

Figure 1: **a** A typical soliton solution where R- and F- beams are mutually confined. **b-c** Trajectories (solid, center-of-mass) of the beams under propagation with an initial separation and that **b** only R-beam or **c** only F-beam has initial tilts (i.e., $k_{\perp}$). $\bar{L}_z$ is total angular momentum of the two beams.

To verify "predator-prey" behaviors of two optical beams in experiment, we employ an experimental setup schematically shown in Fig. 2a. A digital micromirror devices (DMD), a spatial light modulator (SLM) and an alternating current (AC) voltage are used and their modulation are well synchronized. The time-dependent modulations uploaded in the DMD reshape a CW laser into two pulsed trains with different intensities. The pulsed beam with a higher (lower) intensity, denoted as R-beam (F-beam), synchronizes with the positive (negative) voltage, and thus experiences a self-focusing (-defocusing) nonlinearity. Each beam is individually imposed phase modulations via the SLM. Their intensity profiles are observed by a charge coupled device (CCD). Dut to the storage effect of the photorefractive crystals, the two beams can interact with each other. At first, we seek two beams experiencing inverted nonlinear dynamics to form a photorefractive soliton upon their interactions. Two beams without space presented in Fig. 2(b, c) are able to be mutually confined, exhibiting a localization along the propagation (Fig. 2d-g). To perform the predator-prey experiment, the two beams are separated in the *x*-axis at the input, and meanwhile, only one of them is applied with an initial tilt downwards. Upon interaction, they can undergo a counter-clockwise or a clockwise spiral propagation (Fig. 2h and Fig. 2i), agreeing with the simulation (Fig. 1b, c).

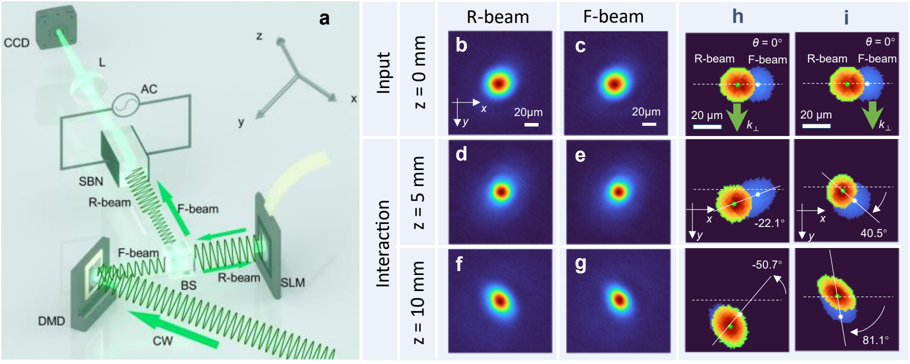

Figure 2: **a** Schematic experimental setup. **b-g** Measured intensity patterns (normalized) of R-beam (left column) and F-beam (right column) at different propagation distances under nonlinear interactions. **h-i** Spiral chase-and-escape motion of two optical beams in experiment for the cases of tilting only **h** R- or **i** F-beam at the input, respectively.

## References

[1]. Wimmer M, et al. Nat. Phys. **9**, 780-784 (2013).

[2]. Alberucci A, et al. Phys. Rev. A **100**, 011802(R) (2019).

[3]. Zhang P, et al. Phys. Rev. Lett. **127**, 083901 (2021).

[4]. Ma W, et al. Laser Photonics Rev. **17**, 220017 (2022).

# Photovoltaic High-throughput Microfluidic Platform for the Mass-Production of Hybrid Viscous Microdroplets Towards Diverse Applications

Mengtong Wang[1, 2], Xiaohu Liu[1, 2], Lihong Shi[3], Zuoxuan Gao[1, 2], Chenyu Li[1, 2], Zechao Huai[1, 2], Cheng Wang[1, 2], Jinghui Yan[1, 2], Lina Zhang[1, 2], Xuan Wang[1, 2], Wenbo Yan[1, 2, *]

[1] State Key Laboratory of Reliability and Intelligence of Electrical Equipment, School of Materials Science and Engineering, Hebei University of Technology, Tianjin 300130, China

[2] Hebei Engineering Laboratory of Photoelectronic Functional Crystals, School of Materials Science and Engineering, Hebei University of Technology, Tianjin 300130, China

[3] Department of Physics, Tianjin Chengjian University, Tianjin 300384, China

*Corresponding Author. E-mail: yanwenbo@hebut.edu.cn

## Summary

We present a photovoltaic MHTE platform to handle serial aqueous microdroplets dispersed in a continuous oil phase. By simply applying focused-laser illumination, we realize the sequential cascading of microfluidic manipulations, including trapping, coalescence, mixing, and release of microdroplets, in a reconfigurable, high-throughput manner. It is found that three cases, that is, Non-coalescence, Successful coalescence and Bouncing back of adjacent microdroplets dominate at the low ($I<I_{Min}$), moderate ($I_{Min}<I<I_{Max}$) and high ($I>I_{Max}$) illumination intensity, respectively. The suitable range of illumination intensity for microdroplet coalescence significantly changes with variations in surfactant and SA concentrations, owing to the steric hindrance effect of surfactant layers and the inhibition of microdroplet viscosity to the interface Rayleigh jetting. By properly adjusting the intensity of laser illumination, we are able to control the number of the microdroplets participating in coalescence as well as the degree of the followed liquid mixing inside coalescent microdroplets, thus realizing the mass-production of hybrid viscous microdroplets. Besides, the residual photovoltaic field after the removal of laser illumination is also utilized for the microdroplet coalescence, which can be developed as a new mode of microdroplet coalescence with the capability to avoid direct laser illumination. To demonstrate the capability of the photovoltaic MHTE platform, Janus microparticles, processing magnetic property in one hemisphere and phosphorescent property in the other hemisphere, are massively prepared for assembling a magnetically driven displayer. This displayer, with reduced size and

enhanced magnetic sensitivity of the pixels, is expected to visualize the magnetic field with high resolution and accuracy. Moreover, uniformly sized bioreactors with both immobilized yeast cells for effective fermentation and embedded magnetic nanoparticles for convenient recovery, are also massively produced on this platform. It has been observed that over 70% of the activity of freely suspended cells can be maintained in the prepared bioreactors and about 85% of activity is retained after each cycling experiment. Additionally, based on the photovoltaic MHTE platform, we generate chains of fluorescent double-emulsion microdroplets for optically encoding the information of the target microdroplet. This encoding method avoids the undesirable contamination of the encoding materials encapsulated in unit microdroplets to the sample contained in the target microdroplet, meanwhile the code with multiunit and multilevel potentially allows to achieve a large encoding capacity. The present photovoltaic MHTE platform and the related optofluidic technique may find a large number of applications in diverse fields including optics, MEMS, biotechnology and chemical sciences.

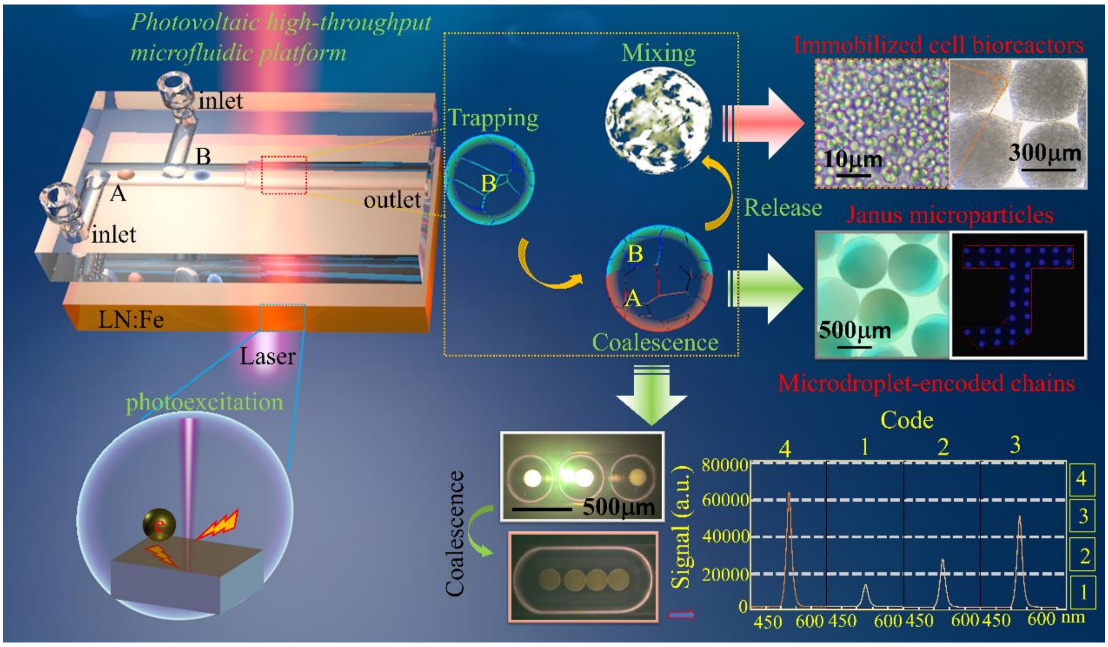

# Application of photorefractive liquid crystals to laser ultrasonics

**Takeo Sasaki**

Department of Chemistry, Faculty of Science, Tokyo University of Science,
1-3, Kagurazaka, Shinjuku-ku, Tokyo 162-8601, Japan
* sasaki@rs.tus.ac.jp

Laser ultrasonics using a photorefractive liquid crystal is investigated. The proposed laser ultrasonic method involves irradiating an object with a laser pulse to produce an ultrasonic vibration and then using another laser beam to detect the vibration. The phase of the laser beam reflected from the object is shifted by the ultrasonic vibration. This phase shift can be detected by using liquid crystals with photorefractive properties. Compared to traditional laser ultrasonic methods, this system offers a simpler optical setup and allows for more precise measurements that are unaffected by environmental vibrations. In this study, laser ultrasonic measurement experiments were carried out using optical setups in which pulsed and detection lasers irradiated opposite sides of an object (counter-optical setup) and the same side of the object (coaxial-optical setup), as shown in Fig. 1. In both setups, the ultrasonic vibration changes the phase of the reflected beam, which is detected by a photorefractive liquid crystal. It was found that the laser ultrasonics using an LC provides noise-free, highly sensitive measurement results. Optical systems that use LCs are simpler than those that use conventional interferometers, making them suitable for miniaturization.

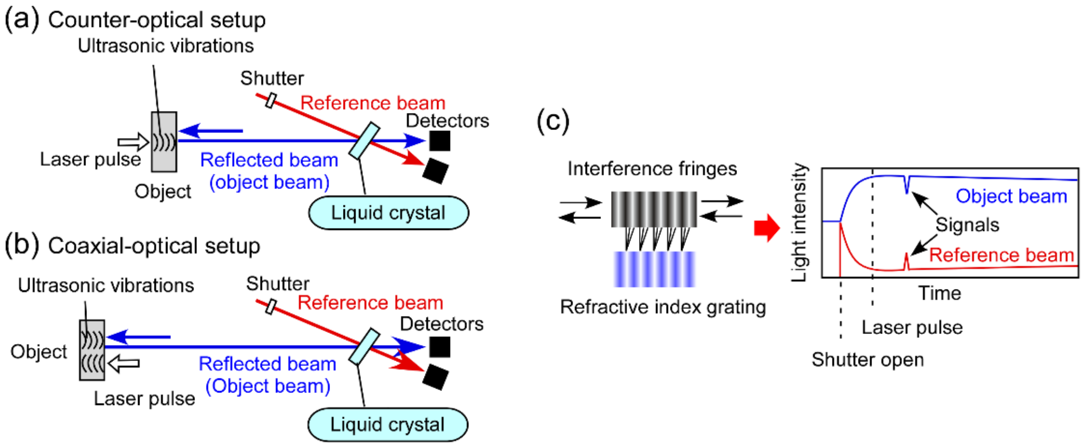

**Fig. 1.** (a) Optical setup for measuring thickness and shape of object by laser ultrasonics. (b) Optical setup used to irradiate pulsed light and probe laser from same direction; (c) Phase change due to acoustic vibration in object signal beam leads to changes in interference intensity via asymmetric energy exchange.

A photoconductive LC blend was used as a photorefractive material. The structures of the compounds used in the experiments are shown in Fig. 2(a). The base LC exhibited the following phase sequence: crystal → 6.4 °C → SmC → 48.1 °C → SmA → 59.4 °C → nematic → 67.6 °C → isotropic. As shown in Fig. 2(b), the LC mixture was sandwiched between two glass plates that were separated by 10 μm. The two glass plates have an indium tin oxide (ITO) electrode and a polyimide alignment layer (LX-1400, Hitachi Chemical). The thickness of the glass plate of a cell was 0.7 mm and the size of the ITO electrode was 10 mm$^2$. The surfaces of the polyimide coatings were rubbed in one direction with velvet cloth. As shown in Fig. 2(c), the polarizing direction of the laser beam was adjusted to the LC alignment direction in order to minimize the effect of the birefringence of the LC on the measurements. Figure 3 shows an example using an Al plate as the target object. The measurement results show many signals caused by the repeated reflection of ultrasonic vibrations on the front and back surfaces of the Al plate. Different from previously reported experimental results using polymers, noise-free and accurate measurements are possible, as shown in Fig. 3.

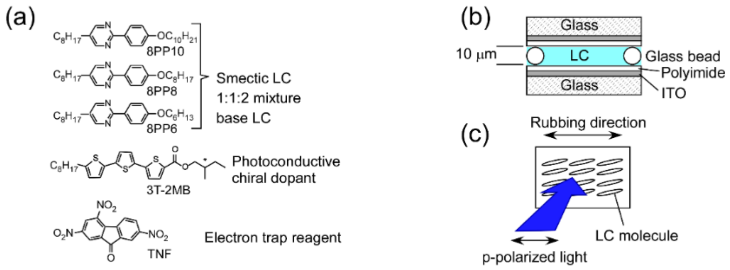

**Fig. 2.** (a) Structures of components of PR-flex LC mixture. The concentration of photoconductive chiral dye (3T-2MB) is 10 wt.% and the concentration of electron trap reagent (TNF) is 0.1 wt.%. (b) Structure of PR-flex LC cell. (c) Schematic diagram of p-polarized beam incidence in two-beam mixing experiment.

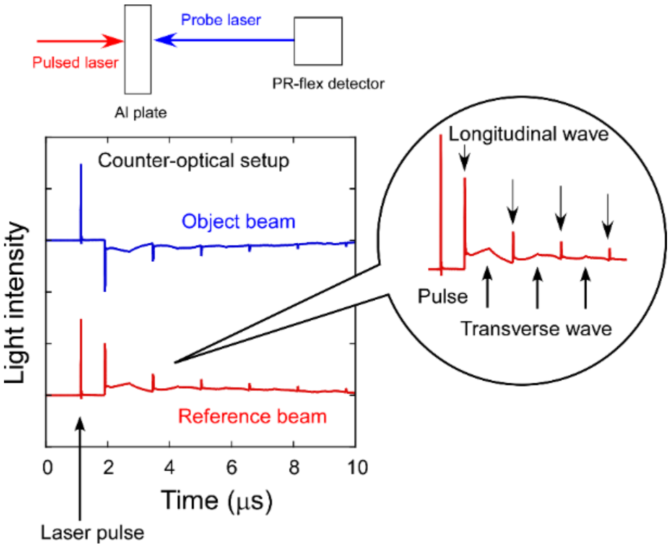

**Fig. 3.** Measured signal in ultrasonic non-contact measurement using counter-optical setup. The thickness of the aluminum plate was 2 mm. The intensity of the pulsed laser was 20 mJ/pulse. The diameter of the laser pulse was 3 mm.

Figure 4 shows the measurement results for a sample with a drilled cavity in the Al plate (Fig. 4(a)) for various laser irradiation locations. The surface of the plate was scanned in two dimensions and a three-dimensional image of the cavity inside the plate was obtained (Fig. 4(b)). A total of 121 points were measured (11 points in the x-axis direction × 11 points in the y-axis direction) and plotted in three dimensions. The existence of the cavity in the Al plate was clearly detected. The upper surface of the cavity was visualized. This method can only visualize the shape of the upper surface of the internal structure viewed vertically from above. Nevertheless, it can visualize the hidden structures inside an object and can measure the depth of the upper surface of an inner structure.

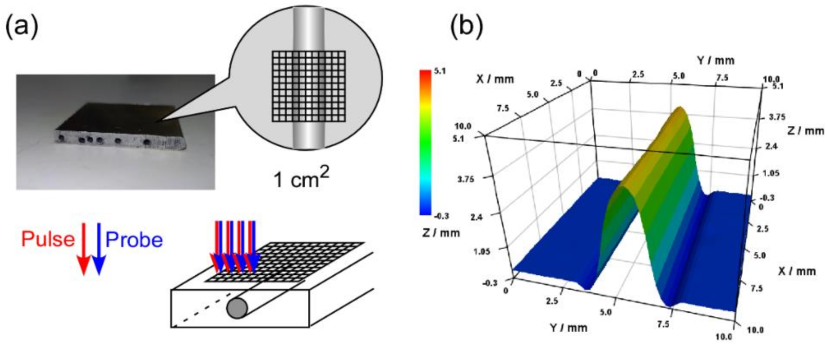

**Fig. 4.** (a) Photograph of aluminum plate with drilled cavity. The surface of the aluminum plate was scanned with lasers with a coaxial-optical setup. The scanned area was 10 mm square. The diameter of the pulse laser irradiation spot was 1 mm. (b) Three-dimensional plot of cavity inside aluminum plate measured by laser ultrasonics with coaxial setup.

## References

[1] Takeo Sasaki, et.al. *Opt. Mater. Express*, 13, 728-738 (2023)

# Photorefractive deceleration of light pulses at the visible and infrared wavelengths

Nacera Bouldja,[1,2] Alexander Grabar,[3] Marc Sciamanna,[1,2] Delphine Wolfersberger,[1,2]

[1]Chair in Photonics, CentraleSupélec, LMOPS, F-57070 Metz, France
[2]Université Lorraine, CentraleSupélec, LMOPS, F-57070 Metz, France
[3]Institute of Solid-State Physics and Chemistry, Uzhhorod National University,
Pidhirna 46,88000 Uzhhorod, Ukraine

Photorefractive (PR) crystals are considered among the most promising materials for studying the deceleration of the group velocity of light pulses at room temperature [1, 2, 3]. Their optical properties enable the exploitation of various nonlinear phenomena, such as beam fanning and two-wave mixing to manipulate the speed of long and short light pulses [4]. Due to these advantages, PR crystals can become indispensable materials in developing innovative future optical devices.

This work demonstrates that the PR crystal can decelerate the group velocity of light pulses over a broad spectrum of wavelengths. We illustrate that the beam fanning effect can slow down light pulses at different wavelengths, including 638 nm, 1064 nm, and 1310 nm. Additionally, we show that a 100 ns pulse can slow down by 25 ns at 1064 nm and by 10 ns at 1310 nm, respectively. Indeed, these pulses do not suffer from the same broadening observed in the visible regime with longer pulses.

The experiment uses a laser and a $Sn_2P_2S_6$ (SPS) PR crystal. The input pulse is modulated into a Gaussian shape using an electro-optical modulator and then propagates through the PR crystal along the z-direction. The same experimental configuration is used to investigate the deceleration of light pulses at various wavelengths (638 nm, 1064 nm, and 1310 nm). Initially, we adjust the rotation of the PR crystal so that the incident beam and crystal's c-axis form an incidence angle $\theta = 45°$, and we characterize the beam fanning of PR crystals versus the input power using Eq .2 [**?**]. An example of the obtained result at 1310 nm is plotted in Fig.1. We note that the depletion factor increases, reaching a maximum of 0.97 at an input power $P_0$=0.6 mW. Then its values decrease as the input power is further increased.

We present the experimental results that show the possibility of slowing down light pulses at different wavelengths using the beam fanning effect. Fig. 2 illustrates the time delays for pulses emitted by lasers at wavelengths $\lambda$= 638, 1064, and 1310 nm, respectively. We observe that at each wavelength, the time delay value increases with the input pulse width. Indeed, for $\lambda$=1310 nm, the crystal can slow down short light pulses ranging from nanoseconds to microseconds.

power). The following figures show examples of detection under self-stabilized background level.

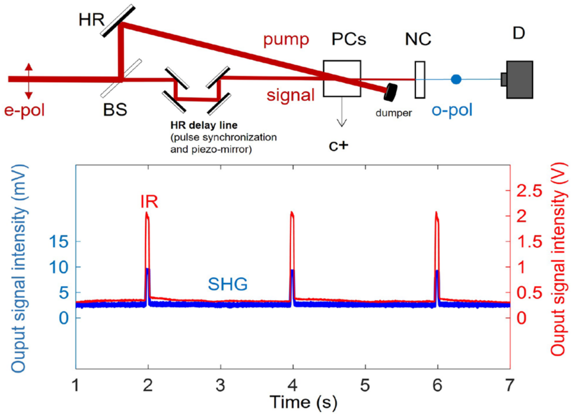

Fig. 1. Top: Scheme for IR-pumped fs OTD with output up-conversion. BS: beam-splitter. HR: high-reflector. PCs: photorefractive crystals. NC: nonlinear crystal for SHG. D: detector. Bottom: OTD of IR pulses with 2.5 rad phase variations.

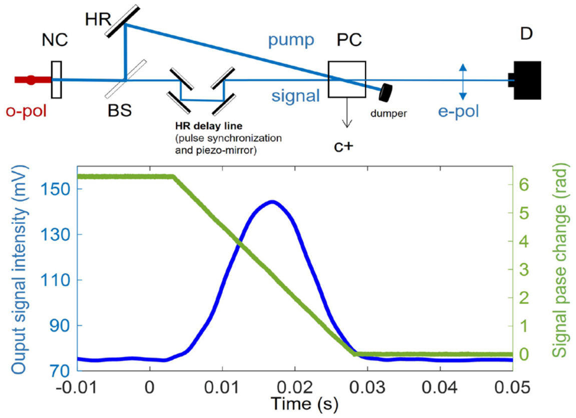

Fig. 2. Top: Scheme for visible-pumped fs OTD. BS: beam-splitter. HR: high-reflector. PC: photorefractive crystal. NC: nonlinear crystal. D: detector. Bottom: OTD of fast (~30ms) 2π signal-phase change (fit of Eq. 1 with a $R^2 = 0.993$).

## Conclusions

We have demonstrated photorefractive OTD with ultrafast lasers, providing background suppression and phase detections with femtosecond pulses, which is especially important for low-power small-phase change signals sensors. Moreover, we have evidenced the relation between output intensity-input phase change, in agreement with squared-sinusoidal type theoretical dependence. Finally, we must emphasize that the implementation of up-conversion schemes, opens up new possibilities by exploiting unsurpassed wavelength flexibility for both sampling and detection in OTD, which can be advantageous in case of living samples, and could be extended to imaging.

## References

[1] R. S. Cudney, R. M. Pierce, and J. Feinberg, “The transient detection microscope,” Nature **332**(6163), 424–426 (1988).
[2] V. V. Krishnamachari, O. Grothe, H. Deitmar, and C. Denz, ““Full-field particle velocimetry with a photorefractive optical novelty filter,” Appl. Phys. Lett. **87**(7), 071105 (2005).
[3] K. Shcherbin and M. B. Klein, “Adaptive interferometers with no external field using reflection gratings in CdTe:Ge at 1550 nm,” Opt. Commun. **282**(13), 2580–2585 (2009).
[4] A. Esteban-Martín, J. García-Monreal, F. Silva, and G. J. de Valcárcel, “Interferometric measurement of complex-field changes in transient detection imaging,” Optics Express **28**(20), 28782–28791(2020).
[5] Sukeert; S. Chaitanya Kumar; P.G. Schunemann; Germán J. de Valcárcel; M. Ebrahim-Zadeh; A. Esteban-Martín, “Up-converted photorefractive optical transient detection with femtosecond laser pulses,” Optics Express **31**(10), 16939-16951 (2023).

We acknowledge financial support from the Spanish Government through Projects PID2020-120056GB-C22 and PID2020-112700RB-I00 funded by MCIN/AEI/10.13039/501100011033.

# Photorefractive optical transient detection with femtosecond pulses

Sukeert[a], S. Chaitanya Kumar[b], P. G. Schunemann[c], G. J. de Valcárcel[d], M. Ebrahim-Zadeh[a,e], A. Esteban-Martín[d]

[a]ICFO—Institut de Ciències Fotòniques, The Barcelona Institute of Science and Technology, 08860 Castelldefels (Barcelona), Spain
[b]Tata Institute of Fundamental Research Hyderabad, 36/P Gopanpally, Hyderabad 500046, Telangana, India
[c]BAE Systems Inc., MER15-1813, P.O. Box 868, Nashua, NH 03061-0868, USA
[d]Departament d'Òptica i Optometria i Ciències de la Visió, Universitat de València, Dr. Moliner 50, 46100-Burjassot, Spain
[e]Institució Catalana de Recerca i Estudis Avançats (ICREA), Passeig Lluís Companys 23, Barcelona 08010, Spain

## Introduction

An optical transient detection (OTD) system, also known as optical novelty filter, is an adaptive interferometer that detects temporal changes while suppressing static background, improving contrast when measuring intensity and phase. Several systems have been implemented for many applications, including transient detection microscopy [1] as well as quantitative measurement of phase changes [2-4]. However, most OTD systems are based on photorefractive two-wave mixing in the visible range, and use continuous-wave lasers.

We report on experimental demonstration of OTD with femtosecond (fs) pulses. We explore two experimental setups based on an 805 nm KLM Ti:sapphire laser, providing ~130 fs pulses at 76 MHz. Coherent ultrafast lasers providing high-repetition-rate fs pulses are of interest for many applications and the high peak power of the ultrashort pulses further make possible up-conversion from infrared (IR) into the visible, enabling measurements with standard (GaP/Si) photodetectors.

The laser beam is split into a signal beam and a pump beam, which intersect in the photorefractive crystal, whose $c^+$-axis is oriented to get signal attenuation under steady-state operation, and any phase change, $\Delta\varphi_{in}$, produces a signal output intensity:

$$I^{out} = 4I^{ref}\, sin^2(\frac{\Delta\varphi_{in}}{2})\ , \qquad (1)$$

where $I^{ref}$, is determined by a fit on the dependence between the output intensity and the signal phase shifts, which we implement by means of a piezo-mirror.

The first setup (see Fig. 1) employs $BaTiO_3$ and SBN photorefractive crystals in tandem [5], which are pumped in the IR and SHG is achieved in $BiB_3O_6$ (BIBO) nonlinear crystal. Two crystals were needed to achieve an efficient suppression above 50%. And an input signal power of 100 mW (500 mW of pump power) was required to achieve detection in the visible. The second setup (see Fig. 2) makes use of a $BaTiO_3$ pumped directly in the visible. In this case, a suppression above 50% was achieved just with a single crystal (requiring only 1 mW of signal power and 100 mW of pump

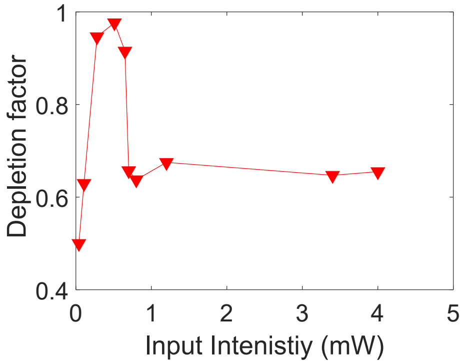

Figure 1: Experimental depletion factor D according to the input power at 1310 nm in the doped SB SPS crystal with thickness d = 1 cm.

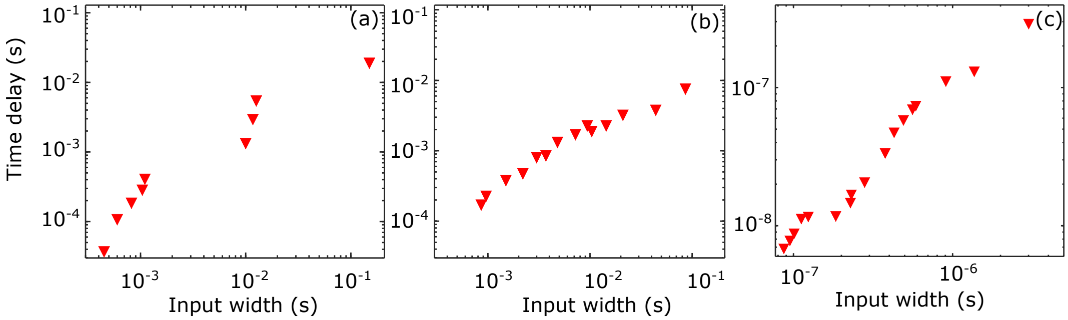

Figure 2: Experimental results of the time delay as a function of the input pulse duration for different wavelengths. a) for $\lambda$=638 nm, a 0.5 cm long doped Te SPS, and a depletion factor D=0.54. b) For $\lambda$=638 nm, a 0.5 cm long doped Te SPS, and a depletion factor D=0.94. c) For $\lambda$=638 nm, a 1 cm long doped SB SPS, and a depletion factor D=0.9.

In this paper, we demonstrated that the PR crystal can slow down short and large light pulses at different wavelengths using the beam fanning effect. We have demonstrated that the time delay can be controlled by varying the laser wavelengths and the input pulse duration of the laser.

## References

[1] N.Bouldja, A.Grabar, M.Sciamanna, D. Wolfersberger,Phys. Rev. Research 2, 032022. (2020).

[2] Podivilov, E., Sturman, B., Shumelyuk, A., Odoulov, S. Phys. Rev. Lett., (2003).

[3] N. Bouldja, M. Sciamanna, and D. Wolfersberger, Opt. Lett. 44, 1496-1499 (2019)

[4] N. Bouldja, M. Tsyhyka, A. Grabar, M. Sciamanna, and D. Wolfersberger, Phys. Rev. A 105, L021501 (2022).

# Two-beam energy exchange in a hybrid photorefractive-ferroelectric liquid crystal cell

**V. Yu. Reshetnyak** [a,b], I. P. Pinkevych [a], D. R. Evans [c]

[a] Physics Faculty, Taras Shevchenko National University of Kyiv, Kyiv 01601, Ukraine
[b] School of Physics and Astronomy, University of Leeds, Leeds LS2 9JT, United Kingdom
[c] Air Force Research Laboratory, Materials and Manufacturing Directorate, Wright-Patterson Air Force Base 45433, USA

* victor.reshetnyak@gmail.com

In recent years, significant progress has been made in studying energy transfer between light beams in hybrid systems consisting of a liquid crystal (LC) layer placed between two photorefractive windows. Incident intersecting light beams interfere and induce a spatially periodic space charge field in photorefractive windows. The photorefractive field penetrates the LC layer and modulates the LC director, creating the director grating. The light beams are diffracted by the director grating, leading to an exchange of intensity between beams and the amplification of one of them. In conventional LCs, the main mechanism responsible for the LC director modulation is the interaction of the photorefractive field with the LC flexoelectric polarization. In this case, the exponential gain coefficient can reach values significantly exceeding those in solid inorganic photorefractive crystals [1].

In this report, we theoretically study energy transfer between light beams in hybrid systems when a ferroelectric nematic liquid crystal (FLC) is placed between two photorefractive windows. FLCs are new photonic materials that can create real innovations in LC-based technologies [2-4]. Since one of the most striking characteristics of FLC is the presence of high values of electric polarization, much higher than the values of flexoelectric polarization, it can be assumed that the main mechanism of director grating formation in FLC based hybrid systems is the interaction of the photorefractive field with the FLC polarization.

To study the equilibrium director profile in the FLC cell we take the total free energy functional of the FLC cell in the form

$$F = F_{el} + F_p + F_S, \quad F_{el} = \frac{1}{2}\int\left[K_{11}\left(\nabla\cdot\mathbf{n}\right)^2 + K_{22}\left(\mathbf{n}\cdot\nabla\times\mathbf{n}\right)^2 + K_{33}\left(\mathbf{n}\times\nabla\times\mathbf{n}\right)^2\right]dV,$$

$$F_p = -\int\left(\mathbf{P}\cdot\mathbf{E}\right)dV, \quad F_S = -\frac{1}{2}W\sum_{i=1}^{2}\int\left(\mathbf{n}\cdot\mathbf{d}_i\right)^2 dS_i,$$

where $F_{el}$ is the bulk elastic energy of a distorted FLC layer, $F_p$ is the contribution from the interaction of the photorefractive field $\mathbf{E}$ that penetrated into the FLC cell with the FLC polarization, $F_S$ is the surface term describing the interaction of the director with the FLC cell substrates, $K_{11}, K_{22}, K_{33}$ are the splay, twist and bend elastic constants, respectively, $\mathbf{n}$ is the FLC director, $\mathbf{P}$ is a vector of the FLC polarization, $\mathbf{d}_i$ is a unit vector of the director easy axis at the cell substrates.

The electric field $\mathbf{E}$ in the FLC cell can be found from the Poisson equation. Then minimizing the free energy $F$ one can obtain equations for the FLC director. Solution to these equations describes the director grating arising in the FLC cell under photorefractive electric field $\mathbf{E}$ penetrating into the cell and interacting with the ferroelectric polarization $\mathbf{P}$. The director grating influences the energy exchange between two light beams propagating through the FLC cell. In order to study this we calculate the FLC dielectric tensor and use it at solving of the wave equation for electric field of the light beams. For solving of the wave equation, we follow a procedure first outlined by Kogelnik [5] and also used in our previous paper [1]. As a result, one can obtain amplitudes of the electromagnetic waves at the output of the FLC cell and calculate the exponential gain coefficient of the signal beam defined as $g = (1/L)\left|A_{out}/A_{in}\right|^2$, where $A_{in}, A_{out}$ are amplitudes of the signal beam at the input and output of the FLC cell, respectively, $L$ is the FLC cell thickness.

In particular, if a vector of the FLC polarization is parallel to the director, $\mathbf{P}=P_0\mathbf{n}$, and anchoring of the director with the cell substrates is infinitely rigid, the expression for the gain coefficient in the one constant approximation ($K_{11}=K_{22}=K_{33}=K$) is as follows:

$$g \approx 2.5\frac{\pi}{\lambda_0}\frac{\left(n_e^2-n_o^2\right)\left|E_{0sc}(q)\right|}{L}\frac{1}{\left(\tilde{q}+q\right)}\frac{P_0}{q^2K}\left(\theta_1-\theta_2\right), \quad \tilde{q}=q\sqrt{\tilde{\varepsilon}_{\parallel}/\tilde{\varepsilon}_{\perp}}, \quad q=2\pi/\Lambda,$$

where $\lambda_0$ is the wavelength of the incident light, $\Lambda$ is the director grating spacing, $E_{0sc}(q)$ is the space charge field, $\theta_1, \theta_2$ are the angles of the director pretilt at the cell substrates, $n_e, n_o, \tilde{\varepsilon}_{\parallel}, \tilde{\varepsilon}_{\perp}$ are the LC refractive indices and the LC static permittivity components parallel and perpendicular to the director, respectively.

Comparing the obtained result with the gain coefficient $g_{flex}$ calculated in LC with a flexoelectric modulation mechanism of the director [1], we arrive at

$$\frac{g}{g_{flex}} \approx \frac{2P_0}{q\left(e_{11}+e_{33}\right)},$$

where $e_{11}, e_{33}$ are the flexoelectric coefficients.

Using typical values of the grating spacing $\Lambda=(1-5)\,\mu m$, $e_{11}+e_{33}\approx 10^{-11}C/m$, the LC elastic constant $K\sim 10^{-11}N$ [1], $P_0\approx 1\mu C/cm^2$ [6] we get the estimate $g/g_{flex}\geq 10^2$. Thus, the gain coefficient in a FLC based hybrid system can be more than two orders of magnitude greater compared to the gain coefficient in a system with a conventional LC.

The dependence of the gain coefficient $g$ on the LC parameters was studied for different values of the grating spacing and direction of the FLC polarization, as well as the influence on $g$ of the director anchoring strength $W$ with the cell substrates and the photorefractive field inhomogeneous distribution over the LC cell thickness.

**References**

[1] V. Yu. Reshetnyak, I. P. Pinkevych, G. Cook et al. Phys. Rev. 81, 031705 (2010).
[2] O. D. Lavrentovich. PNAS, 117 (26) 14629 (2020).
[3] J. Ortega, C. L. Folcia, J. Etxebarria et al. Liq. Cryst. 49, 2128 (2022).
[4] N. Sebastián, M. Lovšin, B. Berteloot et al. Nat. Commun. 14, 3029 (2023).
[5] H. Kogelnik, Bell Syst. Tech. J. 48, 2909 (1969).
[6] H. Nishikawa, K. Sano, S. Kurihara et al. Commun Mater 3, 89 (2022).

# Applications of light-driven nanomotors and deflecting metagratings in sensing and microscopy

**Hana Jungová**[a]

[a] Chalmers University of Technology, Göteborg, Sweden,
hana.jungova@chalmers.se

The last decade has seen remarkable advancements in the development of nanomotion detectors as noninvasive monitoring devices of cellular life and health. However, hundreds or thousands of cells are often needed for the analysis and it is not possible to distinguish various nanomotion patterns due to insufficient spatial resolution of the current techniques. In our research we use a gold nanorod (rotary nanomotor) spinning at kHz frequencies [1] that is trapped in optical tweezers to detect nanomotions of single cells. We show that the light-powered nanomotors can be detections of nanomotions of single mammalian cells with an unprecedented spatial resolution [2]. This new technique can provide insights into fundamental cellular processes, potentially leading to the development of new diagnostic tools.

In the second part of my talk, I will discuss our recent research on flat metaoptics, components aimed at replacing classical optical elements, potentially leading to highly compact biophotonics devices. We demonstrate curved GaAs metagratings integrated on vertical-cavity surface-emitting lasers (VCSELs) that enable on-chip illumination for total internal reflection and dark field microscopy, with rapid switching between the two illumination modes [3]. Our approach provides a versatile illumination solution for high-contrast imaging, compatible with conventional microscopy setups and integrable with biophotonics devices such as portable microscopy and lab-on-a-chip devices.

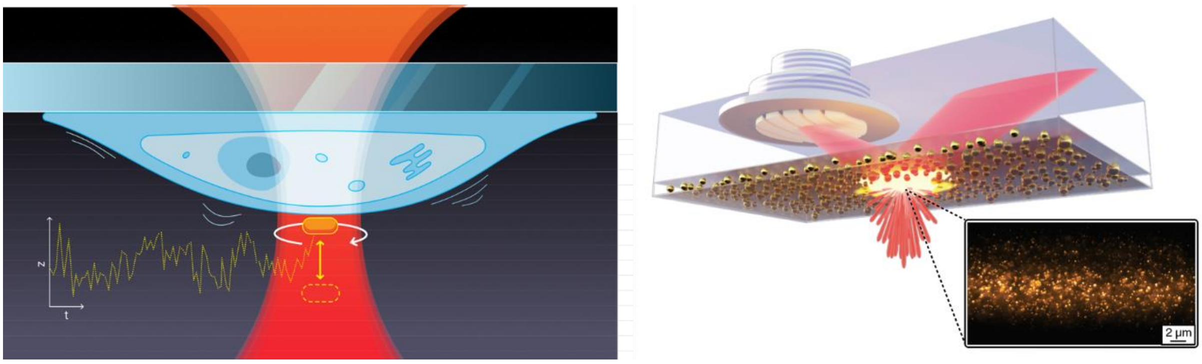

*Figure: Detection of cellular nanomotion with a gold-rotary nanomotor (left). Miniaturized illumination module for high-contrast microscopy (right).*

## References

[1] Shao, et. Al; Gold nanorod rotary motors driven by resonant light scattering. *ACS Nano* (2015), 9 (12), 12542-12551.

[2] Thornéus, E. et.al. Detecting nanomotions of single endothelial cells using rotary nanomotors. *In preparation* (2024)

[3] Mindaugas Juodėnas, et al.; High-angle deflection of metagrating-integrated laser emission for high-contrast microscopy *Light Science and Applications* 12 (2023) 251

# Magnetic control of electrically uncharged magneto-optical particles

**M. I. Marqués**[a]*, S. Edelstein[b], P.A.Serena [b], B. Castillo López de Larrinzar [c]and A. García-Martín[c].

[a] Departamento de Física de Materiales, IFIMAC and Instituto de Física de Materiales
Nicolás Cabrera" Universidad Autónoma de Madrid, 28049 Madrid, Spain
[b] Instituto de Ciencia de Materiales de Madrid (ICMM-CSIC), Campus de Cantoblanco, 28049 Madrid, Spain
[c] Instituto de Micro y Nanotecnología IMN-CNM, CSIC,CEI UAM+CSIC, Isaac Newton 8, Tres Cantos, 28760 Madrid, Spain

*manuel.marques@uam.es

Constant magnetic fields are known to interact with electrically charged particles inducing Lorentz forces that point in a direction perpendicular to the field. However, if the particle is electrically discharged, it is impossible to induce a force using a constant magnetic field. An exotic option is to mimic a magnetic charge on a neutral particle. This false magnetic monopole will interact with the magnetic field just as an electric charge would do with an electric field through the Coulomb interaction. Attempts to generate this magnetic charge have mainly relied on quasiparticles generated using condensed matter spin ice networks [1-3]. In this work we present another option based on neutral magneto-optical particles illuminated by a spinning monochromatic light field [4]. We will analyze the behavior of these particles under different fluctuating isotropic optical configurations [5,6], and we will calculate the value of the induced magnetic charge. We will prove that this is a purely non-reciprocal effect as the reciprocal equivalent (a chiral dipole) despite presenting a dichroic response, does not experience any force when illuminated by the spinning field. The magnetic charge induced by impinging radiation on the magneto-optical dipole is found to depend linearly on the helicity of the field. In addition, this artificial monopole experiences a dichroic permanent optical torque and does not interact with an external electric field.

## References

1. S. T. Bramwell, S. R. Giblin, S. Calder, R. Aldus, D. Prabhakaran, and T. Fennell, Measurement of the charge and current of magnetic monopoles in spin ice, Nature 461, 956 (2009).
2. S. J. Blundell, Monopoles, magnetricity, and the stray field from spin ice, Phys. Rev. Lett. 108, 147601 (2012).
3. C. Castelnovo, R. Moessner, and S. L. Sondhi, Magnetic monopoles in spin ice, Nature 451, 42 (2008).
4. S. Edelstein, R. M. Abraham-Ekeroth, P. A. Serena, J. J.Saenz, A. Garcia-Martin, and M. I. Marques, Magnetooptical stern-gerlach forces and nonreciprocal torques on small particles, Phys. Rev. Res. 1, 013005 (2019).
5. J. Luis-Hita, M. I. Marques, R. Delgado-Buscalioni, N. de Sousa, L. S. Froufe-Perez, F. Scheold, and J. J.Saenz, Light induced inverse-square law interactions between nanoparticles: “mock gravity" at the nanoscale, Phys. Rev. Lett. 123, 143201 (2019).
6. J. Luis-Hita, J. J. Saenz, and M. I. Marques, Active motion induced by random electromagnetic fields, ACS Photonics 9, 1008 (2022).

# Rare-earth doped $YVO_4$ crystals beyond lasing: applications in thermometry and optofluidics

**V. H. Paschoal**[a,*], P. Karpiński[a]

[a]Institute of Advanced Materials-Wroclaw University of Science and Technology

*vitor.paschoal@pwr.edu.pl

Yttrium vanadate ($YVO_4$) is one of the most popular materials used in optics, often used as a host material for lasers based on emission from rare earth (RE) ions, like Neodymium (Nd) or Ytterbium (Yb).[1] It is observed in a zircon-type structure and shows significant birefringence of around $\Delta n=0.2$.[1] In this work we explore un-doped and RE-doped $YVO_4$ microcrystals as a candidates for optical cooling, optical tweezers, and Raman and luminescence thermometry. We synthesize microcrystals using a novel micro-wave-assisted mineralization route, obtaining few micrometer-sized polyhedral crystals. Due to high refractive index of $YVO_4$ microcrystals they can be easily optically trapped. Additionally, high birefringence allows to induce strong angular momentum on them by circularly polarized light. The angular momentum acting on them cause their spinning with average frequencies of ~100 Hz (at ~100 mW), which are comparable to spinning frequencies observed for nano-waterite.[2] In Figure 1, we show the Raman spectrum for un-doped crystals at 373 K. We can use frequency shift of the Raman modes as a temperature indicator. In the inset we show linear softening of marked $A_{1g}$ mode with increasing temperature ($T$) of the sample in the range from 275 to 375 K.

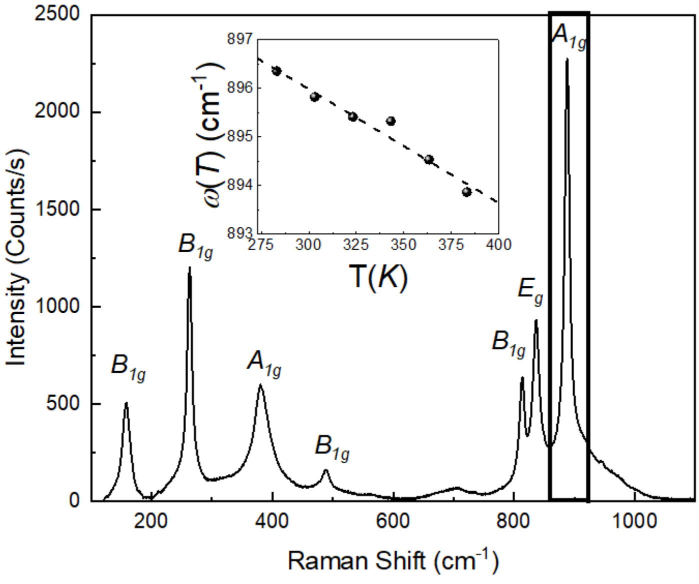

Figure 1: The Raman spectra of $YVO_4$ microcrystals taken at 373 K, with the mode symmetries marked. Inset: Frequency of the highlighted $A_{1g}$ mode versus Temperature, $T$.

## References

[1] A. Sanson *et al.* Physical Review B. 86, 214305 (2012)

[2] Y. Arita *et al.* ACS Nano 10(12), 11505 (2016)

# Optofluidic platform for the manipulation of water droplets on engineered Fe:LiNbO₃ surfaces

**Sebastian Cremaschini** [a], Annamaria Zaltron, Davide Ferraro, Alberto Cattelan, Alessio Meggiolaro, Filippo Marinello, Daniele Filippi, Matteo Pierno, Cinzia Sada, Paolo Umari and Giampaolo Mistura

[a] Department of Physics and Astronomy Galileo Galilei, University of Padova, via Marzolo 8, 35131 Padova, Italy.

* sebastian.cremaschini@studenti.unipd.it

The actuation of liquid droplets on a surface has relevance in many industrial fields and in microfluidics. In recent years, various strategies have been exploited to accomplish the task: in this work we present an optofluidic platform, which allows reproducing the basic droplet handling operations obtained in a common closed microfluidic device [1]. This platform is based on a z-cut iron-doped lithium niobate crystal (Fe:$LiNbO_3$): when illuminated with light, surface charges of opposite signs are generated at the two faces of the material due to the photovoltaic effect [2]. These charge accumulations create virtual reconfigurable electrodes, that can be exploited to manipulate microliter water droplets (which correspond to millimeters in size) and overcome the typical drawbacks of electrowetting based techniques. The crystal face in contact with the droplets is coated with a lubricant-infused layer (LIS), which guarantees hydrophobicity and produces a very slippery and robust surface for prolonged use [3].

In particular we performed measurements in two different configurations: in the first case the Fe:$LiNbO_3$ sample is tilted of a specific angle and light patterns with shapes of straight or curved lines are projected by a spatial-light-modulator (SLM) to illuminated a specific area of the sample (passive case). The droplets start sliding on the sample till they reach the illuminated area, where they are able to deviate and follow the entire illumination pattern from the beginning till its end (see Fig.1 (a)-(d)).

In the second type of configuration the sample is maintained horizontal and the illumination pattern is constituted by a single light spot with uniform intensity (active case); here different patterns (linear and curvilinear) are created by simply moving the light spot, illuminating different regions of the $LiNbO_3$ sample at different time instants. In this way, we were able to actuate, merge and even split microliter water droplets by simply exploiting the dielectrophoretic force generated by photovoltaic effect of $LiNbO_3$ (see Fig.1 (e)-(h)).

The actuated droplets can cover distances of some centimeters in a few seconds. This optofluidic platform is highly flexible, reconfigurable and does not require moving parts.

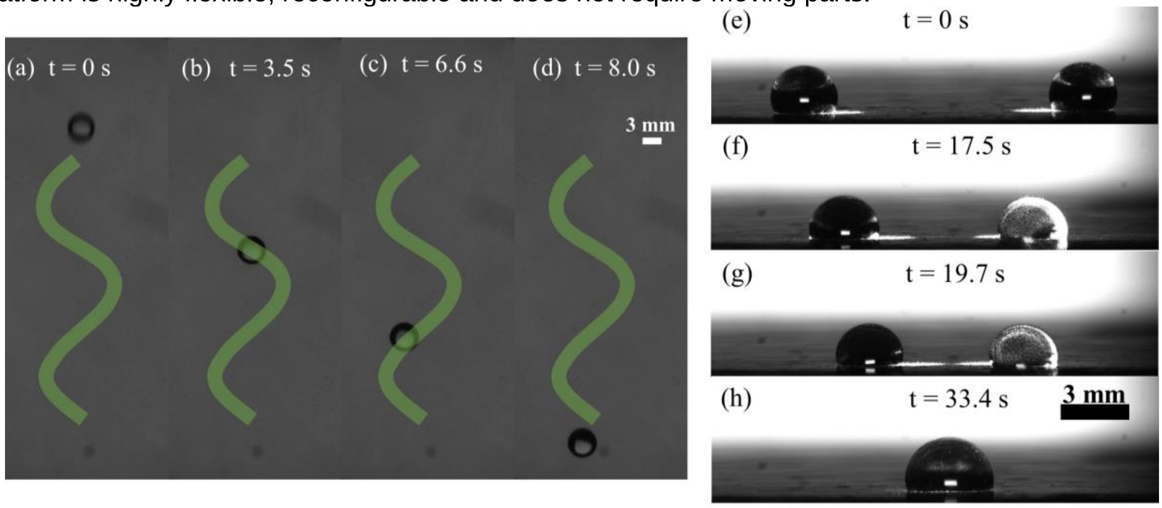

*Figure 1 – (a)-(d) Sequential video frames showing the motion of a droplet along an illuminated wavy pattern. (e)-(h) Sequential video frames showing the merging of two droplets, moving along two counterpropagating directions.*

In particular, next the splitting phenomenon has been studied in detail due to its implications in chemistry and biological fields: when the illumination intensity is enough, millimetric water droplets placed near the illuminated area of the sample split into two fragments: one fragment remains trapped in the illuminated region, while the other one moves away from it. Notably, this second fragment does not move randomly, but it follows three well-defined trajectories separated by 120°, reflecting the anisotropy in the crystalline structure of: Fe:LiNbO$_3$ [4] (see Fig. 2 (a)).

Moreover, we discovered that the presence of the lubricant layer (LIS) is crucial to observe the splitting of water droplets and the thickness of this liquid layer affects the reproducibility of the phenomenon.

Numerical simulations to explain the splitting event have been performed to explain the splitting of water droplets: we discovered that an interplay between photovoltaic, piezoelectric and pyroelectric effects allows to explain in details the physics behind the observed phenomenon (see Fig. 2 (b)).

In particular, the electric field profile related to photovoltaic effect is characterized by a circular symmetry and allows to explain the occurrence of the splitting of water droplets, since it is possible to reach electric field values comparable with the ones found in literature and typical of splitting exploiting electrowetting technique. While the electric field profile related to the pyroelectric effect, generated due to the fact laser illumination induces a heating of Fe:LiNbO$_3$ sample, is characterized by three main lobes and allows to explain the peculiar trifurcated motion of the second water fragment split from the mother droplet.

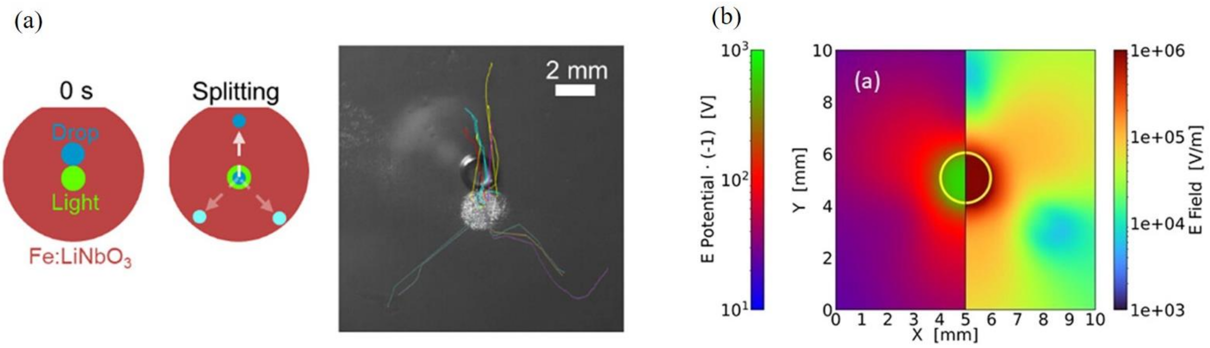

*Figure 2 – (a) Scheme of droplet splitting on Fe:LiNbO$_3$; the three directions of motion of split fragment separated by 120° each are highlighted. (b) Magnitude of the electric field (right half) and the electric potential changed of sign (left half) calculated on the upper surface of a z-cut Fe:LiNbO$_3$ crystal. These graphs combine both the photovoltaic and the pyroelectric effects induced in the sample due to laser illumination. The yellow circle indicates the contour of the illumination pattern.*

## References

[1] A. Zaltron et al., Advanced Materials Interfaces, 9, 2200345 (2022).

[2] A. Puerto et al., Physical Review Appli, 14, 024046 (2020).

[3] T.-S. Wong et al., Nature, 477, 443-447 (2011).

[4] S.Cremaschini et al., ACS Applied Materials Interfaces, 16, 4271-4282 (2024).

# Photovoltaic opto-electrowetting using Fe:LiNbO$_3$ on artificially micropatterned surfaces

**R. Zamboni**[a*], D. Ray[b], J. Imbrock[a].

[a] Institute of Applied Physics, University of Münster, Corrensstr. 2/4, 48149 Münster, Germany
[b] Indian Institute of Technology (IIT) Kanpur

* riccardo.zamboni@uni-muenster.de

## Introduction

Electrowetting is a technique that is widely used to control the wettability of different substrates [1]. A significant advancement in electrowetting was represented by the introduction of virtual electrodes generated by light [2], which consist of photoexcited space charge distributions. The shape and position of these virtual electrodes are defined by light through optical shaping and reconfiguration of the light beam. These unique features have led to the development of numerous opto-electrowetting methods. Among the techniques and substrates used to transduce light stimulus into electric fields, the bulk photovoltaic effect exhibited by ferroelectric crystals has shown remarkable performance due to moderate light intensities ($<10^4$ W m$^{-2}$) to achieve strong electric fields (~kV mm$^{-1}$) [3], particularly iron-doped lithium niobate (Fe:LiNbO$_3$) has been proven outstanding materials [3]. However, despite the success of this technique, crystalline materials can hardly be sculpted and customization of the wetting properties requires coatings and treatments, which are not always easy to achieve in the crystal [4]. Furthermore, the necessity for rapid prototyping protocols requires a disposable and inexpensive substrate to host custom wetting properties. Complex wetting states and properties can be obtained, for instance, by varying the roughness of the substrates [5]. The tailoring of the morphological micro- and nanostructures of the substrates has led to significant advances in practical applications [5]. In particular, the textured substrate of pillars exhibits either the Cassie-Baxter state (see Figure 1a), in which a fakir-like droplet is suspended on top of the pillars with air pockets underneath, or the Wenzel state (see Figure 1b), in which the droplet wets completely the surfaces and liquid is trapped in the structures. These two wetting states are exploited by different plants to repel or trap water [6]. The development of artificially micropatterned surfaces inspired by nature has led to significant advantages in wetting applications [5], particularly in platforms that can achieve a transition between these two states.

In this contribution, we present a method for controlling wetting on artificially micropatterned surfaces using the photovoltaic electric field on Fe:LiNbO$_3$ (see Figure 1c). The Cassie-Baxter to Wenzel states transition is achieved by long-range interaction between photovoltaic virtual electrodes on the Fe:LiNbO$_3$ and a 3 µL droplet suspended on micropatterned substrates.

## Experiments and Results

The micropatterned substrates consist of a 0.5 mm thick quartz substrate textured with SU8 cylindrical pillars made with lithographic technique. After a silanization treatment, this substrate exhibits a superhydrophobic Cassie-Baxter wetting state. The crystal is a 0.1%mol iron-doped crystal lying below in contact with the substrate without any adhesion techniques.

Sessile droplets on the substrate in the initial Cassie-Baxter states (see Figure 1d) exhibit a transition to Wenzel states upon the photoinduction of virtual electrodes on the crystal (see Figure 1e). This transition is proven by numerical and experimental results to be caused by the Maxwell stress induced by the evanescent photovoltaic field acting against the capillary pressure that maintains the droplets suspended on the microstructures. The contact angle is monitored during the photoinduction of the virtual electrode with a homogeneous intensity $I \leq 2.2 \cdot 10^3$ W m$^{-2}$ (see Figure 1f). The temporal evolution of the droplet and the Maxwell stress is consistent with the charge accumulation in the virtual electrode described by the one-center model. Both light intensity and iron doping have been modified to show the variation in the speed of charge accumulation and speed of the transition. In addition, different shapes of the electrodes have been employed and the rectangular virtual electrodes are proven as the most efficient for a wetting transition in a few seconds.

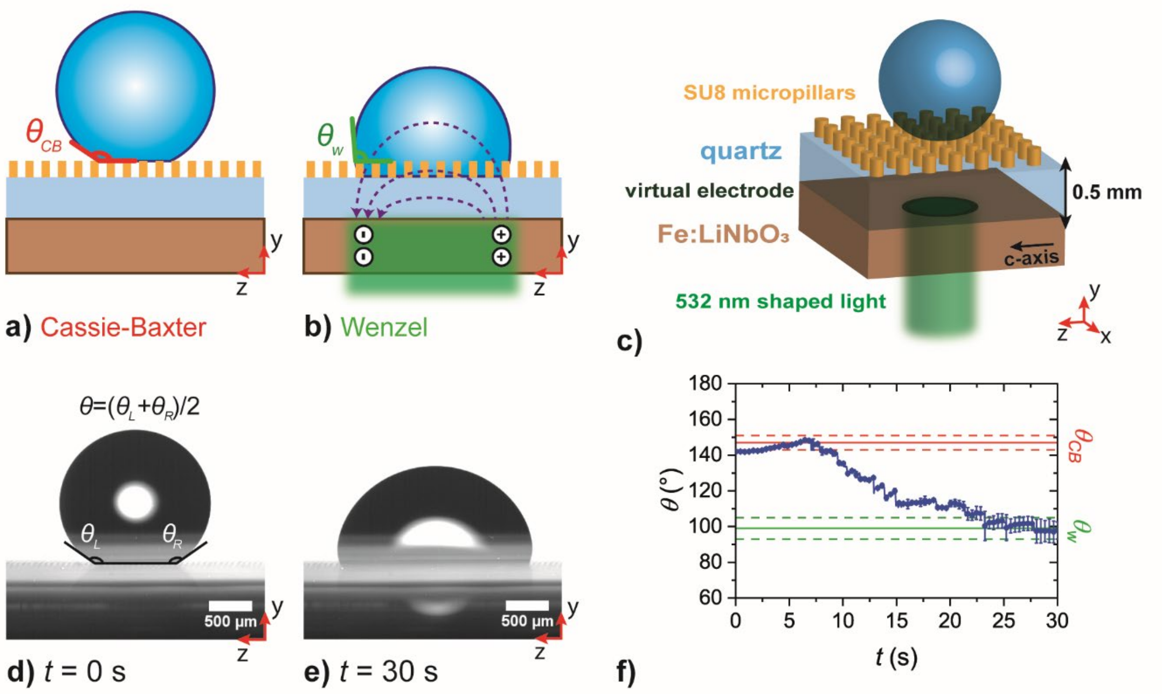

**Figure 1.** Cassie-Baxter to Wenzel state wetting transition achieved with virtual electrodes on the Fe:$LiNbO_3$. a) b) Schematics showing the Cassie-Baxter and the Wenzel state, respectively. In b) the working mechanism of the interaction with the virtual electrodes is illustrated with the dashed purple line showing the evanescent electric field. c) 3D illustration of the complete system. d) Image of a 3 µL droplet in the initial Cassie-Baxter state. The contact angle is measured as the average of the left and right contact angle. e) Image of the same droplet in e) after 30s of the illumination of Fe:$LiNbO_3$. In this case, the droplet shows a Wenzel state. f) Evolution of the measured contact angle θ. The green and red lines, $\theta_{CB}$ and $\theta_W$ represent the measured contact angle from the morphology of the substrate for the Cassie-Baxter and Wenzel states, respectively. Both d) and e) are examples of images used for the graph f).

## Conclusion

In this contribution, we demonstrate a method for inducing wetting of the Cassie-Baxter to Wenzel transition in Fe:$LiNbO_3$ using long-range photovoltaic virtual electrodes. This method does not rely on any specific substrate characteristics, allowing for substrate disposal and replacement as needed for different applications. Furthermore, the transition is achieved without the need for an adhesion process between the crystal and the substrate, enabling a rapid exchange of the latter.

Acknowledgments: This work has been funded by the Deutsche Forschungsgemeinschaft (DFG, German Research Foundation) – 5126330344.

## References

[1] Nelson, W. C., Kim, C. J. C. *Journal of Adhesion Science and Technology*, 26(12-17), 1747-1771 (2012).

[2] Thio, S. K., Park, S. Y. *Lab on a Chip,* 22, 3987-4006 (2022).

[3] Fan, B., et al. *Physical Review Applied,* 7(6), 064010 (2017).

[4] Zaltron, A., et al. *Advanced Materials Interfaces*, 9(22), 2200345 (2022).

[5] Zeng, Q., et al. *Nanoscale*, 13(27), 11734-11764 (2021).

[6] Guo, Z., Weimin, L., Bao-Lian S. *Journal of colloid and interface science* 353(2), 335-355 (2011).

# Surfing on the edge of exploring new perspectives: light-driven phenomena as a booster for new applications and scientific progress

**C. Sada**[a,*],

[a]Physics and Astronomy Department, University of Padova Via Marzolo 8, 35121 Padova (Italy)

*Keynote: cinzia.sada@ unipd.it

From the very beginning, fundamental research on light-driven phenomena in materials has triggered interdisciplinary applications. Optical sensing and storage, as well as optical nonlinear effects, have dominated scientific research for a long time, showing relative advantages and disadvantages. It was not expected that what was then seen as a possible limitation would turn out to be such a great potential. In fact, the effect of generating electric fields through light-matter interactions, including their modulation and shaping, has allowed the field to be broadened to include, for example, the manipulation of optical particles, both inorganic and organic, even living ones. Advanced photonics applications have just been proposed for green sustainability, supported by research into new materials, both in hybrid configurations and in integrated platforms. Surfing on the edge of exploring new perspectives, this talk will present some ideas recently proposed by the scientific community to think out of the box and use light-driven phenomena as a booster for new applications and scientific progress.

# Droplet manipulation on superhydrophobic surfaces enabled by electrostatic charge printing using Fe:LiNbO$_3$

**A. Sadasivan**[a*], C. Sebastián-Vicente[b], A. García-Cabañes[b], M. Carrascosa[b],
J. Imbrock[a], R. Zamboni[a].

[a] Institute of Applied Physics, University of Muenster, Corrensstr. 2/4, 48149 Muenster, Germany
[b] Department of Materials Physics and Instituto Nicolás Cabrera, Autonomous University of Madrid, c/ Francisco Tomás y Valiente 7, Madrid, 28049 Spain

* asadasiv@uni-muenster.de

## Introduction

Superhydrophobic surfaces are employed by nature due to their unique wetting properties for controlling liquid-solid interface. Mimicking this structure, many technologies have been developed in various applications, from self-cleaning materials to biomaterials for their low friction [1]. Droplet manipulation on these materials is, therefore, an essential operation in many applications, such as microfluidic devices, medical diagnosis, lab-on-chip, etc [1]. Droplet transport is typically triggered by external stimuli, among which the electric field represents the most efficient one [2,3]. In this context, the conventional approach involves electrode patterning and an external voltage. The lack of reconfigurability of conventional approaches is overcome by the use of virtual electrodes shaped by light [3], consisting of space charge patterns induced by optical stimulus. This requires the introduction of active materials able to generate electric fields in response to light in a controlled way [3]. Among other materials, Fe:LiNbO$_3$ has been proven to be an optimal substrate for inducing strong and localized electric fields via its photovoltaic effect using light stimulus [4]. The advantage of this technique is the ability to shape virtual electrodes on the Fe:LiNbO$_3$ crystal, induced by structured light for droplet manipulation [5]. However, this method is hindered by the crystalline nature of this material, which is hard to sculpt and bend due to its lack of flexibility. In addition, this material does not provide the flexibility of conventional material used in lab-on-a-chip devices, which can be replaced upon applications. Fe:LiNbO$_3$ cannot be customized in its mechanical and chemical properties, for example, is inherently hydrophilic (unless functionalized with a hydrophobic coating), thus hindering the range of application.

Hence, we take advantage of a novel method to transfer the virtual electrodes on Fe:LiNbO$_3$ to passive dielectric substrates. The method has been demonstrated to transfer charges to neutral dielectric particles in contact with the illuminated region of Fe:LiNbO$_3$ [6] , as well as to print virtual charges onto the passive substrates [7]. Upon contact between the Fe:LiNbO$_3$ crystal and passive dielectric substrate, a mirror replica of the charge pattern on Fe:LiNbO$_3$ is formed on the dielectric substrate (see Figure 1a). After the removal of Fe:LiNbO$_3$, the passive substrates are used for droplet manipulation taking advantage of the printed charges. In this work, a 100 μm thin layer of polyethylene terephthalate (PET) has been used as a passive substrate coated with different superhydrophobic coatings, namely Teflon (PTFE) and Tegotop (Evonik) spray (see Figure 1b). Printed charges in an area of 10x5 mm$^2$ have been employed for electrowetting, showing an average variation of contact angle of 95±7° and 118±5° for water droplets on PET coated with PTFE spray and Tegotop, respectively.

To further study the performance of printed virtual electrodes, we observed the transport of water droplets on these films at different inclinations under the influence of printed charges. A Gaussian beam was employed to induce charges on Fe:LiNbO$_3$, to imprint a similar charge pattern on the dielectric substrate. This led to a repulsive and attractive behavior of droplets as they come in contact with the printed virtual electrode (see Figure 1c). The dielectrophoretic attraction and electrophoretic repulsion scales with the amount of charge printed. According to the one-center model, this is observed with different light intensities and exposure times. Delving into inclined substrates, we have detected a droplet that shows droplet splitting in correspondence with the charged pattern. The droplet initially slides on the substrates and, in correspondence with the charged pattern leaves behind a daughter droplet due to the attraction of the charge pattern (see Figure 1c). This demonstrates that aqueous droplets can be influenced by dielectrophoresis or electrophoresis due to the electric field generated by printed charges. Structured light has been used to print striped patterns to control the trajectory of the droplet.

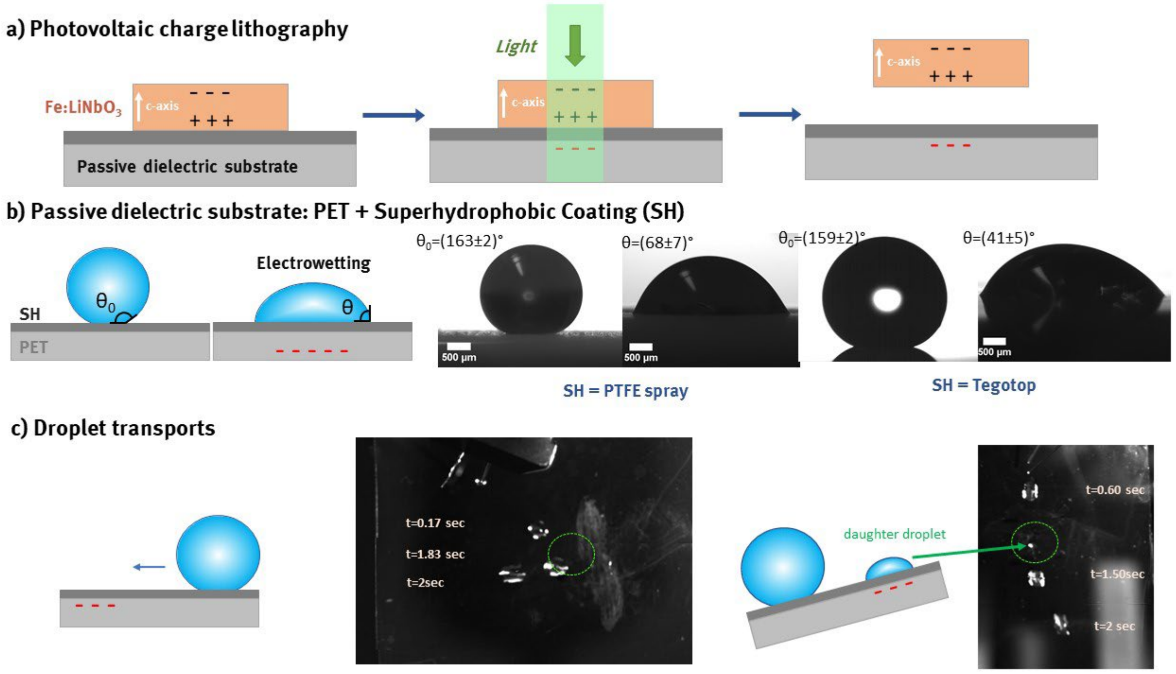

Figure 1. a) **Photovoltaic charge lithography**: Three-step process of charge printing on a passive dielectric substrate (in gray, the darker color represents the coating) using a virtual electrode on z-cut Fe:LiNbO$_3$. b) **Electrowetting**: Variation in contact angle of PET coated with superhydrophobic layer (PTFE spray and Tegotop) without and with charge printing. c) **Droplet transport**: Trajectory of a 5µL droplet on PET coated with Tegotop. On the left, the droplet is initially attracted towards the Gaussian spot, where charges are printed (highlighted by the dashed green circle), followed by repulsion. On the right, the droplet slides on a substrate inclined at 15°, here we observed that the path of the droplet changed due to the localization of charges in PET, and part of the droplet remains trapped at the charged spot.

## Conclusion

We showed droplet manipulation using electrostatic charge printing on dielectric materials (PET) using the light-induced photovoltaic photoexcited pattern on Fe:LiNbO$_3$. This method enables the induction of electrostatic charge on passive dielectric substrates in a controlled manner. We showed that droplet transport, splitting, and electrowetting can be achieved with this method on disposable and conventional passive substrates, opening new opportunities for applications in biomedical fields.

**Acknowledgments**: This work has been funded by the Deutsche Forschungsgemeinschaft (DFG, German Research Foundation) - 5126330344.

## References

[1] Yong, Haiyang, et al. *Advanced Materials Interfaces* 9.30, 2200435 (2022).

[2] Yang, C., et al. *Advances in Colloid and Interface Science*, 306, 102724 (2022).

[3] Cheng, Guangyao, et al. *Advanced Materials*, 2313935 (2024).

[4] Puerto, A., Méndez, A., Arizmendi, L., García-Cabañes, A., Carrascosa, M. *Physical Review Applied*, 14(2), 024046 (2020).

[5] Zaltron, A., et al. *Advanced Materials Interfaces*, 9(22), 2200345 (2022).

[6] Sebastián-Vicente, et al. *IEEE International Symposium on Applications of Ferroelectrics (ISAF)*. IEEE, 2022.

[7] Sebastián-Vicente, Carlos, et al. *Advanced Electronic Materials* 8.2, 2100761 (2022).

# Integrated optofluidics on lithium niobate: effects of photo-induced electric fields on water droplets with dispersed micro-objects

**G. Bragato**[a,*], A. Zaltron[a], R. Zamboni[b], M. De Ros[a], C. Sada[a]

[a]Physics and Astronomy Department, University of Padova Via Marzolo 8, 35121 Padova (Italy)

[b] Institute of Applied Physics, University of Münster, Corrensstr.2/4, 48149 Münster (Germany)

*presenting author: giovanni.bragato@phd.unipd.it

Recently, the development of new opto-microfluidic sensing devices in $LiNbO_3$ has gained increasing interest due to the promising features allowed by the combination of microfluidic and optical stages on the same platform, that addresses the need for integrating in the same portable device several tools which carry out different tasks, e.g. manipulation of droplets, optical sensing, targets identification and sorting [1]. In particular, the possibility of exploiting external electric fields to move droplets, sort and merge them as well as modify their shape has been explored in the last years [3]. The actuation and control of liquid droplets represent in fact a major challenge not only for many industrial processes but also for chemical, biological and medical applications. Active control of droplets by means of electric fields is typically achieved by metallic electrodes that cannot be reconfigured. An interesting alternative to bypass this constraint is provided by the so-called virtual electrodes, i.e. electrodes generated by light-induced phenomena able to locally modify the conductivity of the substrate. In this work a new concept of droplet-based opto-microfluidic platform integrated in lithium niobate is presented that combines microfluidics with integrated optics and virtual electrodes made by photovoltaic phenomena to enable either the modification or the actuation of dispersed objects within water droplets. Since the droplets lengths was proven to be sensitive to the photo-induced electric field with a dependence on the droplets' velocity [1] and on the dissolved electrolytes concentration, interesting novel perspectives will be discussed in the field of optical sensing.

## References

[1] Zamboni R., Zaltron A., Chauvet M., Sada C., Sci. Rep. Vol 11 pag 1 (2021)

[2] Bragato G, Zaltron A., Zanardi M., Zamboni R., De Ros M., Sada C., Adv. Mater. Interfaces, 2301008 (2024)

[3] Zaltron A., Ferraro D., Meggiolaro A. Cremaschini S., Carneri M., Chiarello E., Sartori P., Pierno M., Sada C., Mistura G. Adv. Mater. Interfaces Vol 9 pag 2200345 (2022)

# Exploring the electric charge of tumour spheroids through their manipulation on photovoltaic ferroelectric platforms

**E. Rincón** [1], P. Camarero [1,2], Á. Mendez[3], M. Quintanilla [1,2], P. Haro-González [1,2], M. Carrascosa [1,2] and Á. García Cabañes [1,2]

[1] *Departamento de Física de Materiales, Universidad Autónoma de Madrid, Madrid 28049, Spain*
[2] *Instituto Nicolás Cabrera, Universidad Autónoma de Madrid, Madrid 28049, Spain*
[3]*Departamento de Mecánica de Fluidos y Propulsión Aeroespacial, ETSIAE, Universidad Politécnica de Madrid, Madrid, Spain*

* esther.rincona@estudiante.uam.es

Electrical charge is a key factor in the behavior of biological systems, as it determines the interaction with external factors, such as surrounding molecules or surfaces [1]. For this reason, physical methods to manipulate and characterize biological systems are increasing every day. Recent studies suggest that cancer cells are negatively charged on their surfaces [2]. Thus, net charge could be used to diagnose tissues. These studies, still limited, are mainly applied to the study of single cells although 3D tissues may exhibit different behaviors. Over the past few decades, 3D cell culture has been developed to prepare multicellular spheroids. This 3D cultures have cellular metabolism and cell-cell interaction closer to those of tissues, thus are used as a middle point between *in vivo* and *ex vitro* biological assays [3].

Optoelectronic photovoltaic tweezers have recently emerged for the manipulation of micro- and nano-objects [4]. This technique is based on the bulk photovoltaic effect (PVE), taking advantage of the light induced electric fields generated in some ferroelectric crystas, being particularly strong in $LiNbO_3$:Fe (LN:Fe) [5]. Because of their non-centrosymmetric lattice, as the crystal is illuminated, carriers from donor impurities are excited along the crystal's polar axis (*c* axis), resulting in a photo-current density. This charge separation gives rise to a bulk photovoltaic (PV) electric field $\boldsymbol{E_{PV}}$ inside the ferroelectric crystal, which extends outside as an evanescent field. This evanescent field will interact with objects near the ferroelectric's surface [6]. If the objects are not charged, they will undergo dielectrophoretic (DEP) forces $\boldsymbol{F_{DEP}}$, and charged objects will undergo both DEP and electrophoretic (EP) $\boldsymbol{F_{EP}} = q\,\boldsymbol{E_{PV}}$ forces, $q$ being the object's charge.

Recently, a method to manipulate aqueous solution droplets have been developed [7]. In this method, the ferroelectric surface is submerged in a non-polar liquid. Above it, the micro-droplet moves inside the liquid, hanging from the liquid-air interface. Particularly, it has been applied to droplets containing homogenously dispersed bio-material, such as DNA and sperm [6]. The analysis of the droplet's migration kinetics allows for the determination of the electrical forces acting on the droplet and the characterization of some droplet's properties, such as the bio-content concentration [6].

In this work, we report the application of this method to the manipulation and characterization of droplets containing a single multicellular spheroid. This hybrid system is composed of a single multicellular spheroid suspended inside a cell culture medium droplet, as it can be seen in Figure 1(a). Two cell lines of human cancer have been used: MCF-7 (Michigan Cancer Foundation-7) and U-87 MG (Uppsala 87 malignant glioblastoma). The difference between both cells lines lies in their cell joining mechanism. MCF-7 cells form side-by-side junctions, and U-87 MG cells form elongated unions. Therefore, MCF-7 cells form more compact spheroids than U-87 MG cells.

Z-cut LN:Fe crystals have been used as photovoltaic ferroelectric substrates, in which negative/positive charge is accumulated in the +*c*/−*c* faces, respectively (see Figure 1(b)). The LN:Fe crystal is placed at the bottom of a cuvette and covered in paraffin oil, which is then placed at the optic setup. The droplet is pipetted and left hanging at the oil-air interphase a few millimeters over the crystal's surface.

As the LN:Fe crystal is illuminated with a laser beam ( $\lambda = 488\,\mathrm{nm}$ in the case of this work), the PV evanescent field induces electrical forces (DEP and/or EP forces) on the droplet. In general, the electrical force on the hybrid droplet $\boldsymbol{F_{ELhd}}$, as it's shown in Figure 1(b), is $\boldsymbol{F_{ELhd}} = \boldsymbol{F_{DEP}} + \boldsymbol{F_{EP}} = \boldsymbol{F_{DEP}} + \boldsymbol{F_{EPm}} + \boldsymbol{F_{EPs}}$, where $\boldsymbol{F_{EPm}}$ is the EP force acting on the cell culture medium and $\boldsymbol{F_{EPs}}$ the EP force acting on the spheroid. As a result, the droplet starts undergoing a horizontal rectilinear motion towards the light beam (stopping at the illuminated region) or away from it.

In the case of cell culture medium droplets, results show migration towards the light on the +*c* face (negatively charged) and repulsion from the light on the -*c* face (positively charged). These results indicate that the cell culture medium is positively charged. When the cell culture medium droplet contained a single spheroid, either from MCF-7 or U-87 MG cell lines, a change in the behavior was observed compared to the manipulation of cell culture medium droplets. This result points to a net negative charge in the spheroids.

Through experiments of deionized water and cell culture medium droplets, $\boldsymbol{F_{DEP}}$ and $\boldsymbol{F_{EPm}}$ have been measured. With those results, together with experiments on hybrid droplets, $\boldsymbol{F_{EPs}}$ has been obtained. Knowing $\boldsymbol{F_{EPs}}$ and the PV electric field, the spheroids' charge density has been estimated.

Finally, because of the potential biological interest of this technique, viability assays have been carried out with U-87 MG spheroids after manipulation. Results show the spheroids' viability is not compromised by neither the PV evanescent fields nor the illumination by the laser beam.

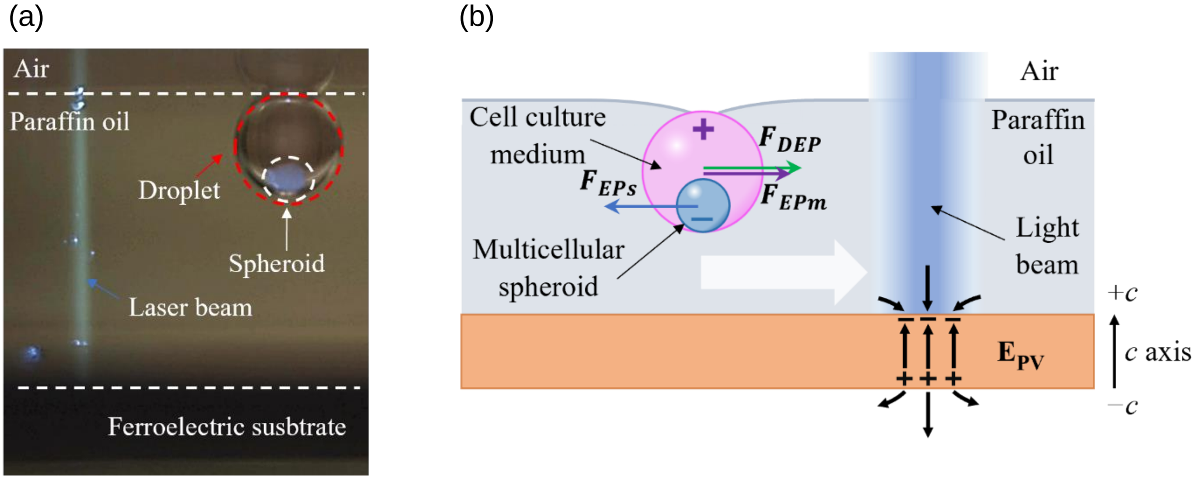

*Figure 1: (a) Schematics of the PV ferroelectric platform showing the hanging droplet containing the spheroid. The ferroelectric substrate is illuminated with a laser beam that generates a PV electric that manipulates the droplet. (b) Schematics of the electrical forces acting on a hybrid droplet manipulated on the +c face. The evanescent PV fields and charges in the LN:Fe crystal are also included.*

This work has been funded by MCIN/AEI/10.13039/501100011033 under the grants PID2020-116192RB-I00, PID2019-110632RB-I00, TED2021-129937B-I00, CNS2022-135495, and PID2023-151078OB-I00.

## References

[1] G. Caniglia et al., Anal Bioanal Chem **415** (11), 2059 (2023).
[2] L. Wenjun et al., Biophysics Reports **5** (1), 10 (2019).
[3] C. Jensen and Y. Teng, Front Mol Biosci **7**, 33 (2020).
[4] J. Meseguer et al., Eubacteria **34** (2015).
[5] B. Sturman and V. Fridkin, *The Photovoltaic and Photorefractive Effects in Noncentrosymmetric Materials*. Gordon&Breach Science Publishers (1992).
[6] A. Puerto et al., Biomed Opt Express **12** (10), 6601 (2021).
[7] A. Puerto et al., Physical Review Applied **14** (2), 024046 (2020).

# Pyro-electric and photorefractive effect for liquid manipulation and fabrication of 3D polymeric microneedles

**S. Coppola**[a], V. Vespini[a], L. Miccio[a], S. Grilli[a], P. Ferraro[a]
[a] CNR ISASI Institute of Applied Sciences and Intelligent Systems, via campi flegrei 34, 80078, Pozzuoli (NA), Italy

* sara.coppola@isasi.cnr.it

The development of innovative strategies for liquid dispensing and droplet motion control represents a key enabling technology for the fabrication of micro devices very common in our daily life. In the last decade, the interest in investigating and controlling liquids raised continuously, opening toward powerful potential applications both for industrial than academic point of view, mainly based on simple procedures and low cost methods. Point of care applications for a prompt on-site diagnosis and personalized treatment, clinical diagnostics, cell-based applications and detection or sensing are few examples of case of use. The biomedical application is not the only focus of the liquid dispensing, considering that synthetic polymers (“plastics”) are indispensable to society, and the market is expected to further expand in the medium-term future, a sustainable approach to the recycling of plastic wastes is a crucial and urgent requirement for transitioning from a linear to a (predominantly) circular model of economy. It is generally agreed that this calls for a complex strategy entailing (at least) the following four actions: the development on innovative technologies for: re-design the market of virgin plastic products, focusing on ‘mono-material’ solutions; enforce a separate collection of plastic wastes; sort any residual multi-material plastic wastes. In this condition the protocols for rapid determinations of waste composition by analysing the mold-free deformation patterns for electrostatically charged drops in intense electric fields will open a very interesting industrial scenario. Actually, manipulating polymers, dispensing and jetting liquid from a larger mother droplet or a liquid film using conventional methods require strong electric fields and very expensive equipment. In alternative, some years ago an innovative and efficient method was proposed for reaching high electric fields completely avoiding the use of external electrodes and very expensive nozzles [1,2]. The method prosed exploits the pyroelectric-EHD effect presented by lithium niobate (LN) when it undergoes to a temperature gradient. Different approaches have been experimented based on the pyro-EHD manipulation of liquids and polymers [3,4]. Recently, the use of iron doped lithium it has also been proposed for manipulating liquid in a contact-free modality through an external light source [5]. In fact, the iron doped LN presents photovoltaic in combination with slight pyroelectric effects. Here we report on the innovative methods proposed for liquid dispensing and for manipulating polymeric solutions. We propose the characterization of the process activated by various exciting sources and in case of different kind of liquids and polymers. We demonstrate that efficient drop blasting and liquid jetting can be easily achieved through visible laser light and by temperature gradient in different optical configurations [5-7]. The results have been characterized in terms of jetting periods, volume of the dispensed droplets and pattern geometry. The main components of the set-up are a Lithium Niobate crystal, that is used for the activation of the pyro-electrohydrodynamic or photorefractive effect, an external exciting source that could be in direct contact with the crystal or could work in non-contact modality, a receiving target connected to a moving stage in order to create patterns of different geometry and a liquid reservoir. The innovation of the method proposed is that we completely avoid the use of nano engineered nozzle, starting directly from the liquid drop that is deformed under the action of the pyro-electrohydrodynamic and photorefractive effect. In fact, because of the accumulation of external surface charges on the external layer of the liquid, the starting drop deforms assuming the shape of a Taylor cone [1]. Here we compare the dispensing and manipulating results obtained in different configurations and in case of different materials. We also describe how is it possible to characterize the materials in terms of deformation under the exciting source, focusing on different microstructures that could be fabricated using the proposed technology and that could find application in micro-fluidic, optics and biomedicine. In particular, we will focus on the fabrication and functionalization of chip and portable devices where polymeric microneedles will represent the smart components that could be used both for transdermal drug delivery and as biosensing components. We will also focus on the optical properties of the 3D microstructures proposed. We believe that functionalized microneedles with advanced light focusing properties will open to new minimally invasive treatments for nonmelanoma skin cancer very interesting for application of personalized medicine.

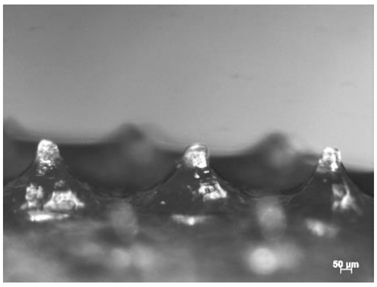

Polymeric microneedles.

**References**

[1] Ferraro, P., et al. "Dispensing nano–pico droplets and liquid patterning by pyroelectrodynamic shooting." Nature nanotechnology 5.6 (2010): 429-435.

[2] Coppola, Sara, et al. "Direct writing of microfluidic footpaths by pyro-EHD printing." *ACS Applied Materials & Interfaces* 9.19 (2017): 16488-16494.

[3] Bianco, Vittorio, et al. "Endowing a plain fluidic chip with micro-optics: a holographic microscope slide." *Light: Science & Applications* 6.9 (2017): e17055-e17055.

[4] Coppola, Sara, et al. "Transmitting light through biocompatible and biodegradable drug delivery micro needles." *IEEE Journal of Selected Topics in Quantum Electronics* 27.5 (2021): 1-8.

[5] Puerto, Andrés, et al. "Droplet Ejection and Liquid Jetting by Visible Laser Irradiation in Pyro-Photovoltaic Fe-Doped LiNbO3 Platforms." *Advanced Materials Interfaces* 8.22 (2021): 2101164.

[6] Coppola, Sara, et al. "Layered 3D printing by tethered pyro-electrospinning." *Advances in Polymer Technology* 2020 (2020).

[7] Coppola, Sara, et al. "Drop-on-Demand Pyro-Electrohydrodynamic Printing of Nematic Liquid Crystal Microlenses." *ACS Applied Materials & Interfaces* 16.15 (2024): 19453-19462.

# Design and fabrication of nanostructured diffractive microlenses inside optical crystals by 3D laser nanolithography

**F. Paz-Buclatin**[a], L. L. Martin[a,b] and A. Ródenas[a,b]

[a] Departamento de Física, Universidad de La Laguna (ULL), San Cristóbal de La Laguna, Tenerife, Spain
[b] Instituto Universitario de Estudios Avanzados en Física Atómica, Molecular y Fotónica (IUDEA), Universidad de La Laguna (ULL), San Cristóbal de La Laguna, Tenerife, Spain

* fpazbucl@ull.edu.es

## Introduction

The field of flat optics such as metalenses and diffractive lenses has been booming in the recent years, primarily because of their wavelength-thickness. A diffractive lens is composed of spatially arranged zones that impart an appropriate phase shift to the incident beam to produce a constructive interference at the focal point [1]. In this work, we fabricated a diffractive microlens embedded within the interior of an Yttrium Aluminium Garnet (YAG) crystal. The capability to fabricate the lens directly inside the crystal not only provides a protective layer to the lens surface, but also holds immense potential for photonic lab-on-a-chip applications. This is possible through the novel 3D femtosecond laser nanolithography technique [2,3].

## Methodology and Results

Our aim is to fabricate a 20 µm-diameter diffractive microlens with a numerical aperture (NA) of 0.49, designed to operate at $\lambda = 0.8$ µm, embedded 10 µm below the crystal's surface. For the design of the microlens, we use the hyperbolic phase function [4]: $\phi_{\mathrm{hyp}}(x, y) = (2\pi n_{bg}/\lambda_0)\left(f - \sqrt{x^2 + y^2 + f^2}\right)$, where $n_{bg}$ is the refractive index of the background medium, $\lambda_0$ is the design wavelength, f is the focal length, and x and y are the spatial coordinates of the microlens. To evaluate the focusing performance of the microlens, we carried out numerical simulations based on Finite-Difference Time-Domain (FDTD) algorithm. The simulated intensity distribution obtained by propagating a plane wave through the microlens is displayed in Fig. 1a. The focal spot is obtained at 20.6 µm from the diffractive microlens surface. The full width at half maximum (FWHM) of the spot is 0.82 µm and 5.4 µm in the transverse and axial direction, respectively. The focusing efficiency obtained, defined as the fraction of power within a circular region of radius 3 × FWHM in the focus plane to the total incident power [5], is 34.4% of the input power.

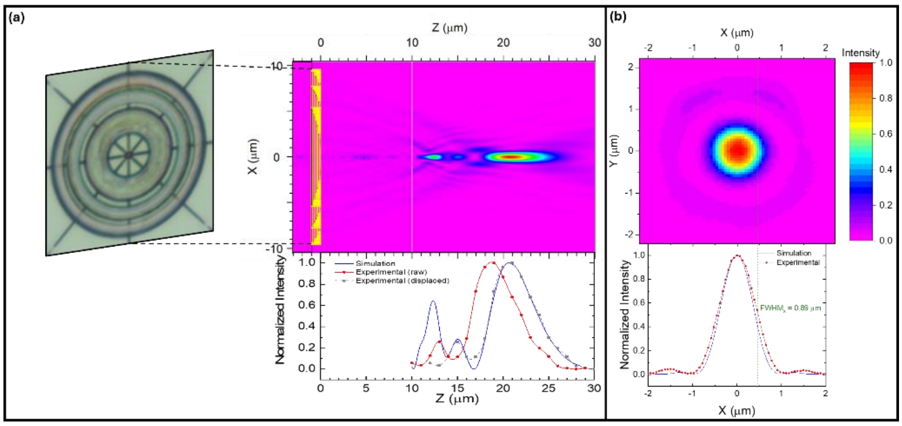

**Figure 1.** (a) Top: FDTD simulated axial intensity distribution of the diffractive microlens. Inset: Optical microscope image of the fabricated diffractive microlens. Bottom: Axial intensity profile of the experimental focal spot (red circles) superimposed on that of the simulated focal spot (blue solid line). Gray squares represent the displaced experimental data for ease of comparison. (b) Top: Transverse (xy) intensity distribution of the experimental focal spot at the focal length f=19.0 µm. Bottom: Transverse intensity profile of the experimental focal spot (red circles) superimposed on that of the simulated focal spot (blue solid line).

The diffractive microlens was fabricated using the 3D femtosecond laser nanolithography on a YAG crystal. This technique is a three-step process [3] which consists of (1) computer-controlled 3D direct laser writing of the design structure inside the crystal, (2) polishing of the top surface of the crystal to expose the nanotracks which will become the etching pores, and (3) chemical wet-etching of the crystal with phosphoric acid solution. The fabrication parameters such as the writing speed, laser pulse energy, and pulse repetition rate were carefully studied to replicate the microlens design with maximum precision. An optical microscope image of the fabricated diffractive microlens, embedded within the crystal, is shown in Fig. 1a (inset).

To evaluate experimentally the focusing performance of the fabricated microlens, the field profiles were measured using an 808 nm diode laser and a home-built microscope consisting of a 100x objective with NA 0.9, a 150 mm focal length tube lens, and a SWIR CMOS camera. The axial intensity profile of the focal spot plotted in Fig. 1a (red circles) is measured starting from the crystal's surface by translating the microscope along the optical axis (z) in steps of 1 µm. From this, the focal length is determined to be 19.0 µm. The axial FWHM is measured to be 5.5 µm, in agreement with the simulated $\mathrm{FWHM_z}$. To facilitate the comparison between the experimental axial intensity profile and the simulated one (blue solid line), the data points were displaced to equalize the focal lengths (black squares). It can be observed that the experimentally obtained profile closely matches the simulations. Fig. 1b shows the transverse cut of the experimental focal spot at 19.0 µm, showing a near diffraction-limited focal spot. The intensity distribution along the x-axis is shown below it, along with the simulated distribution for comparison. The $\mathrm{FWHM_x}$ is measured to be 0.89 µm, in good agreement with the simulated value. The focusing efficiency is measured to be 32.3%. We consider the presented experimental results to be in good agreement with the numerical simulation results. These serve as proof-of-concept results confirming the successful fabrication of a nanostructured diffractive microlens designed using the simple approach proposed.

## Conclusion

We successfully designed and fabricated a 20 µm-diameter nanostructured diffractive microlens with an NA of 0.49, operating at a wavelength of 0.8 µm and embedded 10 µm below the surface of a YAG crystal through 3D fs laser nanolithography. Numerical simulations predicted a near diffraction-limited focal spot with $\mathrm{FWHM_x}$ of 0.82 µm and a 34.4% focusing efficiency, which closely matched experimental results obtained with the fabricated microlens. This study demonstrates the efficacy of our fabrication method and validates the performance of the designed microlens, laying the groundwork for future photonic lab-on-a-chip applications.

## References

1. S. Banerji, M. Meem, A. Majumder, F. G. Vasquez, B. Sensale-Rodriguez, and R. Menon, "Imaging with flat optics: metalenses or diffractive lenses?," Optica **6**(6), 805 (2019).
2. A. Ródenas, M. Gu, G. Corrielli, P. Paiè, S. John, A. K. Kar, and R. Osellame, "Three-dimensional femtosecond laser nanolithography of crystals," Nat Photonics **13**(2), 105–109 (2019).
3. F. Paz-Buclatin, M. Esquivel-González, A. Casasnovas-Melián, O. de Varona, C. Cairós, J. M. Trujillo-Sevilla, K. Kamada, A. Yoshikawa, J. M. Rodríguez-Ramos, L. L. Martin, and A. Ródenas, "Circularly symmetric nanopores in 3D femtosecond laser nanolithography with burst control and the role of energy dose," Nanophotonics **12**(8), 1511–1525 (2023).
4. M. Plidschun, H. Ren, J. Kim, R. Förster, S. A. Maier, and M. A. Schmidt, "Ultrahigh numerical aperture meta-fibre for flexible optical trapping," Light Sci Appl **10**(1), 57 (2021).
5. A. Arbabi, Y. Horie, A. J. Ball, M. Bagheri, and A. Faraon, "Subwavelength-thick lenses with high numerical apertures and large efficiency based on high-contrast transmitarrays," Nat Commun **6**(1), 7069 (2015).

# Photovoltaic effect in monocrystalline lithium niobate films with nanoscale thickness

**Y. C. Zhang** [a], S. B. Li [a], J. J. Xu [a], G. Q. Zhang [a]

[a] The MOE Key Laboratory of Weak-Light Nonlinear Photonics,
School of Physics and TEDA Applied Physics Institute, Nankai University, Tianjin 300071, China

*zhangyuchen@mail.nankai.edu.cn

## Abstract:

The photovoltaic (PV) effect in lithium niobate (LN) was first observed in 1960s[1], and was found to be enhanced greatly in iron-doped LN crystals[2]. Nevertheless, the energy conversion efficiency $\eta$ is extremely low, usually in the range of $10^{-6}$~$10^{-4}$. Recently, the successful preparation of monocrystalline thin film LN on insulator (LNOI) by crystal-ion-slicing technology opens up the exploration of LN at nanoscale thickness and forges ahead for the development of opto-electronics, yielding memristor[3], domain-wall p-n junction[4], and vibrational energy harvester[5].

Here, the PV effect of LN with a nanoscale thickness was studied under the illumination of 325-nm irradiation, and it was found that the PV effect is originated from the Schottky barrier (1.15 eV) formed at the electrode/LN interface, different from the bulk PV effect reported previously in the bulk crystals. The structure of the PV device was shown schematically in Fig.1(a). With a light power density of 135 mW/cm$^2$, the dependence of short-circuit density ($|J_{sc}|$) and open-circuit voltage ($V_{oc}$) on LN film thickness $d$ is illustrated in Fig.1(b). The values of $|J_{sc}|$ and $V_{oc}$ were found to be 0.377 mA/cm$^2$ and 0.8 V, respectively, at a LN film thickness of 16 nm. Moreover, the $J$-$V$ characteristics are film-thickness dependent, as shown in Fig.1(c), mainly due to the increasing contribution of the polarization-induced asymmetric conduction from the bulk layer with the increase of film thickness. Interestingly, direct tunneling of electron was found to be the dominant conduction mechanism in ultra-thin LN films. The energy conversion efficiency $\eta$ was determined to be 0.1% at 16 nm. These results could be useful for developing integrated opto-electronic devices such as PV devices and photo-detectors based on LNOI.

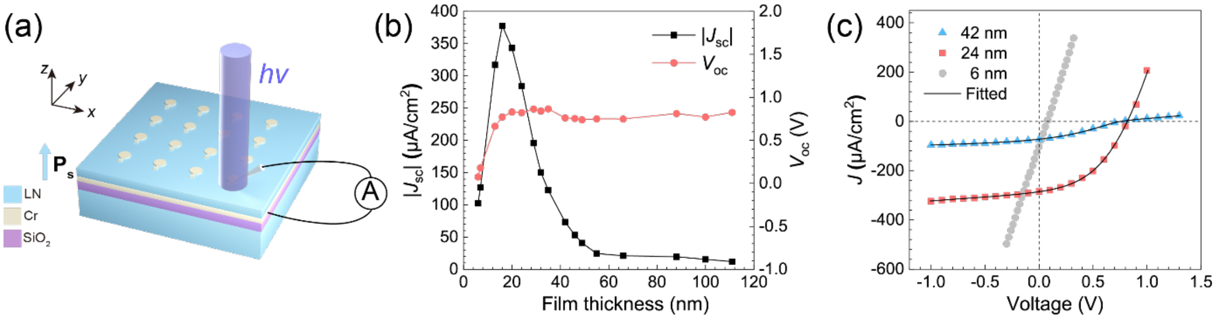

*Figure 1-* (a) Schematic structure of the PV device. (b) The dependence of $|J_{sc}|$ and $V_{oc}$ on the film thickness $d$. (c) The $J$-$V$ characteristics of the devices with different film thickness $d$.

## References

[1] F. S. Chen, J. Appl. Phys. **40,** 3389 (1969).
[2] A. M. Glass, D. von der Linde, and T. J. Negran, Appl. Phys. Lett. **25,** 233 (1974).
[3] J. P. V. McConville, H. D. Lu, B. Wang, Y. Tan, C. Cochard, M. Conroy, K. Moore, A. Harvey, U. Bangert, L. Q. Chen, A. Gruverman, and J. M. Gregg, Adv. Funct. Mater. **30,** 2000109 (2020).
[4] Y. Z. Qian, Y. C. Zhang, J. J. Xu, and G. Q. Zhang, Phys. Rev. Appl. **17,** 044011 (2022).
[5] G. Clementi, G. Lombardi, S. Margueron, M. A. Suarez, E. Lebrasseur, S. Ballandras, J. Imbaud, F. Lardet-Vieudrin, L. Gauthier-Manuel, B. Dulmet, M. Lallart, and A. Bartasyte, Mech. Syst. Signal Pr. **149,** 107171 (2021).

# Poling free $LiNbO_3$ waveguides for wide bandwidth nonlinear optical frequency conversion

M. Chauvet, A. Zinaoui, N. Courjal, L. Robert, S. Queste, L. Gauthier-Manuel, M. Suarez
*FEMTO-ST institute, UMR CNRS 6174, University of Bourgogne Franche-Comté, 15B Avenue des Montboucons, 25030 Besançon, France*

$LiNbO_3$ films are at the heart of an intense research activity due to a strong potential for RF components, exploiting piezoelectric properties, and for the development of integrated optical chips, using electro-optical and nonlinear properties [1-3]. Thanks to the latter property, optical frequencies conversion is possible which is a key process in many devices. For example, to realize intricated photon sources for optics, for MIR spectroscopy, and more generally to obtain new wavelengths from existing laser sources.

The most common approach for efficient frequency conversion in $LiNbO_3$ is based on inversing periodically its polarity (PPLN - Periodically Poled Lithium Niobate). Combining this technique with a waveguide with small effective guided mode cross section leads to normalized conversion efficiency as high as 2600 $\%/W/cm^2$ at telecom wavelengths [4]. However, it is restrained by a short conversion bandwidth, typically of a few nanometers near the central wavelength. One way to increase this bandwidth consists in using tailored aperiodic poling (step-chirped PPLN). For instance, a 100 nm bandwidth has been shown in ref [5] but at the expense of a modest conversion efficiency of 9.6 $\%/W/cm^2$. These cases display the trade-off between conversion efficiency and bandwidth response.

In the present work, we uncover a configuration for which a tailored high-index contrast $LiNbO_3$ waveguide provides a nonlinear second harmonic generation (SHG) with a record bandwidth response along with a high conversion efficiency. The frequency doubling component, that could also generate intricated photons, is based on a ridge waveguide built in a suspended thin $LiNbO_3$ membrane (Fig.1a). The phase matching between the two fundamental modes $TE_{00}$ (SH) and $TM_{00}$ (pump) is fulfilled thanks to a precisely designed waveguide cross section of few micrometers square. Standard Ti-indiffused waveguide are combined at the input and output of this nonlinear section with adiabatic tapered transition area to form a monolithic $LiNbO_3$ integrated component, as shown in Fig 1b. This arrangement greatly facilitates light coupling in the high confinement nonlinear section with a simple polarization maintaining singlemode fiber giving coupling losses less than 1dB.

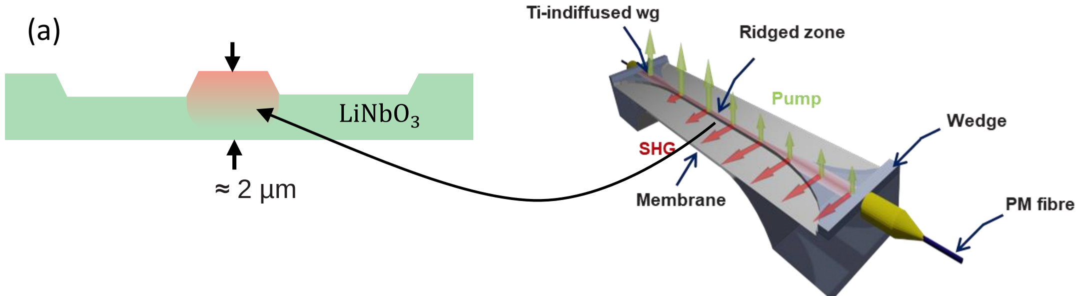

*Figure 1: Structure of the nonlinear ridge waveguide membrane (a) and artistic view of the developed suspended nonlinear ridge component integrated with input and output Ti-indiffused tapered regions.*

Numerical simulations reveal outstanding SHG characteristics for the integrated component. As an illustration, normalized conversion efficiency versus wavelength is shown in fig. 2 for a ridge waveguide 2µm wide and 2.15µm high and with a membrane 1.35µm thick. At room temperature phase matching is observed for two separate wavelengths centered near 1.4µm and 1.56µm, respectively. At a temperature of 30°C, the device depicts a broadband response exceeding 100 nm with a competitive efficiency approaching 60 %/W/cm$^2$ at telecom wavelengths.

The manufacturing process begins with the deposition of a 6 µm wide titanium ribbon which is further in-diffused at 1050 °C for 10 hours to form a singlemode waveguide at 1.55µm. The central ridge waveguide and the tapered region are then etched by reactive ion etching (RIE). At last a membrane is finally inscribed in the material by dicing-polishing with a precision circular saw (3350 DISCO DAD) at the back side of structure in the non-linear waveguide area. An RIE post-thinning process has been developed to achieve well-calibrated LiNbO$_3$ membrane thickness down to 500 nm still maintaining low propagation losses.

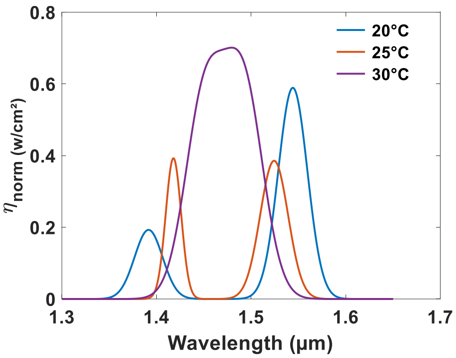

*Figure 2 :Calculated conversion efficiency for a ridge waveguide 2µm wide and 2.15µm high in a 1.35µm thick membrane at three different temperature values.*

Experimental results in accordance with the predicted performances have been recently obtained and will be presented in details.

## Conclusions

We have designed a LiNbO$_3$ waveguide enabling type-I second harmonic generation for the whole C-band telecommunication wavelengths by birefringence phase matching of fundamental SH and pump modes. The nonlinear component is based on a high confinement ridge waveguide made out of a thin LiNbO$_3$ membrane. Ultrawide response over 100nm along with a conversion efficiency near 50% are exposed. The performances extends to a wider range of wavelengths by temperature tuning. In addition, the elaborated device also includes Ti-indiffused standard waveguides that are adiabatically connected with the nonlinear ridge waveguide to provide an efficient and easy light coupling with singlemode fibers. This work uncovers configurations for which tailored high-contrast LiNbO$_3$ waveguides provide nonlinear conversion characteristics that can supplement PPLN structures.

## References

[1] J. Lu et.al, Optica **8**, 539-544 (2021).
[2] V. Pêcheur et. al., OSA continuum, 4, 1404-1414, (2021).
[3] M. Zhang et. al., optica **8**, 652-667 (2021)
[4] Wang, C. et. al. Optica 5, 1438 (2018)
[5] Wu, X. et al. Opt. Lett. 47, 1574 (2022)

# On-chip rare-earth doped lithium niobate waveguide amplifiers

**Y. Zhang** [a], Q. Luo [a], D. Zheng [a], S. Wang [b], H. Liu [a], F. Bo [a], Y. Kong [a], and J. Xu [a]

[a] MOE Key Laboratory of Weak-Light Nonlinear Photonics, School of Physics and TEDA Institute of Applied Physics, Nankai University, Tianjin 300071, China
[b] School of Science, Jiangsu University of Science and Technology, Zhenjiang 212100, China
* YuqiZhang@mail.nankai.edu.cn
* kongyf@nankai.edu.cn

The ability to amplify optical signals is of pivotal importance in photonic integrated circuits (PICs). Typically, rare-earth ions doped materials have the advantages of longer excited state lifetimes and less refractive index change caused by doped ion excitation, which promotes in-depth research on the PICs of rare-earth ions doped waveguide amplifiers and lasers with various passive components on a chip-scale platform.

Lithium niobate ($LiNbO_3$, LN) is considered one of the most promising photonic materials due to its excellent electro-, nonlinear- and acousto-optical properties, as well as its wide transparent window and relatively high refractive index [1]. LN on insulator (LNOI) has strong optical constraints and retains good bulk characteristics, making it the main thin film platform for building chip integrated devices. In the past few years, significant advancements have been made in the development of frequency comb source, electro-optic modulators, frequency converters, and photodetectors based on the LNOI platform. However, due to the indirect bandgap structure of LN, it is difficult to achieve active optical gain, an important function in PICs. A promising solution for developing active devices based on LNOI is to dope rare-earth ions into LN. Recently, significant progress has been made in the integration of active components such as amplifier and lasers based on the erbium (Er) doped LNOI platform, demonstrating the enormous potential for achieving high-performance scalable light sources on the LNOI platform [2].

Considering the significant progress made in rare-earth doped LNOI lasers and amplifiers, the fabrication of on-chip ytterbium (Yb) and erbium-ytterbium co-doped LNOI waveguide amplifiers based on electron-beam lithography and inductively coupled plasma reactive ion etching was investigated [3,4]. Under a 974 nm laser pump, a 5.0 mm long ytterbium doped LNOI waveguide amplifier is demonstrated with a maximum net internal gain of ~18 dB/cm achieved under an input signal power of approximately −51 dBm at 1064 nm. In addition, the demonstrated amplifiers exhibit the highest gain value for reported ytterbium doped LNOI waveguide amplifiers and show the advantages applied to weak-signal amplification in the 1064 nm band.

In addition, signal amplification emerges at a low pump power of 0.1 mW, and the net internal gain in the communication band is 16.52 dB/cm under pumping of a 974 nm continuous laser by erbium-ytterbium co-doped LNOI waveguide amplifier, as shown in Fig. 1. By analyzing the material properties, it was confirmed that the energy transfer from ytterbium and erbium ions in erbium-ytterbium co-doped LN resulted in higher pump efficiency ~10% under unidirectional pumping in the 980 nm band. Compared with erbium doped LNOI waveguide amplifiers, the internal conversion efficiency is greatly improved.

This work proposes new active devices for LNOI integrated optical systems that may become an important fundamental component of future lithium niobate photonic integration platforms. Through further optimization of Yb ions doping or co-doping concentration and mode overlap factors by designing suitable waveguide geometry, the rare-earth doped LNOI waveguide amplifiers are expected to exhibit better amplification performance.

This work was supported by National Key Research and Development Program of China (Grant No. 2019YFA0705000), the National Natural Science Foundation of China (Nos. 12034010, 12134007), Natural Science Foundation of Tianjin (Grant Nos. 21JCZDJC00300, 21JCQNJC00250), and Program for Changjiang Scholars and Innovative Research Team in University (No. IRT_13R29).

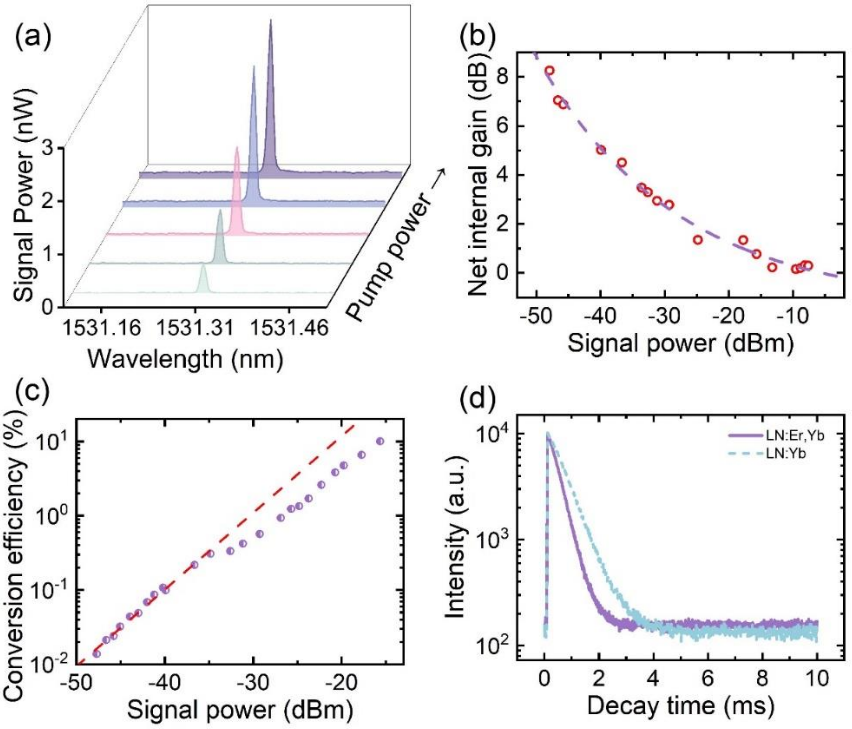

*Figure* 1. Gain characteristics of LNOI waveguide amplifier. (a) Measured signal spectra with increasing pump powers. (b) Net internal gain as a function of increasing signal power at a fixed pump power. (c) The measured internal conversion efficiency is used as a function of signal power. (d). Decay curves of the Yb$^{3+}$ emission at 1062 nm in erbium-ytterbium (Er$^{3+}$/Yb$^{3+}$) co-doped and ytterbium (Yb$^{3+}$) doped LN, excited under 980 nm.

## References

[1] Y. Kong, F. Bo, W. Wang, D. Zheng, H. Liu, G. Zhang, R. Rupp, and J. Xu, Adv. Mater. **32**, 1806452 (2020).

[2] Q. Luo, F. Bo, Y. Kong, G. Zhang, and J. Xu, Adv. Photon. **5**, (2023).

[3] Y. Zhang, Q. Luo, S. Wang, D. Zheng, S. Liu, H. Liu, F. Bo, Y. Kong, and J. Xu, Opt. Lett. **48**, 1810 (2023).

[4] Y. Zhang, Q. Luo, D. Zheng, S. Wang, S. Liu, H. Liu, F. Bo, Y. Kong, and J. Xu, Photonics Res. **11**, 1733 (2023).

# Period-halving intensity oscillation in Floquet photonic structures

Qianqian Kang, Zhaoyuan Wang, Xiaoqin Huang, Fengyi Cao, Zeyu Gong, Minglei Wang,
Yi Hu, Jingjun Xu

The MOE Key Laboratory of Weak-Light Nonlinear Photonics, School of Physics, Nankai University, Tianjin 300457, China

## Introduction

Floquet drive, which is to vary parameters of a system periodically [1,2], has received wide interest in acquiring non-trivial topological phenomena such as in cold atoms [3], photonics [4] and acoustics [5]. Using these platforms, researcher have started to test the idea of discrete time crystals. Spontaneous time-translation symmetry breaking, necessary to form a time crystal, has been reported in photonic crystals [6] and trapped atoms [7], which indicates that the oscillation period of an observable in a Floquet system is able to change. The representative phenomenon is period-doubling effect, where an observable in a Flouqet system oscillate twice as slow as the applied drive [8]. Then a natural question arises: can an observable oscillate faster than the drive? This question has not been concerned, since people usually think the minimum of the oscillation period is equal to the Floquet period.

In this work, we report an effect of period-halving oscillation based on a platform of photonic lattices. By allowing any two instantaneous Hamiltonians separated in a distance of a half period to meet a chiral symmetry, the zero mode in this system can repeat its intensity profiles every half period along the propagation, thereby leading to a period-halving effect. Such dynamics are unique for zero modes, while other modes in the same system still oscillate with the period of the Floquet drive.

## Main results

In Floquet photonic lattices, the waveguide parameters change periodically along the light propagation. The distance (i.e., $z$) is in analogy to time [3]. Thus, Floquet physics can be studied by means of light propagation. Generally, the Hamiltonian of a Floquet photonics lattice is described by $H(z)=H(z+T)$ (where $T$ is the period of drives). We add a constrain to this system, i.e.,

$$\Gamma H(z)\Gamma = -H(z+T/2), \tag{1}$$

where $\Gamma$ is a unitary transformation operator meeting $\Gamma=\mathrm{diag}[-1,1\ldots(-1)^N]$ ($N$ is the number of the waveguides in a photonic lattice). In this framework, the effective Hamiltonian, which is defined as $H_{\mathrm{eff}}(z_0)=(i/T)\ln(Fe^{-i\int_{z_0}^{z_0+T}H(z)dz})$ (where $z_0$ is an initial position and $F$ denotes time ordering), meets the following relationship,

$$\Gamma H_{\mathrm{eff}}(z_0)\Gamma = -H^*_{\mathrm{eff}}(z_0+T/2). \tag{2}$$

Then one can obtain from the above equation:

$$\varphi_{\varepsilon}(z_0+T/2)=\left[\Gamma\varphi_{-\varepsilon}(z_0)\right]^*, \tag{3}$$

where $\varphi(z_0)$ is the eigenstate of $H_{\mathrm{eff}}(z_0)$, and its subscript denotes the corresponding quasi-energy. If a zero mode exists in the system, one has $\varphi_0(z_0+T/2)=[\Gamma\varphi_0(z_0)]^*$. Then it can be readily obtained:

$$\left|\varphi(z_0)\right|^2=\left|\varphi(z_0+T/2)\right|^2. \tag{4}$$

In a Floquet system, the profile of an eigenstate evolving after a distance $L$ is exactly the one with the associated eigenvalue for $H_{\mathrm{eff}}(z_0+L)$. In this framework, one can infer that the zero mode is able to oscillate with $T/2$ in terms of photon number (i.e., intensity).

To illustrate such a period-halving effect, we use a photonic lattice including three waveguides [Fig. 1(a)] as a typical example. The longitudinal refractive index changes are employed as Floquet drives, which is called on-site drives. This kind of structures can be experimentally realized by using a light-induced method in nonlinear crystals [9][10]. Light propagation in this structure is governed by the following equations:

$$\begin{aligned}
i\partial_z\psi_1 &= -M\cos(2\pi/T\cdot z)\psi_1+\kappa(\psi_2),\\
i\partial_z\psi_2 &= \kappa(\psi_1+\psi_3),\\
i\partial_z\psi_3 &= M\cos(2\pi/T\cdot z)\psi_3+\kappa(\psi_2),
\end{aligned} \tag{5}$$

where $\psi_n$ ($n$ denotes lattice site) are complex amplitudes of electric fields of light in each waveguide, $M$ is the drive strength and $\kappa$ is the coupling coefficient between any two nearby sites. The Hamiltonian in this system satisfies the condition of Eq. (1). Three quasi-energies and the corresponding eigenstates of the effective Hamiltonian for a starting position at $z_0= T/3$ and $5T/6$ are presented in Figs. 1(b,c). Apparently, the intensity of the state for $\mp\varepsilon$ of $H_{\mathrm{eff}}$ ($z_0= T/3$) is the same with that for $\pm\varepsilon$ of $H_{\mathrm{eff}}$ ($z_0=5T/6$). From this particular case, one can infer that the modes with $\varepsilon=\pm0.57\pi$ do not have the period-halving effect. For the zero modes, their intensity distributions are always the same for any two effective Hamiltonians whose initial positions are separated by $T/2$, which is the basis of the period-halving effect and in accordance with Eq. (4).

Next, in order to verify the period-halving phenomenon, we experimentally measure the intensity distributions of two modes in each waveguide in a longitudinal period (i.e., $z\in[0,T]$) and present it in Figs. 1(d,e) in comparison with the simulated results based on Eq. (5) . Apparently, the intensity profile of the zero mode tends to reproduce itself after every $T/2$, which is direct evidence to support the period-halving effect. In contrast, the profiles of the other mode with a non-zero quasi-energy are quite distinct in two distances separated by $T/2$ in most cases. These results further show that the proposed Floquet system supports a period-halving effect.

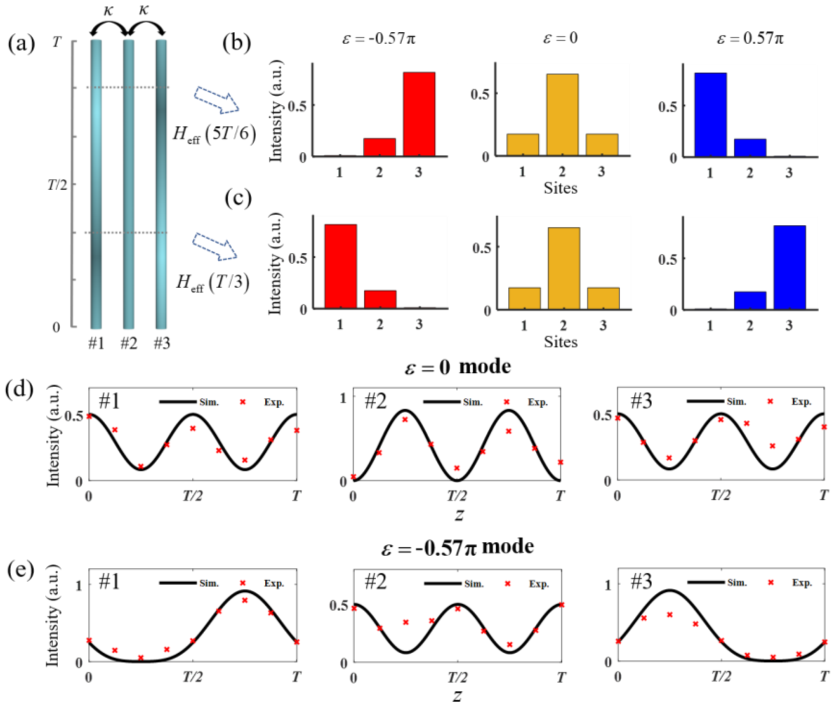

Fig. 1. (a) Sketch of three coupled waveguides upon on-site Floquet drives (brighter color stands for a larger modulation of refractive index). (b,c) show quasi-energies ( $\varepsilon$ ) and the corresponding eigenstates (in terms of intensity) for the structure in (a) where the drive period is $T$=4 cm and the drive strength is $M$=0.64$\kappa$: from down to up are the cases of effective Hamiltonians starting from the initial position $T/3$ and $5T/6$, and the same color represents the modes having the same quasi-energy. (d,e) Intensity distribution of the two modes with quai-energies of 0 (d) and -0.57$\pi$ (e) during propagation along each waveguide (#1, #2 and #3) in a Floquet period (red “x” represents experimental measurements and black solid lines are numerical results).

## References

[1] T. Oka and S. Kitamura, “Floquet engineering of quantum materials,” Annu. Rev. Condens. Matter Phys. **10**, 387-408 (2019).
[2] M. S. Rudner and N. H. Lindner, “Band structure engineering and non-equilibrium dynamics in Floquet topological insulators,” Nat. Rev. Phys. **2**, 229-244 (2020).
[3] A. Eckardt, “Colloquium: Atomic quantum gases in periodically driven optical lattices,” Rev. Mod. Phys. 89, 011004 (2017).
[4] M. C. Rechtsman, *et al*., “Photonic Floquet topological insulators,” Nature **496**, 196-200 (2013).
[5] R. Fleury, *et al*., “Floquet topological insulators for sound,” Nat. Commun. **7**, 11744 (2016).
[6] E. Lustig, *et al*., “Topological aspects of photonic time crystals,” Optica **5**, 1390-1395 (2018).
[7] J. Zhang, *et al*., “Observation of a discrete time crystal,” Nature **543**, 217-220 (2017).
[8] M. Sebabrata and M. C. Rechtsman, “Period-doubled Floquet solitons,” Optica **10**, 1310-1315 (2023).
[9] Z. Wang, *et al.*, “Floquet interface states between photonic lattices with opposite chirality,” Phys. Rev. A **106**, 053107 (2022).
[10] Z. Wang, *et al.*, “Floquet topological phases in a photonic simple lattice upon on-site drives,” Laser Photonics Rev. **17**, 2300037 (2023).

# Poster List

1. Accumulation of micro- and nano-plastics by electrohydrodynamic droplet dispensing for sensitive detection in salt-water**. P Camarero**
2. Small electron polarons bound to interstitial tantalum defects in lithium tantalate. **Julian Koelmann**
3. Exciton emissión enhancement in 1L-MoS2 on a ferroelectric substrate undergoing a ferro-to paraelectric phase transition. **D. Hernández-Pinilla**, Y. A. Xia, G. López-Polín, M. O. Ramírez, L. E. Bausá
4. 2-photon polymerization of patterned polarizers in SU-8 and S1805 photoresist alignment surface **B. Ganazhapa**, X. Quintana, M.A. Geday, M. Caño-García
5. Dynamics of a water droplet suspended in paraffin oil and subjected to a photovoltaic electric field**. A. Mendez**, A. Alcazar, A. García-Cabañes and M. Carrascosa
6. Lithium Niobate for Light-driven Actuation of Droplets. **Ana María Zaltron**
7. Unlocking Single-Particle Multiparametric Sensing: Decoupling Temperature and Viscosity through Upconverting Polarized Spectroscopy **Elisa Ortiz**
8. Brownian motion governs the plasmonic enhancement of colloidal upconverting nanoparticles. **Fengchan Zhang**
9. Microscale Optical Forces: Exploring Size and Electrostatic Influences **A. Dávila**
10. Submicro patterning in LiNbO3 by Fe ion implantation for the assessment of novel type of photovoltaic optoelectronic tweezers.**S. K. Padhi**
11. Harnessing Plasmon Resonances in Ni and Bi2Te3 Nanowire Networks for Enhanced Thermoelectric Performance. **O Caballero-Calero**
12. Three-dimensionally nanostructured waveguides inside optical crystals for on-chip instrumentation by fs-laser nanolithography. F. Paz-Buclatin**, P. Molina,** G. Martín, and A. Ródenas.
13. Dimensional analysis of Kukhtarev equations for the photorefractive effect. **A Alcazar,** A. Méndez, J.B. Ramiro.
14. Imprinting micro-patterns of photovoltaic charge onto non-photovoltaic dielectric substrates. **C. Sebastián-Vicente**
15. Anomalous small polarons mobility in defective oxides: the case of congruent lithium niobate. **L. Vittadello**
16. Small polaron trapping kinetics in iron-doped congruent lithium niobate. **M. Bazzan**
17. Optical control of ferroelectric liquids on ferroelectric solid substrates. **L. Lucchetti**,

# Accumulation of micro- and nano-plastics by electrohydrodynamic droplet dispensing for sensitive detection in salt-water

Poster contribution

**P. Camarero [1,2]**, E.Rincón [1], M. Hernando-Pérez [1,2,3], P. Haro-González [1,2,4],
A.García-Cabañes [1,2], M.Carrascosa [1,2]

[1] Departamento de Física de Materiales, Universidad Autónoma de Madrid, Madrid, Spain.
[2] Instituto Nicolás Cabrera, Universidad Autónoma de Madrid, Madrid, Spain.
[3] Condensed Matter Physics Center (IFIMAC), Universidad Autónoma de Madrid, Madrid, Spain.
[4]Institute for Advanced Research in Chemical Sciences, Universidad Autónoma de Madrid, Madrid, Spain.

*pablo.camarerol@estudiante.uam.es

Multiple and unique advantages of plastics, including affordability, lightweight design, and biodurability,[1] contribute to their widespread and excessive utilization both in industry and in daily life. Through the fragmentation of larger plastics, micro- and nano-plastics are generated through chemical or physical processes, making plastic pollution a major concern in environmental research. To identify these pollutants within marine environments, several microscopic techniques such as Atomic Force Microscopy and Transmission Electron Microscopy followed by analytical methods such as Raman spectroscopy and FTIR spectroscopy, are employed.[2] However, detecting low-concentration samples of micro- and nano-plastics in water is challenging due to their weak signals.

In view of this, we propose a technique for accumulating micro- and nano-plastics to facilitate Raman spectroscopy. This method relies on an optoelectronic platform capable of generating high light-induced electric fields through the bulk photovoltaic effect (PVE). $LiNbO_3$:Fe, a commonly used ferroelectric material, serves as the active material for this platform.[3] The precision of the technique, along with its versatility in handling liquids and non-invasiveness, makes it ideal for use with biological samples.[4] To the best of the authors' knowledge, this is the first instance of using PVE to induce droplet ejection for plastic accumulation.

To generate the photovoltaic response of the substrate, a frequency-doubled Nd:YAG operating at 532 nm illuminates a $LiNbO_3$:Fe crystal (surface size ≈ 7 x 9 $mm^2$) cut from a 1 mm thick z-cut wafer (0.25 % mol Fe-doped). When a micro-drop reservoir approaches the crystal, the strong light-induced electric field results in an attractive force between them, resulting in a significant number of droplets being ejected towards the crystal. The experimental setup, illustrated in Fig.1(a), allows the excitation of the crystal while visualizing the droplet ejection process using lateral and upper CMOS cameras. The lateral camera monitors the deformation of the reservoir drop during illumination and to ensure the avoidance of undesired bridge structures.[5] Additionally, the upper camera facilitates alignment between the center of the reservoir drop and the laser, as misalignment can lead to non-vertical droplet ejection. The inset figure illustrates the positioning of the $LiNbO_3$:Fe crystal on a separate platform, approximately 7 mm away from the slide. This platform features a hole enabling the ejected droplets from a bigger reservoir drop to reach the bottom surface of the crystal.

Reservoir drops containing micro- (1 µm diameter monodisperse polystyrene spheres from Polybead 19822) or nano-plastics (140 nm monodisperse polystyrene spheres from microParticles GmbH PS140) in aqueous solutions are placed on a conventional slide, held by a mobile platform allowing movement along all three axes. The ejected droplets reach the bottom part of the crystal and, due to their tiny volume (nL), evaporate immediately upon reaching the surface, depositing their contents onto the crystal surface and strongly adhering to it. This process results in patterns that serve as a record of the distribution of the ejected droplets. Consequently, the accumulated plastic patterns exhibit radial symmetry, as the material dispensed depends on both light intensity and induced electric field. Throughout the ejection process, as previously

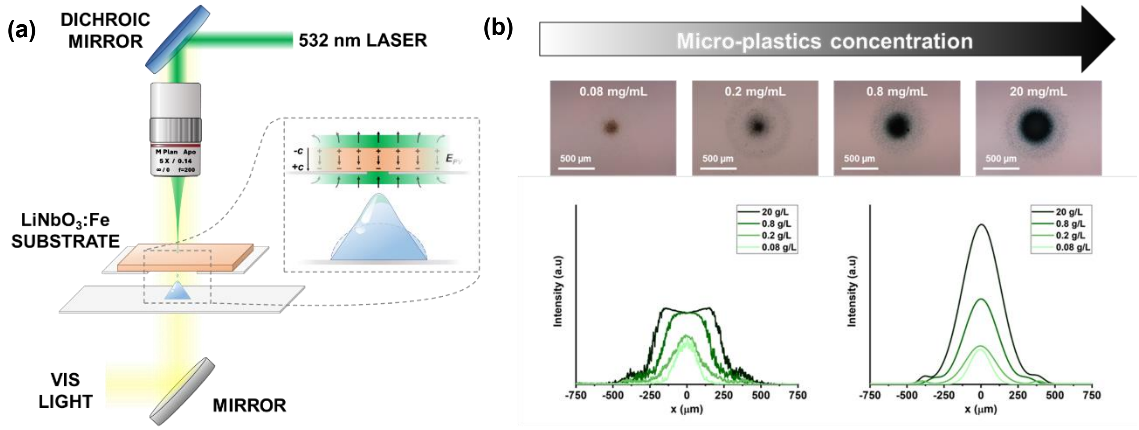

*Figure 1.* (a) Experimental set up of the droplet ejection system. Inset: deformation of the reservoir drop by the electro photovoltaic field. (b) Accumulation of the micro-plastics depending on the concentration of the reservoir drop.

reported, hundreds of droplets are dispensed.[5] These patterns follow a Gaussian-like distribution.

The effect of the elemental parameters of the set-up, such as the initial reservoir drop concentration (Fig.1(b)) or the ejection time, on the deposition of material on the substrate and the pattern formed has been studied. First results show that the gaussian-like pattern of deposited plastics does not depend on the concentration of the plastics. In turn, the number of plastics deposited decreases when the concentration and the ejection time do.

Additionally, we evaluated the role of salinity in salt-water (containing NaCl) of micro-plastic accumulation to simulate seawater conditions. Reservoir droplets with polystyrene (1 µm diameter spheres from Sigma-Aldrich 72938) at a concentration of 0.95 g/L and diverse NaCl concentrations have been ejected. Results show that NaCl concentration affects the gaussian-like distribution, decreasing the full width at half maximum (FWHM) as salt concentration increases. It was also found that the minimum polystyrene concentration in the reservoir droplet needed to accumulate plastics increases with the salt concentration, i.e. the sensitivity of the technique decreases with salinity.

In conclusion, the viability of a novel technique using optoelectronic platforms for the manipulation and deposit of micro- and nano-plastics in saline water is demonstrated. Further results demonstrate the applicability of the technique when it is applied in biological saline solutions (Phosphate Buffer Solution) and marine water.

This work was financed by Grant TED2021-129937B-I00, CNS2022-135495, PID2019-106211RB-I00, PID2020-116192RB-I00 and PID2023-151078OB-I00 funded by MCIN/AEI/10.13039/501100011033 and by the “European Union NextGenerationEU/PRTR. P. Camarero acknowledges Programa Investigo (Plan de Recuperación, Transformación y Resiliencia) which was developed thanks to SEPE, Ministerio de Trabajo y Economía Social and the European Union through NextGenerationEU.

## Refrences

1. Zaki, M.R.M. and A.Z. Aris, *An overview of the effects of nanoplastics on marine organisms.* Science of The Total Environment, 2022. **831**: p. 154757.
2. Mariano, S., et al., *Micro and Nanoplastics Identification: Classic Methods and Innovative Detection Techniques.* Frontiers in Toxicology, 2021. **3**.
3. García-Cabañes, A., et al., *Recent Achievements on Photovoltaic Optoelectronic Tweezers Based on Lithium Niobate.* Crystals, 2018. **8**(2): p. 65.
4. Muñoz-Cortés, E., et al., *Optoelectronic generation of bio-aqueous femto-droplets based on the bulk photovoltaic effect.* Optics Letters, 2020. **45**(5): p. 1164-1167.
5. Puerto, A., et al., *Droplet Ejection and Liquid Jetting by Visible Laser Irradiation in Pyro-Photovoltaic Fe-Doped LiNbO3 Platforms.* Advanced Materials Interfaces, 2021. **8**(22): p. 2101164.

# Small electron polarons bound to interstitial tantalum defects in lithium tantalate

A. Pfannstiel [a], T. Hehemann [a], N. A. Schäfer [b], S. Sanna [b], Y. Suhak [c], L. Vittadello [a,d], F. Sauerwein [a], N. Dömer [a], **J. Koelmann** [a], H. Fritze [c] and M. Imlau [a,d]

[a] Institute of Mathematics/Informatics/Physics, University of Osnabrück,
Barbarastraße 7, D-49076 Osnabrück, German
[b] Institut für Theoretische Physik and Center for Materials Research (ZfM/LaMa), Justus-Liebig - Universität Gießen, Heinrich-Buff-Ring 16, D-35392 Gießen, German
[c] Institut für Energieforschung und Physikalische Technologien, Technische Universität Clausthal, Am Stollen 19 B, D-38640 Goslar, Germany
[d] Center for Cellular Nanoanalytics, University of Osnabrück, Barbarastraße 11, D-49076 Osnabrück, | Germany

mimlau@uni-osnabrueck.de

Small electron polarons, i.e. electrons self-trapped at essentially one site in condensed matter by strong, short-range interaction of the carrier with the surrounding lattice, determine the electrical and optical properties of polar oxides to a large extend. The characteristic small polaron binding energy is considerably enhanced by the extra potential of lattice defects, resulting in a complete lattice site localization at even modest irregularities, i.e. yielding small bound polarons. These polarons can move through the lattice via hopping transport, either assisted thermally or through the absorption of photons.

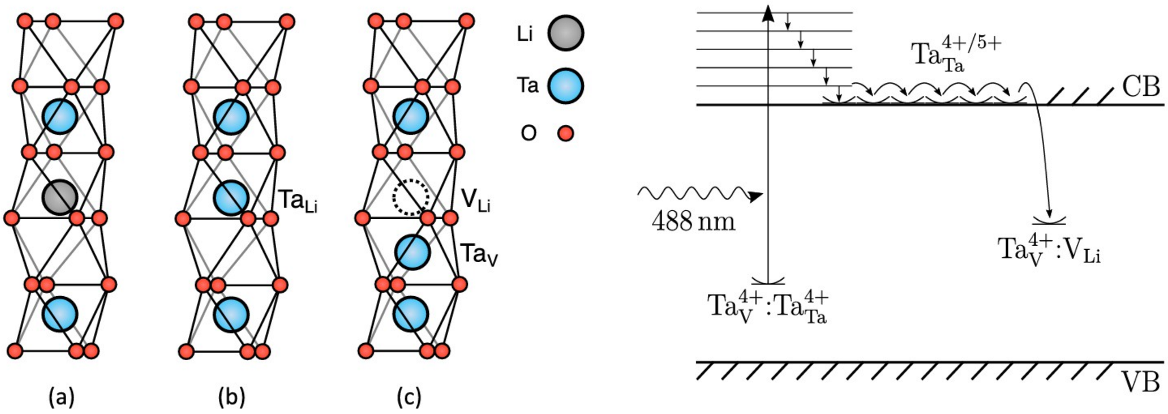

Figure 1 (left): Initial defect structure in LT, structural models of (a) defect free $LiTaO_3$, (b) Lt with $Ta_{Li}$ antisite, and (c) Lt with $Ta_V$:$V_{Li}$ interstitial defect pair. (right): Sketch of the formation process of interstitial polarons assuming the initial presence of bipolarons.

Here [1], the absorption features of optically generated, short-lived small bound electron polarons are inspected in lithium-tantalate, $LiTaO_3$ (cLT), grown from the congruent melt. In accordance with investigations from first principles, the presence of both lithium vacancies $V_{Li}$ and $Ta_{Li}$ antisite defect clusters can be considered to ensure charge compensation. The defect model for LT further allows the presence of another defect center, the interstitial $Ta_V$ defect. Here, the Ta ion is incorporated on Li vacancy. The different structural models for the different polaron spezies can be seen in figure 1 (left). Structural investigations furthermore suggest that both the antisite defect $Ta_{Li}$ and the interstitial defect $Ta_V$ could be present in LT.

The absorption features are investigated in order to address the question whether it is possible to localize electrons at interstitial $Ta_V$:$V_{Li}$ defect pairs by strong, short-range electron-phonon coupling. Solid-state photoabsorption spectroscopy under light exposure and density functional theory are used for an experimental and theoretical access to the spectral features of small bound polaron states and to calculate the binding energies of the small bound $Ta_{Li}^{4+}$ (antisite) and $Ta_V$:$V_{Li}$ (interstitial site) electron polarons. As a result, two energetically well separated ($\delta E \approx 0.5$ eV) absorption features with a distinct dependence on the probe light polarization and peaking at 1.6 eV and 2.1 eV are discovered, as seen in Figure 2. It can be concluded that the respective separation of their optical fingerprints as suggested by the experimental and theoretical data is due to a difference of the polaron binding energies between interstitial and antisite polarons by about 0.5 eV, with a lower value for the interstitial case. The presented discrepancy in the determination of the band gap energy between experiment and theory is attributed to an overestimation of the electronic gap in the GW calculation.

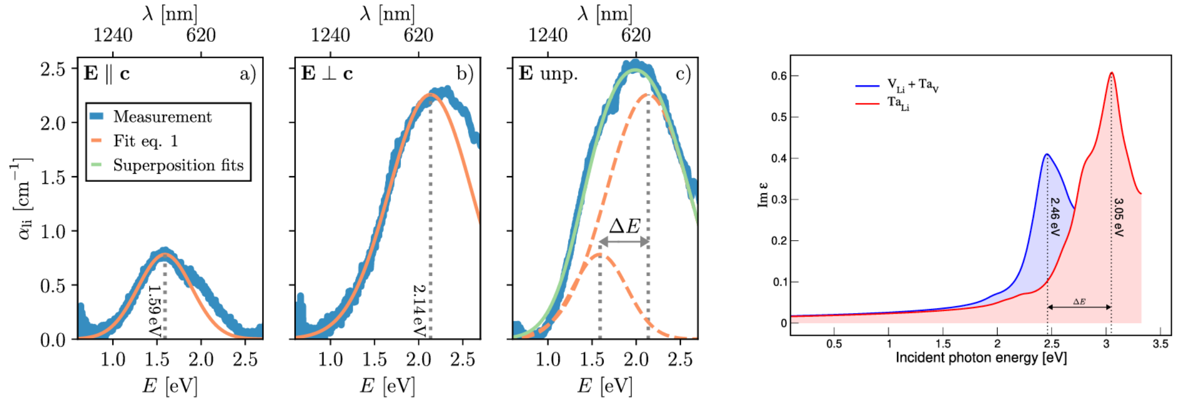

Figure 2: (left): Absorption spectra of c-LT in the illuminated state at T = 80 K and using polarized probe light with a) E∥c-axis, and b) E⊥c-axis. The spectrum in c) is determined without polarizer in the optical paths. The orange lines represents fits to the data sets of a), b), that are used to reconstruct the spectrum in c) by minor amplitude scaling. (right): DFT approximation for $LiTaO_3$ supercells modelling small bound polarons as a $Ta_{Li}$ antisite (red line) or as a $Ta_V$ interstitial close to a lithium vacancy $V_{Li}$ (blue line). The polaronic signatures associated to the two different microscopic models are separated by about 0.6 eV.

We contrast our results to the interpretation of a single small bound $Ta_{Li}^{4+}$ electron state with strong anisotropy of the lattice distortion and discuss the optical generation of interstitial $Ta_V^{4+}$:$V_{Li}$ small polarons in the framework of optical gating of $Ta_V^{4+}$:$Ta_{Ta}^{4+}$ bipolarons.

We can conclude that the appearance of carrier localization at $Ta_V$:$V_{Li}$ must be considered as additional intermediate state for the 3D hopping transport mechanisms at room temperature in addition to $Ta_{Li}$, as well [2], and, thus, impacts a variety of optical, photoelectrical and electrical applications of LT in nonlinear photonics. Furthermore, it is envisaged that LT represents a promising model system for the further examination of the small-polaron based photogalvanic effect in polar oxides with the unique feature of two, energetically well separated small polaron states.

## Acknowledgment

We gratefully acknowledge financial support by the Deutsche Forschungsgemeinschaft (DFG) through the research group FOR5044 (Grant No. 426703838, SA1948/3-1, IM37/12-1, SU12611/1-1, FR1301/42-1). Calculations for this research were conducted on the Lichtenberg high-performance computer of the TU Darmstadt and at the Höchstleistungsrechenzentrum Stuttgart (HLRS). The authors furthermore acknowledge the computational resources provided by the HPC Core Facility and the HRZ of the Justus-Liebig-Universität Gießen.

## References

[1] Anton Pfannstiel et al. “Small electron polarons bound to interstitial tantalum defects in lithium tantalate”. In: *Journal of Physics: Condensed Matter* (May2024). doi: 10.1088/1361-648X/ad4d47.

[2] Niklas Dömer u. a. “Long-lived, pulse-induced absorption in LiNb1−xTaxO3 solid solutions: the case of three intrinsic defect sites for electron localization with strong coupling”. März 2024. arXiv: 2403.16274 [cond-mat.mtrl-sci]

# Exciton emission enhancement in 1L-MoS₂ on a ferroelectric substrate undergoing a ferro-to paraelectric phase transition

**D. Hernández-Pinilla** [a,b*], Y. A. Xia [a], G. López-Polín [a], M. O Ramírez [a,b,c], L. E. Bausá [a,b,c]

[a] Dept. Física de Materiales, Universidad Autónoma de Madrid, Madrid, Spain
[b] Instituto de Ciencia de Materiales Nicolás Cabrera, Universidad Autónoma de Madrid, Madrid, Spain
[c] Condensed Matter Physics Center (IFIMAC), Universidad Autónoma de Madrid, Madrid, Spain

* david.hernandezp@uam.es

$MoS_2$ monolayer (1L-$MoS_2$) is a 2D semiconducting material with excellent optoelectronic properties with potential impact in a variety of areas such as spintronics, optoelectronics and integrated circuitry [1]. Because of its atomic thickness nature, this material provides the possibility of engineering its properties by means of its surrounding environment. In this regard, ferroelectric substrates have demonstrated the ability to modify the carrier concentration of 2D materials, thereby enabling the manipulation of their electronic and optical properties [2,3]. This capability facilitates the development of novel non-volatile, and reconfigurable 2D materials with multiple optoelectronic applications [4].

In this study, the relaxor-ferroelectric Strontium Barium Niobate (SBN) crystal, $Sr_{0.6}Ba_{0.4}(NbO_3)_2$, with a low Curie temperature (Tc ~ 70ºC), is used as a substrate for a 1L-$MoS_2$ (Figure 1a). Figure 1b shows a schematic representation of the SBN ferroelectric crystal and its effect on the 1L-$MoS_2$. The illustration depicts the doping of 1L-$MoS_2$ induced by a $P_{down}$ ferroelectric substrate, which is rich in negative interface charges. The interaction produces a p-type character in 1L-$MoS_2$.

Here, we aim to control the charge carrier density of 1L-$MoS_2$ by utilizing the SBN transition from ferro-to-paraelectric state. In turn, the potential modulation of the charge carrier density will affect the optoelectronic properties of the 2D material, with holds potential for switching and sensing applications.

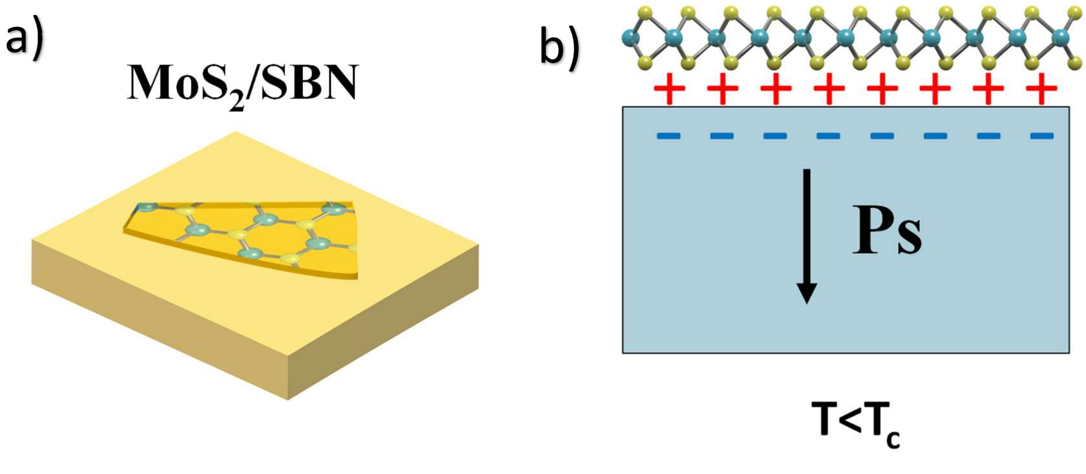

*Figure 1* – Schematic representations of a) 1L-$MoS_2$ on top of the polar surface of SBN crystal, and b) surface doping and polarization charge distribution in 1L-$MoS_2$/SBN for a $P_{down}$ ferroelectric crystal below Tc.

The redistribution of charge along the phase change is analyzed by means of μ-photoluminescence (PL) experiments. To this aim, the evolution of the 1L-$MoS_2$ PL under 488-nm excitation is followed in the 30-90ºC temperature range.

Figure 2a shows the obtained results, which reveal a notable modification of the 1L-$MoS_2$ PL when comparing the spectra below (blue) and above (red) the ferro-to-paraelectric phase transition of SBN. The spectra show an asymmetric shape due to the contribution of two resonances labelled as A and $A^-$ in the figure. The A peak corresponds to the neutral exciton emission centered at around 660-665 nm, while the $A^-$ band centered over 675 nm corresponds to trions. It is well known that the ratio between the contribution of excitons and trions into the emission of 1L-$MoS_2$ is determined by the carrier concentration density in the layer [5]. In particular, for the case depicted in Figure 1b, a $P_{down}$ domain induces a p-type doping charge balance at the 1L-$MoS_2$/SBN interface that results into a predominant emission from A excitons from that domain.

Contrary to what might be expected, the increase in temperature does not cause an emission quenching, but rather a significant enhancement of the 1L-$MoS_2$ PL. This enhancement is correlated with a boost of the exciton population produced by the varying interface charge balance along the phase transition of the SBN substrate. Figure 2b shows the evolution of the $I_{exciton}/I_{trion}$ in the temperature range of 30-90 ºC. As observed, the obtained ratios exhibit a gradual enhancement of the exciton population in 1L-$MoS_2$ due to the relaxor ferro-to-paraelectric phase transition. The ratio remains constant in the paraelectric phase where the spontaneous polarization of SBN is zero (see scheme in Figure 2c).

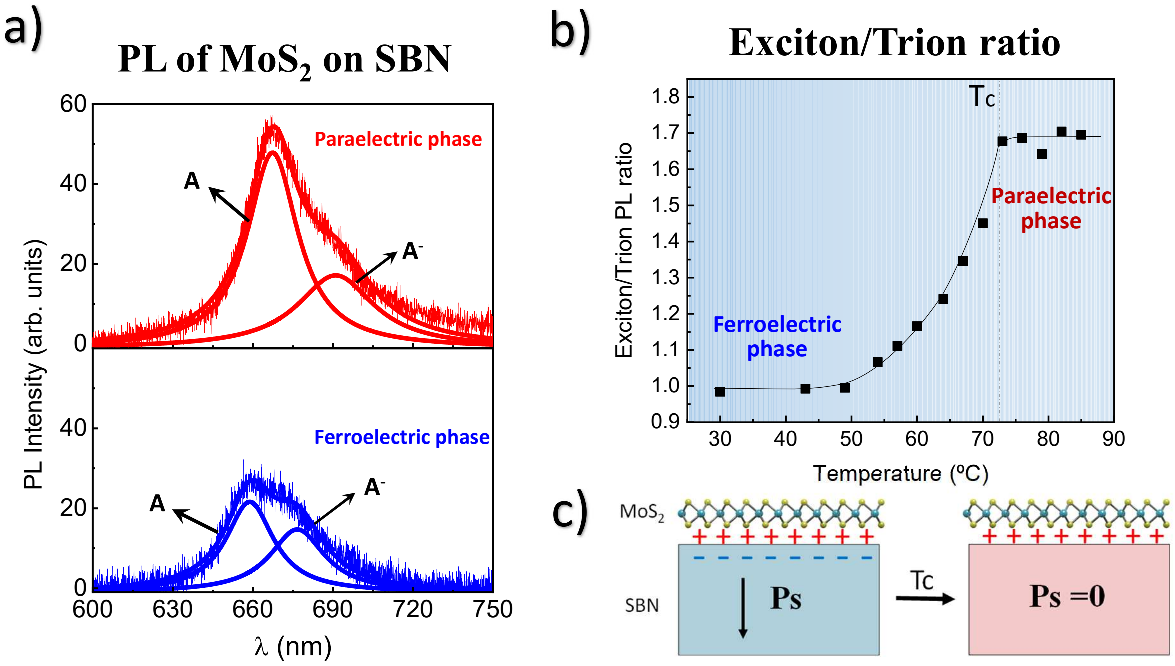

*Figure 2* – a) 1L-$MoS_2$ PL spectra above (red) and below (blue) the ferro-to-paraelectric phase transition of SBN. b) Evolution with temperature of the ratio of exciton and trion populations contributing to 1L-$MoS_2$ PL on an SBN substrate undergoing a ferroelectric to paraelectric phase transition. c) Schematic representation of the surface doping of 1L-$MoS_2$ due to SBN polarization in ferroelectric (left) and paraelectric (right) phase.

The work highlights the importance of the association of 2D materials and ferroelectrics to boost the concentration of excitons and paves the way for cutting-edge switchable devices in the fields of photonics and optoelectronics.

## References

[1] K. Mak, J. Shan. *Nat. Photonics*, 10, 216 (2016).
[2] L. Lv, F. Zhuge, F. Xie, et al. *Nat. Commun.*, 10, 3331 (2019).
[3] M. O Ramírez, J. Fernandez-Tejedor, D. Gallego, et al. *Adv. Opt. Mater.* 2400624 (2024).
[4] Q. Liu, S. Cui, R. Bian, et al. *ACS Nano* 18, 1778 (2024).
[5] S. Mouri, Y. Miyauchi, K. Matsuda. *Nano Lett.* 13, 5944 (2013).

# 2-photon polymerization of patterned polarizers in SU-8 and S1805 photoresist alignment surface

**B. Ganazhapa ***[a,b], X. Quintana [a], M.A. Geday [a], M. Caño-García [c]

[a] CEMDATIC, ETSI Telecomunicación, Universidad Politécnica de Madrid, Av. Complutense 30, 28040, Madrid, Spain.
[b] LASING S.A., c/Julián Camarillo, 26, 28037, Madrid, Spain.
[c] Department of Electronics and Computer Technology, Research Centre for Information and Communication Technologies (CITIC-UGR), University of Granada, Granada, Spain.

* b.ganazhapa@upm.es

Patterned polarizers are prepared using liquid crystals (LC) doped with dichroic dye and photopolymerization to create patterns for surface alignment in photoresists. Alignment techniques are commonly employed to generate complex aligned films [1] – *e.g.,* photoalignment with uniform UV exposure is used to create uniformly aligned films with multiple exposures, or direct laser writing (DLW) with a UV beam laser – but they allow for limited resolution in surface alignment. If high-resolution alignments on the same surface are required, new fast and efficient techniques are explored for creating nano-grooves in conventional photoresist [2].

In this work, surface alignment using 2-photon polymerization direct laser writing (2PP-DLW) technique is employed to create high-resolution groove patterns at arbitrary angles in both negative-tone and positive photoresists. These angles determine the orientation of the LC molecules at any point on the substrate surface, thereby determining the brightness intensity within the patterns in combination with a linear polarizer. Two complementary photoresists are utilized (see Figure - a): the conventional negative-tone SU-8 photoresist and, in this context novel, positive-tone S1805 photoresist. Customized equipment (depicted in Figure - b) has been designed and constructed for this purpose. The equipment is equipped with a 780 nm and 250 mW femtosecond fiber laser to induce 2PP. It also has a number of CNC stages, including xyz nano-positioners based on galvanometers (x,y) and a piezoelectric unit (z-axis), as well as coarse 200x200 mm$^2$ x,y micro-positioners to deal with large samples. Preliminary tests have successfully produced repetitive submicron complex patterns in LC without dichroic dye, which are compared with patterns obtained using dye-doped LCs.

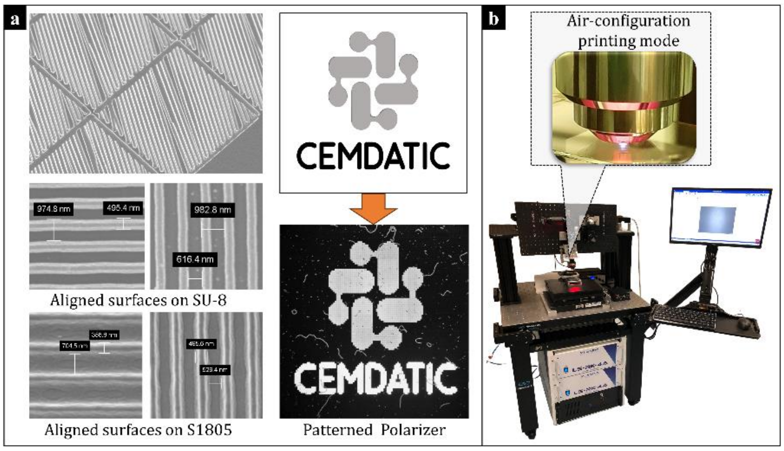

*Figure* - a) SEM images of aligned surfaces of patterned grooves on SU-8 and S1805 photoresist. b) Custom-built 2PP equipment.

## References

[1] Myhre, G., “Patterned Liquid Crystal Polymer Retarders, Polarizers, and Sources,” The university of Arizona, doctoral Thesis, (2012).

[2] Shi, Y. et al, “Two-photon laser-written photoalignment layers for patterning liquid crystalline conjugated polymer orientation,” Adv. Funct. Mater. 31, 2007493 (2021).

# Dynamics of a water droplet suspended in paraffin oil and subjected to a photovoltaic electric field

**A. Méndez** [a], A. Alcázar [a], M. Carrascosa [b], A. García Cabañes [b]

[a] Departamento de Mecánica de Fluidos y Propulsión Aeroespacial, ETSIAE, Universidad Politécnica de Madrid, Madrid, Spain
[b] Departamento de Física de Materiales, Universidad Autónoma de Madrid, Madrid 28049, Spain

* angel.mendez@upm.es

The electric field generated by illuminating ferroelectric substrates with a strong bulk photovoltaic effect has been widely used to manipulate micro- and nano-objects through electrophoretic and dielectrophoretic forces [1]. This photovoltaic optoelectronic tweezer has been introduced as a very interesting alternative to other optoelectronic tweezers because it operates at low light intensities and does not need electrodes or additional power supplies [2]. They are based on the bulk photovoltaic effect, which allows for the light-induced generation of very high electric field patterns (100–200 kV/cm) inside certain ferroelectrics, such as $LiNbO_3$. Additionally, these fields persist even after the illumination ceases, thereby avoiding other effects like heating and temperature fluctuations. However, manipulating particles via electric fields becomes difficult when they are immersed in a polar medium like water due to its high electric field screening effects. One solution to this problem involves immersing the aqueous droplets in a nonpolar immiscible oil, such as paraffin. However, it is necessary to ensure a minimum distance between the droplet and PV substrate, which can be achieved when the droplet is deposited on the surface of a suitable oil in a manner that allows it to hang at the oil-air boundary due to the surface tension contribution of the three fluids involved in the process (oil, water, and air). This experimental setup involves the combination of various forces, and the theoretical study of the interactions between them is highly complex, and, as far as we know, has not been extensively studied.

This work studies the dynamics of a small droplet of water suspended at the interface between oil and water in a container filled with liquid paraffin and immersed in an electric field. First, we examine the steady state of the droplet in the absence of the electric field. In this case, the position of the droplet depends on the interaction between two weak forces: gravity and surface tension [3]. Therefore, a sufficiently small droplet can be suspended at the interface. Once the droplet is stabilized (which occurs within a small fraction of a second), we analyze its interaction with a nonhomogeneous electric field. We performed these simulations with the help of the commercial software COMSOL Multiphysics©.

We use a two-dimensional simulation model based on the three-phase field method [4], in which we define three domains: D1 filled with air, D2 at the bottom filled with paraffin, and a circle of 1,4 mm diameter between both filled with water. The entire geometry is meshed with triangles.

In the first step, we define three immiscible phases, one for each fluid, and solve the Navier-Stokes equations and the three-phase Cahn-Hilliard equations to obtain the droplet's movement until it reaches a steady-state suspension by surface tension forces. The Cahn-Hilliard approach assumes that the interface thickness between two phases in the system is small but larger than the actual physical thickness, allowing it to be set to the size of the calculation element and providing greater stability to the simulation. Each phase is described geometrically by a smooth function $\Phi_i$, known as the "order parameter," which equals 1 in phase i and 0 outside of it, and varies continuously at the interfaces between phase i and the other phases. The temporal study of each parameter $\Phi_i$ enables us to analyze the evolution of each fluid in the system [5].

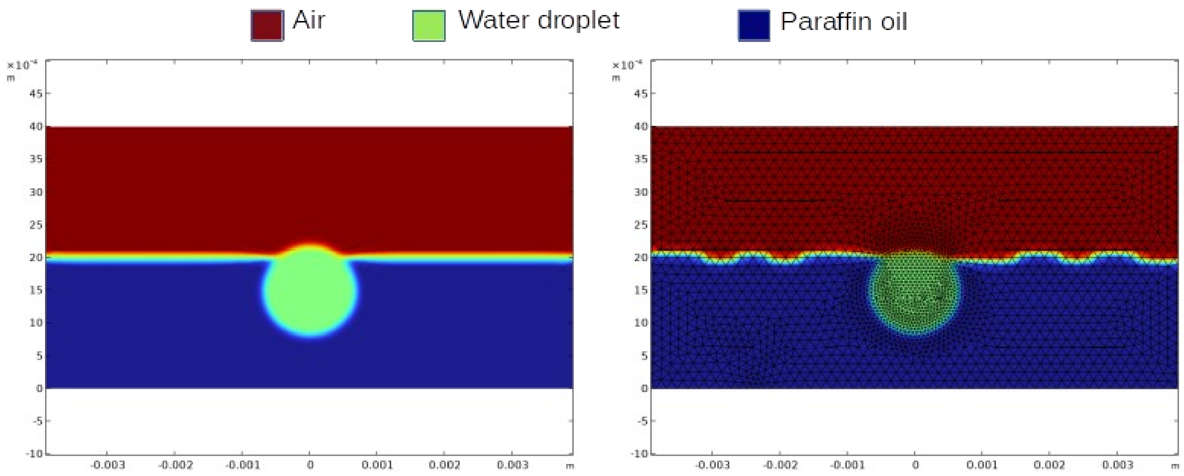

(a) (b)

Figure 1: Schematic representation of a water droplet deposited on a paraffin-air interface. Image (a) shows the droplet at t=0, before stabilization due to surface tension. Image (b) shows the droplet after stabilization, with the triangles used to mesh the simulation area also depicted. These triangles are chosen to be smaller than the thickness of the interface for simulation stability purposes.

Once the droplet is stabilized, we calculate the effect of a Z-cut, 1 mm deep, LiNbO3 substrate placed at the bottom of the container and illuminated by a homogeneous 532 nm, 2 mm laser beam of 10 $W/m^2$. This light leads to a negative charge accumulation at the crystal's surface, which can be calculated by solving the steady-state solution of the Kukhtarev equations for the photovoltaic effect in Z-cut lithium niobate substrates. In this case, the diffusion term has been disregarded [6]. The water droplet begins to move and approaches the illumination region due to the evanescent electric field components generated by the $LiNbO_3$ substrate, which induce DEP forces on the droplet.

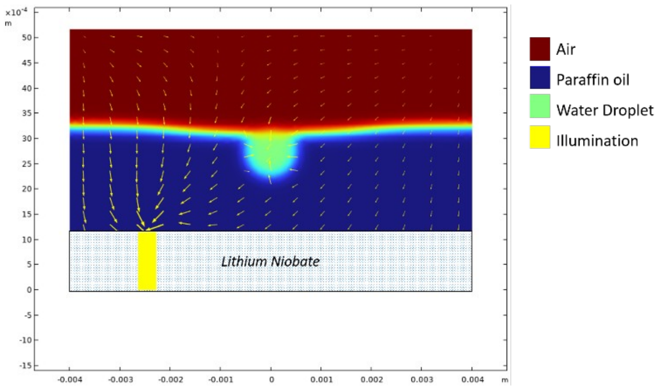

Figure 2: Schematic representation of a water droplet suspended at a paraffin-air interface. The arrows depict the dielectrophoretic force induced by a photovoltaic field generated via the illumination of a Z-cut iron-doped lithium niobate crystal.

## References

[1] M. Carrascosa, A. Garcia-Cabañes, M.Jubera, J.B. Ramiro et al Appl. Phys Rev 2, 040605 (2015)
[2] A Puerto, A Méndez, L Arizmendi, A García-Cabañes et al, Phys. Rev. Appl.14, 024046 (2020)
[3] D George, S. Damodara, R. Iqbal, A.K. Sen, Langmuir, 32 10276 (2016)
[4] Hu, Q.; Hu, F.; Xu, D.; Zhang, K. *Micromachines 14*, 951 (2023)
[5] Boyer, F., Lapuerta, C., Minjeaud, S., Piar, B. *et al. Transp Porous Med* **82**, 463–483 (2010).
[6] C. Arregui, J. B. Ramiro, A. M. Alcazar, A. Mendez et al, J. Eur. Opt. Soc.-RP, 10, 15026, (2015)

# Lithium Niobate for Light-driven Actuation of Droplets

**A. Zaltron**, S. Cremaschini, R. Zamboni, A. Cattelan, D. Ferraro, D. Filippi, F. Marinello, A. Meggiolaro, M. Pierno, L. Lucchetti, C. Sada, P. Umari, G. Mistura

Department of Physics and Astronomy, University of Padua, Italy

* annamaria.zaltron@unipd.it

The actuation and control of liquid droplets is a key function in many microfluidic applications, both in scientific research and industry. Over the years, several strategies have been employed to accomplish this task and optical approaches have recently emerged, thanks to the high versatility and reconfigurability of the optofluidic devices. In this work, we present an optofluidic platform based on a iron-doped z-cut lithium niobate crystal (Fe:LiNbO3): the remarkable photovoltaic, piezoelectric and pyroelectric properties of this material have been synergically employed to actuate, merge and split water droplets, solely by using laser beams [1]. The engineering of the Fe:LiNbO3 surface with a lubrificated-infused layer (LIS) guarantees a very slippery and robust device, suitable for prolonged use and the manipulation of water droplets with volumes up to some microliters [2]. Furthermore, the remarkable light-induced properties of LiNbO3 can be used to actuate also other liquids, as the case of nematic liquid crystals (LCs), thus representing an innovative approach for achieve a full light-driven actuation also in LCs-based technology [3,4].

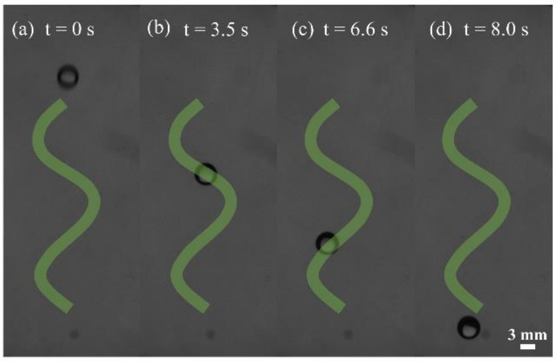

*Figure* - Passive actuation of a water droplets along a wavy illuminated stripe achieved at the surface of LIS/LiNbO3 crystals via light-induced phenomena.

## References

[1] S. Cremaschini et al.,*Trifurcated Splitting of Water Droplets on Engineered Lithium Niobate Surfaces.* ACS Appl. Mater. Interfaces, 24, 16, 4271, 2024

[2] A. Zaltron et al.,*Optofluidic Platform for the Manipulation of Water Droplets on Engineered LiNbO$_3$ Surfaces*. Adv. Mater. Interfaces 9, 2200345, 2022

[3] L. Lucchetti et al., *Light controlled phase shifter for optofluidics*, Opt. Lett. 41, 333, 2016

[4] J. A. Lv et al., *Photocontrol of Fluid Slugs in Liquid Crystal Polymer Microactuators*. Nature, 537, 179, 2016

# Unlocking Single-Particle Multiparametric Sensing: Decoupling Temperature and Viscosity through Upconverting Polarized Spectroscopy

**E. Ortiz-Rivero**[a,b], K. Prorok[c], R. Marin[a], D. Jaque[a,b], , Artur Bednarkiewicz[c], P. Haro-González[a,b].

[a] Nanomaterials for bioimaging group, Departamento de Física de Materiales, UAM. 28049 Madrid, Spain
[b] Instituto de materiales Nicolás Cabrera, Universidad Autónoma de Madrid, Madrid 28049, Spain
[c] Institute of Low Temperature and Structure Research, Polish Academy of Sciences, ul.Okolna 2, 50–422 Wroclaw, Poland

* elisa.ortiz@uam.com

## Introduction

In biological systems, the interplay between temperature and viscosity is pivotal. Hence, a comprehensive understanding of the dynamics within biological microenvironments requires that both temperature and viscosity are monitored simultaneously and in a remote way, minimizing perturbations to the investigated system. In this context, individual luminescent particles have emerged as prime probes for remote and high-resolution sensing. Among these particles, erbium-doped sodium yttrium fluoride ($NaYF_4$: $Er^{3+}$) upconverting particles (UCPs) stand out for their capability to convert infrared radiation to visible light. Their responsiveness to diverse external stimuli holds promise for leveraging UCPs as remote multiparametric sensors, capable of characterizing medium properties in a single assessment. However, the utility of UCPs in multiparametric sensing is impeded by crosstalk, wherein distinct external stimuli induce identical alterations in UCP luminescence, hindering accurate interpretation and yielding erroneous outputs. Overcoming crosstalk requires alternative strategies in UC luminescence analysis.

To achieve non-invasive and precise control of the UCPs, optical trapping has emerged as a reliable contactless technique, already used for long-term studies of single cells and bacteria. [1, 2] It has been demonstrated that single laser beams can trap, excite and induce rotation of single birefringent UCPs.[3] Its rotation dynamics has been found to be strongly dependent on environmental conditions (e.g., viscosity, temperature, etc.) so that they have been introduced to the scientific community as a potential high-sensitivity sensors.[4, 5]

This study showcases the feasibility of decoupling temperature and viscosity readouts through multiband analysis of luminescence from an optically rotated single UCP.

## Methods

The $NaYF_4$: $Er^{3+}$ microparticles were synthesized by hydrothermal method and dispersed in water at a very low concentration to avoid multiple particle trapping.[3] The solution was introduced into microchannel and placed in a homemade optical trapping setup. A linearly polarized 808 nm, single-mode, fiber-coupled diode laser was used as the optical excitation source. A quarter-wave plate placed afterwards converted the laser beam into circularly polarized light. Optical excitation at 808 nm was selected as it keeps at minimum the laser-induced thermal loading of the rotating UCP and surrounding medium. The $NaYF_4$: $Er^{3+}$ UCPs used here show an intense visible emission when optically excited by 808 nm radiation thanks to a multiphoton excitation process already described elsewhere.[6]

## Result and discussion

The visible emission spectra, after 808 nm laser excitation, of a $NaYF_4$: $Er^{3+}$ UCP is shown in Figure 1b,c. The green emission band, centered around 540 nm, corresponds to the $^4S_{3/2}$ ($^2H_{11/2}$)$\rightarrow$ $^4I_{15/2}$ transitions of $Er^{3+}$ ions, and the red emission band, centered around 660 nm, to the

$^4F_{9/2} \rightarrow ^4I_{15/2}$ transitions of $Er^{3+}$ ions. The two excited states, $^4S_{3/2}$ ($^2H_{11/2}$), are thermally coupled: The ratio of the relative intensities from the “green” emission bands is temperature-dependent. [7] On the other hand, the “red” emission band is polarized thus, viscosity-dependent rotation dynamics can be extracted from examining the fluctuation in the polarization state of a trapped UCP luminescence and its correlation with particle orientation. [8]

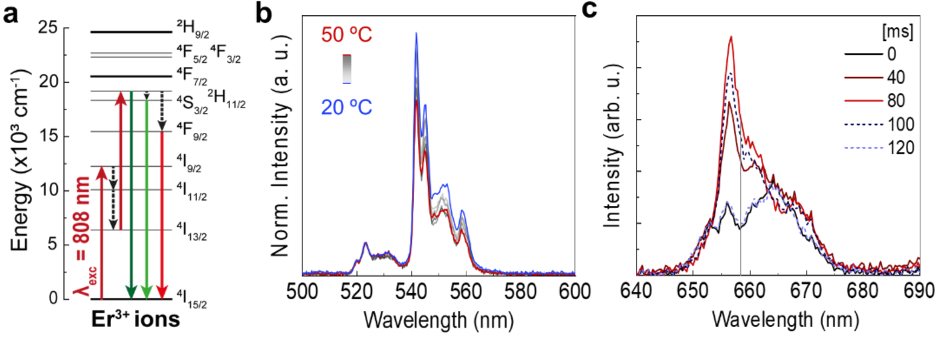

*Figure 1* – a) Energy level diagram of $Er^{3+}$ ions. b) Temperature-dependent green emission spectra and c) orientation-dependent red emission of an optically trapped and rotating $Er^{3+}$-doped UCP.

Finally, we want to demonstrate the capacity of the $NaYF_4$: $Er^{3+}$ UCP for de-coupled local and remote sensing. With that purpose a viscous solution was introduced in the microchannel where a single UCP is trapped and rotating (Figure 2a). The luminescent signal was monitored in real time, and the temperature and viscosity were obtained: the temperature remains constant during the experiment (Figure 2b), and the medium viscosity increased (Figure 2c) up to 4 mPa·s.

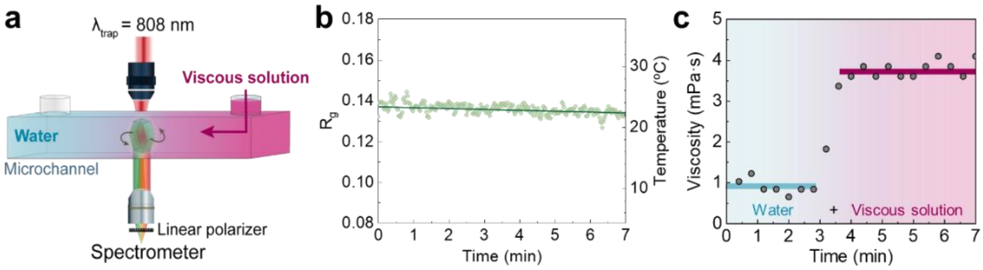

*Figure 2* – a) Schematic representation of a trapped and rotated UCP by a 808 nm laser. After 3 minutes, a viscous solution is introduced. b) Time evolution of the $Er^{3+}$ ions green emission ratio and temperature. c) Viscosity evolution with time.

## Conclusion

We demonstrate a novel strategy to achieve uncoupled and simultaneous temperature and viscosity sensing during a mixture process based on a single upconverting microparticle. Reliable readouts, without the present of cross-talk, of these two parameters are obtained from the analysis of the luminescence of an optically trapped and rotating $NaYF_4$: $Er^{3+}$ UCP. These results could pave the way for new methods to overcome the limitations of current luminescent sensors. For example, it can be relevant for further analysis of bio-systems or temperature-changing events such as in-situ monitoring of reaction processes and other complex mechanisms.

## References

[1]. C.F. Kenworthy et al., *Sci. Rep.*, 11(1), 6873, (2021).
[2]. P Rodríguez-Sevilla et al., *Journal of Materials Chemistry B*, 5(46), 9085, (2017).
[3]. E. Ortiz-Rivero*, et al.*, *Small*, 16(19), e2002055, (2020).
[4]. Y. Arita*, et al.*, *ACS Nano*, 10(12), 11505, (2016).
[5]. Al.. Bishop et al., *PRLs*, 92(19), 198104, (2004).
[6]. M. Wang et al., *Nanomedicine: NBM*, 7(6), 710, (2011).
[7]. D. Jaque & F. Vetrone, *Nanoscale*, 4(15), 4301, (2012).
[8]. J. Kim *et al.*, *Nat. Comm.,* 12(1), 1943, (2021).

## Acknowledgements

This work has been partially supported by the Ministerio de Ciencia e Innovación de España (PID2019 105195RA I00, CNS2022-135495, and TED2021-129937B-I00).

# Deciphering the role of Brownian motion in plasmonic enhancement in single colloidal upconverting nanoparticle

**F. Zhang** [a,*], P. R. Almeida Oiticica [b], J. Abad-Arredondo [c], M. Setsuko Arai [b], O. N. Oliveira Jr. [b], D. Jaque [a], A. I. Fernandez Dominguez [c], A. S. Stucchi de Camargo [d], and P. Haro-González [a]

[a] Nanomaterials for Bioimaging Group (nanoBIG), Universidad Autónoma de Madrid, 28049, Spain
[b] São Carlos Institute of Physics, University of São Paulo (USP),13566-590 São Carlos, SP, Brazil
[c] Condensed Matter Physics Center (IFIMAC), Universidad Autónoma de Madrid, 28049 Madrid, Spain
[d] Friedrich Schiller University (FSU), Jena, 07737, Germany

* Fengchan.zhang@estudiante.uam.es

Upconverting nanoparticles (UCNP) are essential in modern photonics due to their ability to convert infrared to visible light. Their main drawback is the low brightness, owing to the relatively low absorption coefficient of the lanthanide ions and their reduced quantum yield. This drawback can be solved by combining UCNPs with plasmonic nanostructures (PNSs). Plasmon-enhanced upconversion has been widely demonstrated in dry environments, where upconverting nanoparticles are immobilized so that the UCNP−PNS distance is controlled and fixed. Nevertheless, the situation becomes more complex if UCNPs are suspended in an aqueous medium. Brownian motion can introduce continuous fluctuations in the UCNP−PNS distance, competing with plasmon-enhanced luminescence.

In this study, we employ optical tweezers (OTs) for 3D manipulation of an individual UCNP in the proximity of Au plasmonic nanoparticles (PNPs), enabling the exploration of plasmon-enhanced upconversion luminescence in water. A continuous-wave 980 nm laser beam is focused within a microchamber containing the colloidal dispersion of UCNPs to create the optical trap and excite the upconverting luminescence. The base of the microchamber is a glass substrate deposited with Au PNPs. The magnitude of plasmon-enhanced luminescence in a single UCNP as a function of OT−PNS distance was studied. There are two differences between our results and those reported for static UCNP-PNPs systems. First, the plasmon-induced enhancement is moderate (20%). Second, our results arise from a long-range effect, extending up to UCNP-PNP separations as large as 1 μm. Comparison between experimental and numerical simulations evidence the key role of Brownian motion in limiting the plasmon-enhanced luminescence. The three-dimensional Brownian fluctuations of the upconverting nanoparticle leads to an “average effect” that explains the magnitude and spatial extension of luminescence. The findings contribute to the understanding of the complex interplay among plasmonic effects, optical trapping, and Brownian motion in colloidal systems.

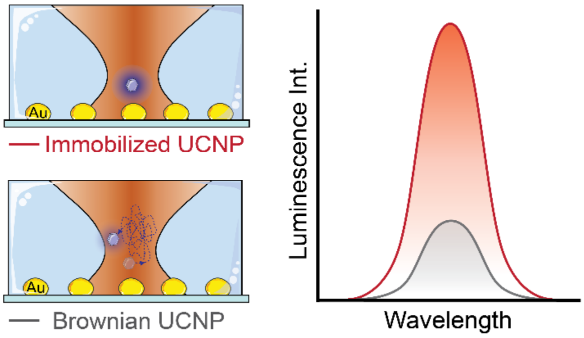

*Figure* – Different plasmon-enhanced luminescence between immobilized UCNP (simulation) and colloidal UCNP subjected to Brownian motion.

## References

[1] Qin, X. et al. Surface Plasmon–Photon Coupling in Lanthanide-Doped Nanoparticles. The Journal of Physical Chemistry Letters, 12, 1520 (2021).

## Acknowledgments

Financed by Grant TED2021-129937B-I00, CNS2022-135495, and PID2023-151078OB-I00, funded by MCIN/AEI/ 10.13039/501100011033 and by the “European Union NextGenerationEU/PRTR.

# Microscale Optical Forces: Exploring Size and Electrostatic Influences

**A. Dávila [a]**, L. Labrador-Páez [b], P. Haro-González [a,c]

[a] Departamento de Física de Materiales, Universidad Autónoma de Madrid, Madrid 28049, Spain.
[b] Departamento de Química Física, Universidad Complutense de Madrid, Madrid 28040, Spain.
[c] Instituto Nicolás Cabrera, Universidad Autónoma de Madrid, Madrid 28049, Spain.

* ana.davila@uam.es

Optical tweezers (OT) are a widely used tool in fields such as biology and physics as they facilitate the manipulation of nanometer and micrometer elements. Most of the particles used in optical tweezers (OT) with a biological interest usually have a micrometer radius, as well as being manipulated with lasers in the infrared range.

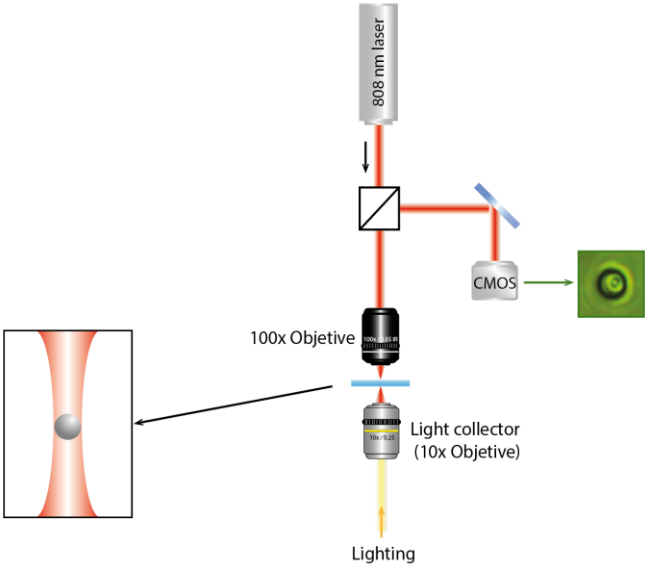

Figure 1. Optical trapping set-up using a infrared laser (808 nm).

Such particles lie in between the Mie Regime and the Rayleigh Regime (**$R \sim \lambda$**), but neither is an accurate model for particles in the 1 to 10 micrometer range [2]. Furthermore, the optical forces acting on dielectric microparticles have only been related to parameters such as volume, and size has traditionally been identified as a key parameter, but it has now been found that electrostatic properties could be an important factor to consider [1].

The aim of this work is to design a set of experiments that aim to test which parameters and properties are relevant when trapping a dielectric microparticle.

For this, particles of different materials with a size of 2 microns have been chosen, among which are: PMMA, silica, oil, and polystyrene (PS). To achieve the objective of this work, the optical force of each particle has been measured, thus calculating the trapping constant that characterizes them. In addition, as mentioned above, the electrostatic properties can be an important factor to consider, so the zeta potential of the particles has also been measured.

Also, the optical force of silica particles at different sizes has also been measured.

Using all these parameters, and taking into account others, such as size, in this work we compare them with the aim of finding out how they are related, and if it is possible to find any trend between them. In this way, we will be able to define the parameters to be consider important when a particle is located between the Mie Regime and the Rayleigh Regime.

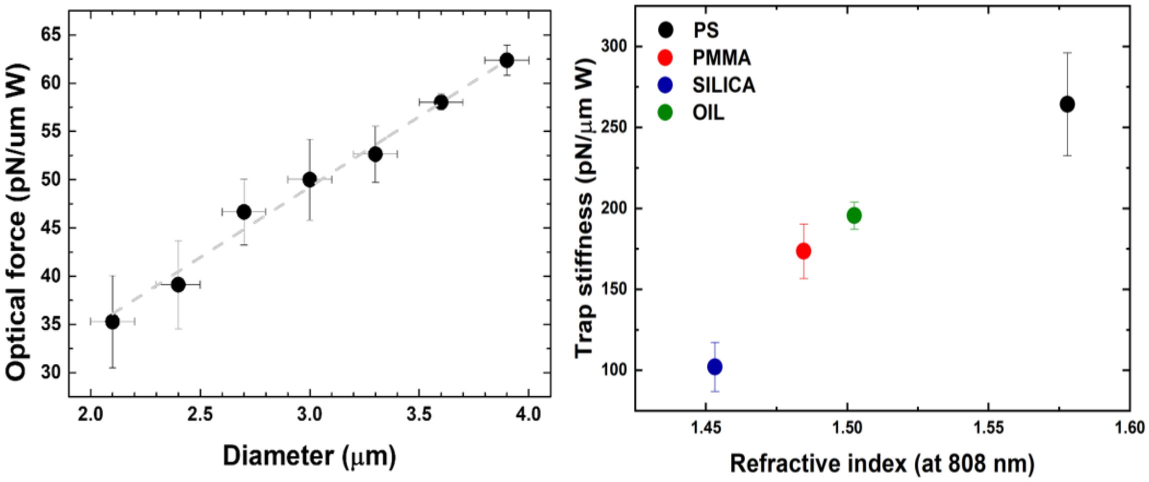

Figure 2. a) Optical force as a function of the diameter of particles. b) Refractive index, using a 808 nm laser, dependence of the trap stiffness calculated for the particles trapped.

This work was financed by Grant TED2021-129937B-I00, CNS2022-135495, PID2020-116192RB-I00 and PID2023-151078OB-I00 funded by MCIN/AEI/10.13039/501100011033 and by the “European Union NextGenerationEU/PRTR

**References**

[1] Rodríguez-Sevilla, Paloma, et al., Phys. Rev. Lett., 18.1, 602 (2018)

[2] W.H. Wright, G.J. Sonek and M.W. Berns, Phys. Rev. Lett., 63, 715 (1993)

# Submicro patterning in $LiNbO_3$ by Fe ion implantation for the assessment of novel type of photovoltaic optoelectronic tweezers

**S. K. Padhi** [a], G. Y. Jia [b,a], F. Valls-Vicent [c,a], C. Sebastián-Vicente[d], A. García-Cabañes [d], J. Olivares [c,a]

[a] Centro de Microanálisis de Materiales (CMAM), UAM, 28049-Madrid, Spain
[b] School of Materials Science and Engineering, Taiyuan University of Science and Technology, Taiyuan 030024, Shanxi, China
[c] Instituto de Optica "Daza de Valdés", CSIC (IO,CSIC), 28006-Madrid, Spain
[d] Dpto. de Física de Materiales, UAM, 28049-Madrid, Spain

* santanu.padhi@uam.es

In the last years, photovoltaic optoelectronic tweezers (PVOT) have emerged as a versatile multi-functional tool for a large variety of applications in different fields, such as optical manipulation and trapping of nano-objects [1], optofluidics [2], plasmonics [3] or biotechnology/biomedicine [4], to cite a few. The technique is based on the bulk photovoltaic effect. It is a singular phenomenon that appears in a few crystalline ferroelectric materials ($LiNbO_3$ clearly standing out) when properly doped (mainly Fe). By default, the available iron-doped $LiNbO_3$ crystals (Fe:LN) are homogeneously doped in bulk format. In addition, these crystals are much more expensive than the nominally pure LN.

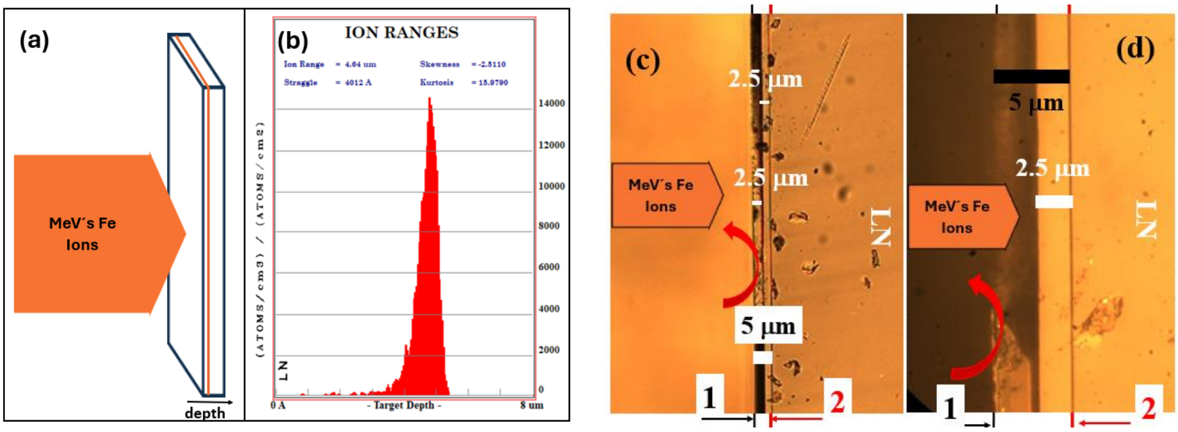

*Figure 1* – (a) Schematic 3D drawing, not to scale, for generating Fe doped lines (of mm-cm length) of submicron thickness by Fe implantation in a standard pure LN sample; and then using the polished perpendicular surface to the ion-implanted surface to study the PVOT performance. (b) SRIM calculations show the depth profile of the implanted Fe ions for the case of 24 MeV Fe ions. Most ions are implanted and concentrated in a thin layer of < 500 nm thickness. Fe implantation line images acquired by using optical microscopy image at magnification: (c) 10 X and (d) 100 X, respectively. The black label "1 (a continuous thin vertical black line placed below the image)" indicates LN crystal edge, and the red label "2" (continuous thick vertical red line placed below the image) indicates the Fe implanted layer beneath LN crystal edge. Also, a curved red arrow away from the crystal edge was included to indicate crystal surface fragility and layer-by-layer removal.

According to the Stopping and Range of Ions in Matter (SRIM) simulation program, the expected implantation depth is 4.6 µm for 24 MeV Fe ion irradiation. The red label "2" mark is the Fe ion implantation line observed in the optical microscope and is shown in figure 1.

Further, in-situ annealing was carried out during Fe ion irradiation. This prevents damage/disorder accumulation from taking place at the first few microns beneath the surface [5]. Moreover, the Fe - implanted surface is fragile, and layer-by-layer loss or removal was noticed. A significant thickness of about 2.5 µm was lost during the characterization and handling processes. For the nanoparticle trapping experiment, a portion of the crystal having the Fe implanted line approximately 2.5 µm beneath the crystal edge was utilized.

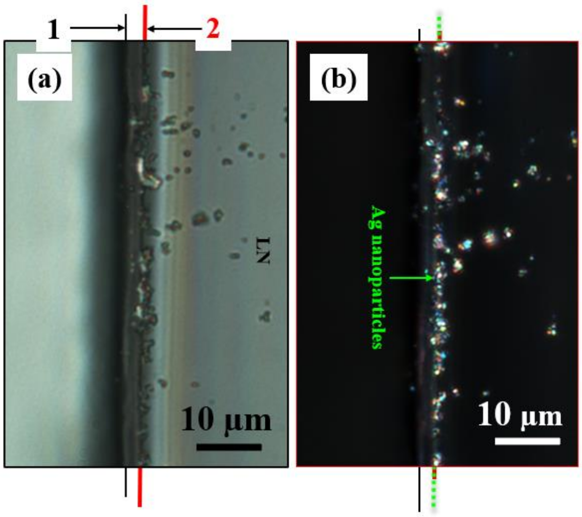

*Figure 2* – One-dimensional (1D) array of trapped Ag nanoparticles in optical microscopy images. (a) Image acquired in transmission bright-field mode: the black label “1” (a continuous thin vertical black line placed below the image) indicates LN crystal edge, the red label “2” (continuous thick vertical red line placed below the image) indicates the Fe implanted layer beneath LN crystal edge. Meanwhile, the corresponding image in (b) with crossed polarizers in reflection mode indicates that 1D trapped Ag nanoparticles have brighter features. A vertical round dotted green line, placed above the red label “2,” represents a guide to the eye to highlight the 1D dielectrophoretic arrangement of Ag nanoparticles.

Figure 2 illustrates photovoltaic optoelectronic tweezers (PVOT) performance. A suspension of Ag nanoparticles (with an average diameter of about 100 nm) were dispersed in n-heptane, with a concentration of 200 mg/L. The following experimental procedure was followed for photovoltaic particle trapping on the Fe-implanted $LiNbO_3$ crystal: (1) The LN crystal was homogeneously illuminated using a white-light source, with an intensity of 900 mW/cm$^2$ and an exposure time of 5 minutes. Subsequently, the crystal was immersed in the Ag nanoparticles suspension for 5 seconds and extracted. (2) The extracted crystal was gently swiped with a lens-cleaning tissue to remove n-heptane residuals and the Ag nanoparticles that were not firmly attached to the crystal. (3) The crystal was observed using an optical microscope, which illustrates a 1D array of trapped Ag nanoparticles, whose location coincides with the sub-micrometer Fe implanted layer.

In conclusion, we have demonstrated Fe-ion implantation as a new scheme for local doping of $LiNbO_3$ crystals for PVOT. The Fe-implanted samples show signatures of the bulk photovoltaic effect, which could explain the light-assisted 1D trapping of Ag nanoparticles at the position of the Fe layer. These locally doped crystals, with sub-micrometer spatial resolution, could be exploited for the optoelectronic manipulation of micro/nanoparticles.

## References

1. M. Carrascosa, A. García-Cabañes, M. Jubera, J. B. Ramiro, and F. Agulló-López, Applied Physics Reviews **2**, 040605 (2015).
2. L. Chen, S. Li, B. Fan, W. Yan, D. Wang, L. Shi, H. Chen, D. Ban, and S. Sun, Sci Rep **6**, 29166 (2016).
3. I. Elvira, J. F. Muñoz-Martínez, M. Jubera, A. García-Cabañes, J. L. Bella, P. Haro-González, M. A. Díaz-García, F. Agulló-López, and M. Carrascosa, Advanced Materials Technologies **2**, 1700024 (2017).
4. A. Blázquez-Castro, J. C. Stockert, B. López-Arias, A. Juarranz, F. Agulló-López, A. García-Cabañes, and M. Carrascosa, Photochem. Photobiol. Sci. **10**, 956 (2011).
5. M. L. Crespillo, O. Caballero-Calero, V. Joco, A. Rivera, P. Herrero, J. Olivares, and F. Agulló-López, Appl. Phys. A **104**, 1143 (2011).

# Harnessing Plasmon Resonances in Ni and $Bi_2Te_3$ Nanowire Networks for Enhanced Thermoelectric Performance

**Olga Caballero-Calero** [a]*, Alejandra Ruiz-Clavijo [a], Cristina V. Manzano [a], Gaspar Armelles [a], Marisol Martín-González [a],

[a] Instituto de Micro y Nanotecnología, IMN-CNM, CSIC (CEI UAM+CSIC) Isaac Newton, 8, E-28760, Tres Cantos, Madrid, Spain

* olga.caballero@csic.es

Anodic aluminum oxide (AAO) templates were used in template-assisted electrochemical deposition, facilitating the creation of one-dimensional (1D) nanowire arrays with different densities of nanowires per area unit and three-dimensional (3D) nanowire networks composed of Ni and $Bi_2Te_3$. The optical properties of these materials were analyzed using spectroscopic ellipsometry. The results indicate that plasmon resonances are responsible for the distinct optical behaviors observed in both materials. Despite the different origins of the plasmons in each material, the position of the resonances appears to be dependent on the interactions between the nanowires [1]. $Bi_2Te_3$ is a thermoelectric semiconductor capable of converting temperature differences into electrical voltages, while Ni is a magnetic metal. It has been observed that 3D nanowire networks exhibit superior performance compared to films or 1D or bulk configurations [2-3]. In the case of $Bi_2Te_3$ nanostructures, the ability of the plasmon to induce a localized temperature increase can be harnessed to enhance the thermal gradient in these structures, thereby facilitating the fabrication of miniaturized thermoelectric generators, as proposed by other researchers [4]. The confinement of light produced by the plasmon resonance could potentially be used to increase the thermal gradient, resulting in an increase in the final power output.

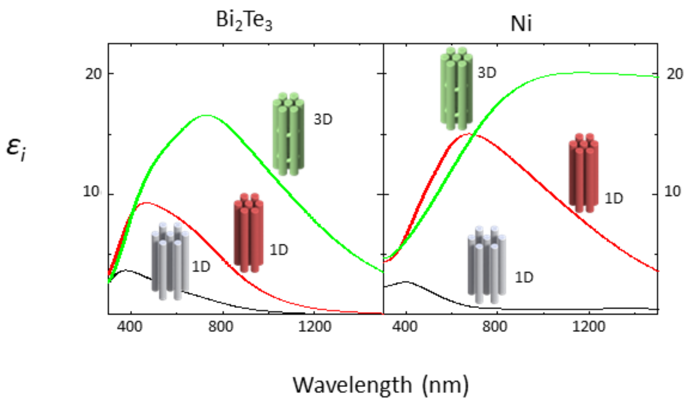

*Figure* – Experimental spectra of the imaginary parts of the in-plane effective dielectric constant of 1D nanowire arrays with 100nm inter-wire distance (black line, scheme in grey), 65 nm inter-wire distance (red line, scheme in red) and 3D nanowire-networks (green line, scheme in green) for $Bi_2Te_3$ (left) and Ni (right).

## References

[**1**] O. Caballero-Calero, A. Ruiz-Clavijo, C.V. Manzano, M. Martín-González, G. Armelles, Nanomaterials, 13, 154 (2023).

[**2**] A. Ruiz-Clavijo, O. Caballero-Calero, C.V. Manzano, X. Maeder, A. Beardo, X. Cartoixà, F.X. Álvarez, M. Martín-González, ACS Applied Energy Materials, 4, 13556 (2021).

[**3**] A. Ruiz-Clavijo, S. Ruiz-Gomez, O. Caballero-Calero, L. Perez, M. Martin-Gonzalez, Physica Status Solidi (RRL)–Rapid Research Letters, 13 (2019) 1900263.

[**4**] K.W. Mauser, S. Kim, S. et al., Nature nanotechnology, 12, 770 (2017).

# Three-dimensionally nanostructured waveguides inside optical crystals for on-chip instrumentation by fs-laser nanolithography

F. Paz-Buclatin[a], P. Molina[b], G. Martín[c], and A. Ródenas[a,d]

[a] Departamento de Física, Universidad de La Laguna (ULL), San Cristóbal de La Laguna, Tenerife, Spain
[b] Departamento de Física de Materiales, Universidad Autónoma de Madrid (UAM), Madrid, Spain
[c] Université Grenoble Alpes/CNRS, IPAG, F-38000 Grenoble, France
[d] Instituto Universitario de Estudios Avanzados en Física Atómica, Molecular y Fotónica (IUDEA), Universidad de La Laguna (ULL), San Cristóbal de La Laguna, Tenerife, Spain

* arodenas@ull.edu.es

Optical waveguiding inside high quality optical garnet materials, such as sapphire and yttrium aluminum garnet (YAG), transparent from the UV (250 nm) to the mid-IR (5 µm), has great application for on-chip sensing instrumentation [1], such as harsh-environment resistant spectrometers, beam combiners for on-chip interferometry [2], and others. Besides sensing and spectral characterization, optical gain and laser generation is also a well-known application of doped sapphire and YAG crystals, with tunable emission from 750 to 1000 nm in the case of Ti:Sapphire, and high efficiency emission at laser lines of 946, 1030, 1064, 1319, 2010, 2080, 2900 and 2940 in the case of YAG doped with rare earth ions $Nd^{3+}$, $Yb^{3+}$, $Tm^{3+}$, $Ho^{3+}$, and $Er^{3+}$, for example, for which single and multimode laser-written waveguides were already seminally demonstrated a decade ago [3]. Coherent light generation in the form of supercontinuum is also a well-known application, for which no crystal doping is needed, but a precise control of the waveguide dispersion as well as of optical losses is required, for which the standard low index-contrast and low spatial precision laser-writing technique is not sufficient [3].

To achieve all of the above mentioned concepts on a single chip, we have recently developed a novel type of 3D embedded optical waveguides whose mode confinement and properties control is based on the sub-wavelength nanostructuring of the optical crystals such as sapphire and YAG, with 10 nm precision and high index contrast of air-to-dielectric [4, 5]. Our concept unifies the fields of nanophotonics with that of solid-state optics for the first time in a three-dimensional architectural design framework.

In this talk we will present the basics of our technique and we will showcase recent results on telecom waveguides design and fabrication, towards application on on-chip metrology instrumentation and integrated laser sources.

## References

[1] Martin, G., et al. "Development of a 3D ultrafast laser written near-infrared spectro-interferometer." Optics Letters 48.9 (2023): 2253-2256.
[2] Ródenas, Airán, et al. "*Three-dimensional mid-infrared photonic circuits in chalcogenide glass*." Optics Letters 37.3 (2012): 392-394.
[3] Ren, Yingying, et al. "Mid-infrared waveguide lasers in rare-earth-doped YAG." Optics Letters 37.16 (2012): 3339-3341.
[4] Ródenas, Airán, et al. "*Three-dimensional femtosecond laser nanolithography of crystals.*" Nature Photonics 13 (2019): 105-109.
[5] Paz-Buclatin, Franzette, et al. "*Circularly symmetric nanopores in 3D femtosecond laser nanolithography with burst control and the role of energy dose*." Nanophotonics 12.8 (2023): 1511-1525.

# Dimensional analysis of Kukhtarev equations for the photorefractive effect

**A. Alcázar**, A. Méndez, J.B. Ramiro

Departamento de Mecánica de Fluidos y Propulsión Aeroespacial, ETSIAE, Universidad Politécnica de Madrid, Madrid, Spain

* a.alcazar@upm.es

This study conducts a dimensional analysis of the Kukhtarev equations governing the photorefractive effect at low light intensity [1], While numerous studies have explored this phenomena [2], the dimensional analysis offers a unique perspective on the underlying physics governing the process. By applying dimensional analysis techniques [3], the equations are scrutinized to identify key dimensionless parameters that govern the photorefractive effect. This systematic examination aims to elucidate the fundamental non obvious relationships between various physical quantities involved in the process.

In parallel configuration, estimates are made for the diffusion length and local oxidation ratio. In perpendicular configuration, superficial diffusion of charge occurs, and there are chances of donor depletion. Simple dependencies are obtained for photoionization cross-section, recombination rate, carriers mobility, and time evolution. More complex dependencies are found for center density, photovoltaic length, and pattern size.

## References

[1] N. V. Kukhtarev , V. B. Markov , S. G. Odulov , M. S. Soskin & V. L. Vinetskii, Ferroelectrics, 22:1, 949-960 (1978)

[2] F. Agulló-López, G. Calvo, and M. Carrascosa, Springer Series in Optical Sciences, 113, 43-82 (2006)

[3] E. Buckingham, Physical Review, 4, 345-376 (1914)

# Exploring the electric charge of tumour spheroids through their manipulation on photovoltaic ferroelectric platforms

**E. Rincón** [1], P. Camarero [1,2], Á. Mendez[3], M. Quintanilla [1,2], P. Haro-González [1,2], M. Carrascosa [1,2] and Á. García Cabañes [1,2]

[1] *Departamento de Física de Materiales, Universidad Autónoma de Madrid, Madrid 28049, Spain*
[2] *Instituto Nicolás Cabrera, Universidad Autónoma de Madrid, Madrid 28049, Spain*
[3]*Departamento de Mecánica de Fluidos y Propulsión Aeroespacial, ETSIAE, Universidad Politécnica de Madrid, Madrid, Spain*

* esther.rincona@estudiante.uam.es

Electrical charge is a key factor in the behavior of biological systems, as it determines the interaction with external factors, such as surrounding molecules or surfaces [1]. For this reason, physical methods to manipulate and characterize biological systems are increasing every day. Recent studies suggest that cancer cells are negatively charged on their surfaces [2]. Thus, net charge could be used to diagnose tissues. These studies, still limited, are mainly applied to the study of single cells although 3D tissues may exhibit different behaviors. Over the past few decades, 3D cell culture has been developed to prepare multicellular spheroids. This 3D cultures have cellular metabolism and cell-cell interaction closer to those of tissues, thus are used as a middle point between *in vivo* and *ex vitro* biological assays [3].

Optoelectronic photovoltaic tweezers have recently emerged for the manipulation of micro- and nano-objects [4]. This technique is based on the bulk photovoltaic effect (PVE), taking advantage of the light induced electric fields generated in some ferroelectric crystas, being particularly strong in $LiNbO_3$:Fe (LN:Fe) [5]. Because of their non-centrosymmetric lattice, as the crystal is illuminated, carriers from donor impurities are excited along the crystal's polar axis (*c* axis), resulting in a photo-current density. This charge separation gives rise to a bulk photovoltaic (PV) electric field $\boldsymbol{E_{PV}}$ inside the ferroelectric crystal, which extends outside as an evanescent field. This evanescent field will interact with objects near the ferroelectric's surface [6]. If the objects are not charged, they will undergo dielectrophoretic (DEP) forces $\boldsymbol{F_{DEP}}$, and charged objects will undergo both DEP and electrophoretic (EP) $\boldsymbol{F_{EP}} = q\,\boldsymbol{E_{PV}}$ forces, $q$ being the object's charge.

Recently, a method to manipulate aqueous solution droplets have been developed [7]. In this method, the ferroelectric surface is submerged in a non-polar liquid. Above it, the micro-droplet moves inside the liquid, hanging from the liquid-air interface. Particularly, it has been applied to droplets containing homogenously dispersed bio-material, such as DNA and sperm [6]. The analysis of the droplet's migration kinetics allows for the determination of the electrical forces acting on the droplet and the characterization of some droplet's properties, such as the bio-content concentration [6].

In this work, we report the application of this method to the manipulation and characterization of droplets containing a single multicellular spheroid. This hybrid system is composed of a single multicellular spheroid suspended inside a cell culture medium droplet, as it can be seen in Figure 1(a). Two cell lines of human cancer have been used: MCF-7 (Michigan Cancer Foundation-7) and U-87 MG (Uppsala 87 malignant glioblastoma). The difference between both cells lines lies in their cell joining mechanism. MCF-7 cells form side-by-side junctions, and U-87 MG cells form elongated unions. Therefore, MCF-7 cells form more compact spheroids than U-87 MG cells.

Z-cut LN:Fe crystals have been used as photovoltaic ferroelectric substrates, in which negative/positive charge is accumulated in the +*c*/−*c* faces, respectively (see Figure 1(b)). The LN:Fe crystal is placed at the bottom of a cuvette and covered in paraffin oil, which is then placed at the optic setup. The droplet is pipetted and left hanging at the oil-air interphase a few millimeters over the crystal's surface.

As the LN:Fe crystal is illuminated with a laser beam ( $\lambda = 488\ \mathrm{nm}$ in the case of this work), the PV evanescent field induces electrical forces (DEP and/or EP forces) on the droplet. In general, the electrical force on the hybrid droplet $\boldsymbol{F_{ELhd}}$, as it's shown in Figure 1(b), is $\boldsymbol{F_{ELhd}} = \boldsymbol{F_{DEP}} + \boldsymbol{F_{EP}} = \boldsymbol{F_{DEP}} + \boldsymbol{F_{EPm}} + \boldsymbol{F_{EPs}}$, where $\boldsymbol{F_{EPm}}$ is the EP force acting on the cell culture medium and $\boldsymbol{F_{EPs}}$ the EP force acting on the spheroid. As a result, the droplet starts undergoing a horizontal rectilinear motion towards the light beam (stopping at the illuminated region) or away from it.

In the case of cell culture medium droplets, results show migration towards the light on the *+c* face (negatively charged) and repulsion from the light on the *-c* face (positively charged). These results indicate that the cell culture medium is positively charged. When the cell culture medium droplet contained a single spheroid, either from MCF-7 or U-87 MG cell lines, a change in the behavior was observed compared to the manipulation of cell culture medium droplets. This result points to a net negative charge in the spheroids.

Through experiments of deionized water and cell culture medium droplets, $\boldsymbol{F_{DEP}}$ and $\boldsymbol{F_{EPm}}$ have been measured. With those results, together with experiments on hybrid droplets, $\boldsymbol{F_{EPs}}$ has been obtained. Knowing $\boldsymbol{F_{EPs}}$ and the PV electric field, the spheroids' charge density has been estimated.

Finally, because of the potential biological interest of this technique, viability assays have been carried out with U-87 MG spheroids after manipulation. Results show the spheroids' viability is not compromised by neither the PV evanescent fields nor the illumination by the laser beam.

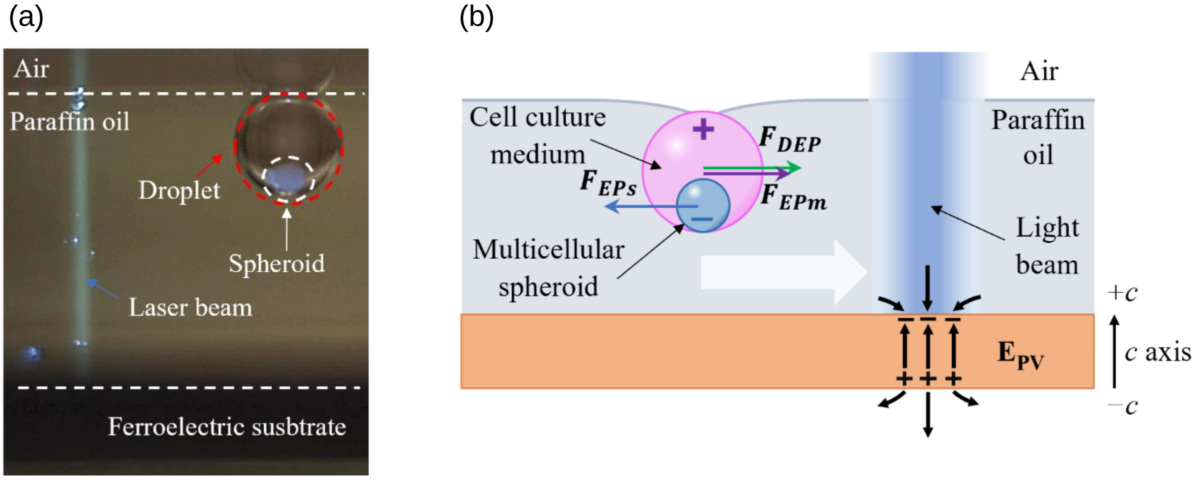

***Figure 1:*** *(a) Schematics of the PV ferroelectric platform showing the hanging droplet containing the spheroid. The ferroelectric substrate is illuminated with a laser beam that generates a PV electric that manipulates the droplet. (b) Schematics of the electrical forces acting on a hybrid droplet manipulated on the +c face. The evanescent PV fields and charges in the LN:Fe crystal are also included.*

This work has been funded by MCIN/AEI/10.13039/501100011033 under the grants PID2020-116192RB-I00, PID2019-110632RB-I00, TED2021-129937B-I00, CNS2022-135495, and PID2023-151078OB-I00.

**References**

[1] G. Caniglia et al., Anal Bioanal Chem **415** (11), 2059 (2023).
[2] L. Wenjun et al., Biophysics Reports **5** (1), 10 (2019).
[3] C. Jensen and Y. Teng, Front Mol Biosci **7**, 33 (2020).
[4] J. Meseguer et al., Eubacteria **34** (2015).
[5] B. Sturman and V. Fridkin, *The Photovoltaic and Photorefractive Effects in Noncentrosymmetric Materials*. Gordon&Breach Science Publishers (1992).
[6] A. Puerto et al., Biomed Opt Express **12** (10), 6601 (2021).
[7] A. Puerto et al., Physical Review Applied **14** (2), 024046 (2020).

# Imprinting micro-patterns of photovoltaic charge onto non-photovoltaic dielectric substrates

**C. Sebastián-Vicente** [a], R. Zamboni [b], J. Imbrock [b], A. García-Cabañes [a], M. Carrascosa [a]

[a] Departamento de Física de Materiales and Instituto Nicolás Cabrera, Universidad Autónoma de Madrid, c/ Francisco Tomás y Valiente 7, 28049 Madrid, Spain
[b] Institute of Applied Physics, University of Münster, Corrensstraβe 2, 48149 Münster, Germany

* carlos.sebastian@uam.es

*Abstract* – Unlike metals or semiconductors, dielectric materials allow for the storage of electrostatic charge patterns for long times thanks to their low electrical conductivity. These charge patterns have many applications: electrostatic assembly of micro/nanoparticles (e.g. laser printers), spatial modulation of wettability, manipulation of liquid droplets, etc. In this context, $LiNbO_3$ is an outstanding platform where one can generate tailored space-charge distributions by optical and/or thermal stimuli, exploiting the bulk photovoltaic effect and/or the pyroelectric effect [1-3]. Here, we demonstrate a novel method for transferring photovoltaic charge patterns from iron-doped $LiNbO_3$ to different passive dielectric substrates, such as glass, quartz, or polymers. Our experimental results establish the foundation of a versatile simple method for electrostatic charge patterning.

## Background of photovoltaic charge printing

Recently, we discovered that electric charge may be transferred from Fe:$LiNbO_3$ crystals to micro/nanoparticles on its surface, either by light or thermal excitation [4,5]. Inspired by these results, we moved one step forward and explored the feasibility of imprinting photovoltaic charge patterns generated in Fe:$LiNbO_3$ onto non-photovoltaic passive substrates. Interestingly, this approach does not require domain-engineered $LiNbO_3$ crystals, in contrast to pyroelectric alternatives [6].

The implementation of the method is straightforward and it resembles the operation of a stamp: 1) first, the Fe:$LiNbO_3$ crystal is illuminated with the desired light distribution, hence producing an electric charge pattern correlated with the light distribution; 2) the crystal is brought into contact for a time $t_c$ with another dielectric substrate; 3) they are separated. As a result, a mirror replica of the original charge pattern is transferred. In this work, the substrates are immersed in n-heptane during the whole process, which has a high breakdown threshold (~$10^8$ V/m) and provides isolation from ambient humidity.

## Experimental results and discussion

To demonstrate and characterize the imprinted charge pattern, we have carried out electrophoretic/dielectrophoretic trapping of micro/nanoparticles. In Figure 1, several proof-of-concept results are illustrated, corresponding to electrophoretic patterns of positively-charged toner microparticles on N-BK7 glass, as well as Fe:$LiNbO_3$ for comparison. We successfully showcase two flexible schemes to print arbitrary charge distributions: serial charge writing by scanning laser beams (Figure 1a-1c) and parallel charge writing by structured illumination (Figure 1d-1g). Both of these approaches allow for arbitrary charge patterns. In both cases, the particle assembly is a faithful reproduction of the light pattern (see Figure 1c, 1f, and 1g), thus proving the existence of a charge replica on the passive dielectric substrate. Similar experiments have been successfully carried out on other passive materials, such as Suprasil quartz, and polyethylene. Furthermore, we have found that the contact time $t_c$ is a key parameter that controls the amount of electrostatic charge on the passive substrate (see Figure 1f and 1g). This strongly evidences that the buildup of printed charge takes place progressively during the contact stage.

Aside from these results, we have also found that the sign of the imprinted charge on the passive substrate is opposite to that of the photovoltaic Fe:$LiNbO_3$ stamp. This might indicate that the underlying physical mechanism could be related to bulk and/or surface screening during the contact stage. Anyhow, further work is necessary to confirm this mechanism.

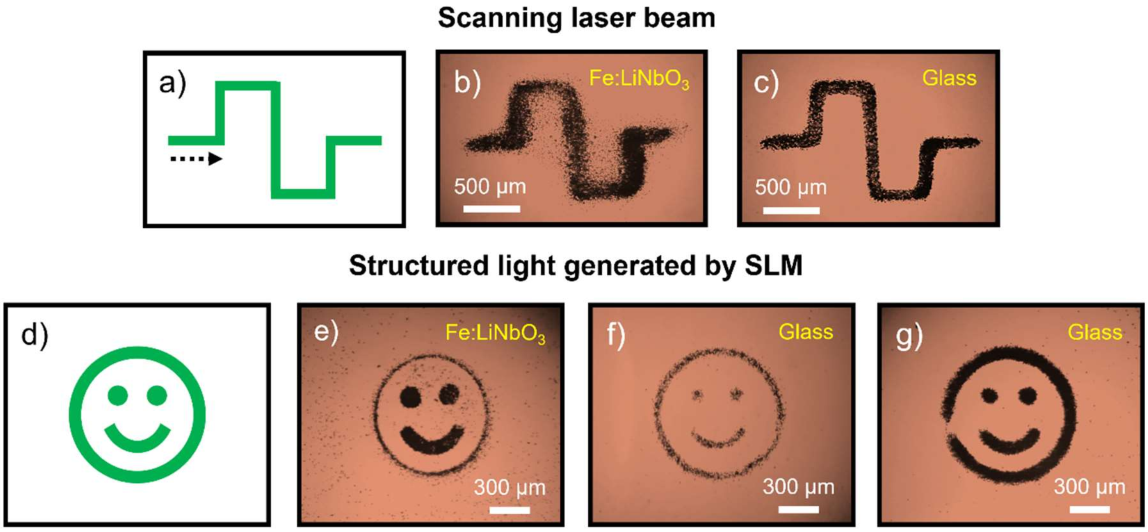

*Figure 1* – a)-c) Experimental results obtained with a scanning laser beam. a) Laser trajectory. The black dotted arrow indicates the scanning direction, from left to right. The scanning speed was 62 µm/s, the beam diameter $d$ = 280 µm, and the light intensity 1 W/cm$^2$. b) Trapping of positively charged toner particles on the +*c* face of the Fe:LiNbO$_3$ stamp. c) Trapping of positively charged toner particles on an N-BK7 glass substrate after contact with the −*c* face of the Fe:LiNbO$_3$ stamp (contact time $t_c$ = 4 min). d)-g) Results obtained with structured illumination. d) Light pattern generated by a spatial light modulator (SLM). The Fe:LiNbO$_3$ crystal was illuminated for 10 min with an intensity of 39 mW/cm$^2$. e)-g) Electrophoretic patterns made of positively charged toner microparticles. Image e) corresponds to the pattern on the +*c* face of a Fe:LiNbO$_3$ crystal. Images f) and g) correspond to the patterns on N-BK7 glass after contact for b) $t_c$ = 5 min and c) $t_c$ = 16 min with the −*c* face of a Fe:LiNbO$_3$ crystal.

## Conclusions

Photovoltaic charge patterns can be transferred upon contact between Fe:LiNbO$_3$ stamps and passive dielectric substrates. The technique is simple, it does not require electron/ion beams or high voltage supplies, and it is applicable to a wide range of materials. The charge pattern can be shaped by moderate light intensities in the entire visible spectrum. Although this work is focused on particle patterning, other applications may be envisaged: manipulation of microfluidic droplets on superhydrophobic surfaces, electrowetting, tailored electro-osmotic flows, etc.

*Acknowledgments* – This work has been funded under grant PID2020-116192RB-I00 by MCIN/AEI/10.13039/501100011033 and grant TED2021-129937B-I00 by MCIN/AEI/10.13039/501100011033 and EU (FEDER, FSE). C. Sebastián-Vicente also thanks financial support through his FPU contract (FPU19/03940). R. Zamboni is funded by a Walter Benjamin position from the Deutsche Forschungsgemeinschaft (DFG, German Research Foundation) – 512630344.

## References

[1] H. A. Eggert, F. Y. Kuhnert, K. Buse, J. R. Adleman, D. Psaltis, *Applied Physics Letters*, *90*, 241909 (2007).

[2] M. Carrascosa, A. García-Cabañes, M. Jubera, J. B. Ramiro, F. Agulló-López, *Applied Physics Reviews*, *2*, 040605 (2015).

[3] R. Rega, J. F. Muñoz-Martinez, V. Pagliarulo, A. Longo, M. Palomba, G. Carotenuto, P. Ferraro, S. Grilli, *Advanced Materials Interfaces*, *8*, 2002216 (2021).

[4] C. Sebastián-Vicente, A. García-Cabañes, F. Agulló-López, M. Carrascosa, *Advanced Electronic Materials*, *8*, 2100761 (2022).

[5] E. Asché, R. Zamboni, C. Denz, J. Imbrock, 2023 IEEE Photonics Conference (IPC), Orlando, FL, USA, pp. 1-2 (2023). DOI: 10.1109/IPC57732.2023.10360764.

[6] R. Rega, O. Gennari, L. Mecozzi, S. Grilli, V. Pagliarulo, P. Ferraro, *Advanced Materials*, *28*, 454-459 (2016).

# Defect related anomalous mobility of small polarons in oxides: the case of congruent lithium niobate

A. Pfannstiel [a], M. Imlau [a,b], **M. Bazzan** [c], L. Vittadello [a,b]

[a] Insitute of Physics, Department of Mathematics, Informatics and Physics, Osnabrueck University, Barbarastrasse 7, 49076 Osnabrueck, Germany
[b] Research Center for Cellular Nanoanalytics Osnabrueck (CellNanOs), Osnabrueck University, Barbarastraße 11, 49076 Osnabrueck, Germany
[c] Università di Padova, Dipartimento di Fisica e Astronomia, Via Marzolo 8, 35131 Padova, Italy

* marco.bazzan@unipd.it

Polarons with strong coupling to the lattice play a major role in the description of optical, electrical, and dielectric properties of ferroelectric oxides. Microscopically, the motion of these quasi-particles occurs through elementary hops among the material lattice sites described by the Holstein theory, while to compute macroscopic transport parameters, such as charge mobility, normal diffusion laws (i.e., via Fick's law) are generally assumed. In this paper, we demonstrate that significant deviations from the used normal diffusion behavior arise if polaron trapping at defects is additionally considered.

As a model system, congruent lithium niobate (LN) is examined enabling electron self-localization both, at regular $Nb_{Nb}^{5+}$ lattice sites and randomly distributed $Nb_{Li}^{5+}$ antisites as so-called free and bound polarons, respectively. At the same time, LN offers a significant wealth of literature information to model polaron transport, including the unambiguous identification of the small polaron localization sites by EPR spectroscopy, the determination of small polaron binding energies by optical spectroscopy, of the electronic energy distribution by ab-initio calculations and of the total hopping time based on (ultra-fast) time-resolved transient absorption spectroscopy. To model polaron hopping, we can describe the lattice distribution of the regular $Nb_{Nb}$ sites by an ordered, cubic-like $Nb_{Nb}$ sublattice, while $Nb_{Li}$ defects represent a disordered antisite sublattice. This constellation leads to a total of four different polaron hopping possibilities that depends on the starting and destination site for carrier self-localization

Here, a formalism is developed that encompasses all these microscopic processes within the framework of a mobile-immobile transport model (MIM) [1] or alternatively, a switching diffusion model (SW) [2], providing expressions for diffusivities, diffusion lengths and mobilities. Starting from the Marcus-Holstein model for the polaron hopping frequency, the diffusion/mobility of different polaron species is verified using a Monte Carlo approach.

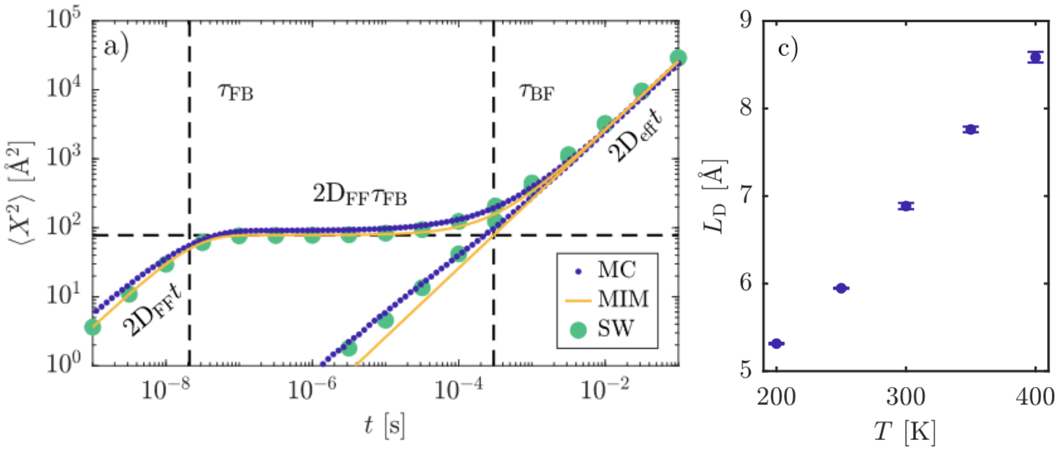

**Figure 1:** (left) Variance (MSD) of the distribution of polarons starting on a $Nb_{Nb}$ site (upper curve) or on a $Nb_{Li}$ site (lower curve) from Monte Carlo simulation (MC), mobile-immobile fit (MIM) and switching diffusion fit (SW). (right) Diffusion length of free polarons as a function of simulation temperature.

Figure 1 (left) shows the mean squared displacement (MSD) of polarons in the congruent crystal from Monte Carlo simulations (MC) and the relative fits by assuming the mobile-immobile (MIM) and the switching diffusion model (SW).The upper curve represents the situation where polarons start its journey as free polaron, while the lower curve shows the situation where polarons start as bound polaron. If the

Fick's law would have been a good description for the system the variance should have shown a linear behavior in the complete time regime. Instead, three distinct transport phases are visible when polarons start as free. Initially, the variance increases linearly. This phase continues until around $10^{-7}$ s, followed by a static phase where transport is nearly halted until $10^{-5}$ s. After this, the diffusion process restarts again, showing again a linear behavior. In the other case, the diffusion begins around $10^{-6}$ s, continuing linearly until $10^{-3}$ s where a slope change is observed. It is interesting to note that in the long-time limit the polaron diffusion, irrespective of starting condition, converges approaching the normality condition. Both, the MIM model and the SW model are able to reproduce the numerical data and these fits reveal diffusion constants of $D_F=1.89\times10^9$ Å$^2$/s and $D_B=7.3\times10^3$ Å$^2$/s for the fundamental diffusivities of free and bound polarons respectively, in good agreement with simulation results for the edge cases of purely free polaron and purely bound polaron transport. Switching rates for the transition from free to bound polaron and vice versa are found as $k_{FB}=3.76\times10^9$ Hz and $k_{BF}=2.14\times10^3$ Hz respectively, indicated with dashed vertical lines in the figure. This overall behavior indicates that in ultrafast time-resolved experiments, the diffusion coefficient is anomalous and time-dependent, however in low-bandwidth or time-integrated experiments the diffusion will appear normal again. Particularly interesting is also the plateau of the MSD curve, which gives information on the diffusion length $L_D=\sqrt{D_F\tau_{FB}}$ of the process. This is shown in Fig 1 (right) as a function of temperature. Its variation from 5 Å to 9 Å over 200 K indicates that free polarons, even at elevated temperatures, move only around 1 to 2 unit cells the before being soft trapped by an $\mathrm{Nb_{Li}}$ defect.

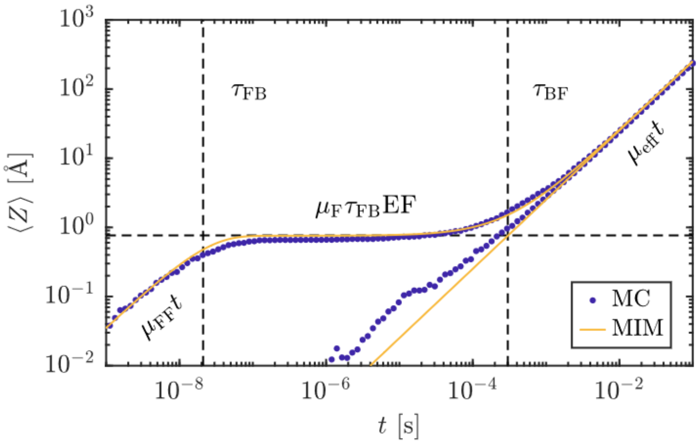

**Figure 2:** First moment of the distribution of small polarons starting on a $\mathrm{Nb_{Nb}}$ site (upper curve) or on a $\mathrm{Nb_{Li}}$ (lower curve) site from Monte Carlo simulation (MC) and mobile-immobile fit (MIM).

Figure 2 shows the average position along $Z$ for polarons starting as free (upper curve) or as bound (lower curve) under the effect of an external electric field of $5\times10^6$ V/m, giving information on the mobility of the system. Also in this case, the behavior should have been linear when Fick's laws would have described correctly the system. Instead, the temporal dynamic is much more rich and the Monte Carlo results can be fitted in a satisfactory way via the MIM model, showing that also an analytical model for the small polaron mobility in the complex environment of congruent LN can be derived.

This overall analysis shows that in the case of a congruent crystal, where mixed free and bound polaron transport is involved, the model expressions of the mobile-immobile and the switching diffusion model provide a better description of the complex dynamic than the normal diffusion laws.

The authors acknowledge funding of the work by the Deutsche Forschungsgemeinschaft (DFG) within the research group "*Periodic low-dimensional defect structures in polar oxides*", FOR 5044, project IM37/12-1.

## References

[1] T. J. Doerries, A. V. Chechkin and R. Metzler, Apparent anomalous diffusion and non-Gaussian distributions in a simple mobile-immobile transport model with Poissonian switching, *Journal of the Royal Society Interface*, **19**, 20220233 (2022)

[2] D. S. Grebenkov, Time-averaged mean square displacement for switching diffusion, *Physical Review E*, **99**, 032133 (2019)

# Small polaron trapping kinetics in iron-doped congruent lithium niobate

Stanislav Fedorenko [a] and **Marco Bazzan** [b]

[a] Voevodsky Institute of Chemical Kinetics and Combustion, Russian Academy of Sciences, - Novosibirsk (Russian federation)
[b] Università di Padova - Dipartimento di Fisica e Astronomia, Via Marzolo 8, 35131 Padova (Italy)

* marco.bazzan@unipd.it

The transport and trapping of small-radius polarons play a key role in the remarkable properties of iron-doped lithium niobate (Fe:LN), which is a widely used material for numerous practical applications, such as integrated and nonlinear optics, optoelectronics, holography, photovoltaics, and oxide catalysis [1]. A standard Fe:LN crystal of a congruent composition contains a large number of point defects, such as vacancies in the lithium sublattice ($V_{Li}$), antisite defects ($Nb_{Li}$), and Fe dopants incorporated at the Li site $Fe_{Li}$. Such defect structure creates conditions for the existence of three types of polarons in the LN lattice [2]: free polarons (F) are formed at regular sites of the niobium sublattice and bound polarons (P) are captured at antisites. In addition, polarons can be stably trapped by the Fe centers.

In Transient Absorption Spectroscopy (TAS) a population of polarons is photo-excited from $Fe^{2+}$ donors and their decay is observed. At a microscopic level, the polarons hop on the lattice sites until a $Fe^{3+}$ trap is encountered and the polaron transforms into a stable $Fe^{2+}$ defect. A formal description of the trapping kinetic from microscopic modelling is therefore very complex and, up to now, could be tackled only by MonteCarlo simulations [3].

We propose here a mathematical approach to the problem leading to analytical solutions to compute the decay of a photo-excited polaron population. Our model considers three types of small polarons, free (F), bound (P) and trapped (T), corresponding to electrons self-localizing at the $Nb_{Nb}$, $Nb_{Li}$ and $Fe_{Li}$ sites. Polarons can move by thermally activated hopping among the different sites with a Marcus-Holstein's jump frequency [4] of the form:

$$W(r_{ij},T) = w_{ij}(T)e^{-2r_{ij}/L_{ij}} \qquad w_{ij}(T) = \left(\frac{\pi}{kT\lambda_{if}}\right)^{\frac{1}{2}}\frac{I_{if}{}^{2}}{\hbar}\exp\left(-\frac{U_{if}}{kT}\right) \qquad (1)$$

Where $i(j) = F, P, T$ are labels indicating the type of initial and final hopping sites: $F$ for polarons sitting on the $Nb_{Nb}$ regular site, $P$ for polarons sitting on an antisite $Nb_{Li}$ defect and $T$ for polarons trapped at the $Fe_{Li}$ site. $r_{ij}$ and $L_{ij}$ are the distance between the hopping sites and a characteristic hopping length specific for the choice $(ij)$. Here, $I_{if}$ is the resonance integral, $\lambda_{if} = E_i + E_f$ is the lattice reorganization energy equal to the sum of the lattice elastic deformation energy in the initial and final states, and $U_{ij} = \left(2E_i + \varepsilon_i - \varepsilon_f\right)^2/4\left(E_i + E_f\right)$ is the hopping barrier equal to the activation energy of the hop from the initial to the final state, $\varepsilon_i, \varepsilon_f$ being additional energies for the Coulomb attraction of impurity centers. For the system under consideration, several of these parameters have been estimated [3].

Next, we treat polarons as "reactants" of a chemical multi-stage reaction:

F + A ↔ P + B, (reversible transformation of free into bound polarons and vice-versa) (2a)

F + T → B + $T_f$, (irreversible trapping of free polarons by Fe traps) (2b)

P + T → A + $T_f$. (irreversible trapping of bound polarons by Fe traps) (2c)

Where A, B and Tf are respectively the concentration of "empty" antisites, regular NbNb sites and Fe3+ traps.

Due to the slow polaron motion, in this kind of reaction the limiting stage is the diffusion towards the reaction zone. Thus the main problem is to determine the rate constants of Eqs. 2(a – c) taking into account the different polaron hopping processes. In our treatment we perform a substantial distinction between the motion of F polarons and the one of P polarons. While the former move by small and fast hops among the regular $Nb_{Nb}$ sublattice, the latter perform rare, long jumps among the disordered lattice of $Nb_{Li}$ antisites. Thus we treat F polarons as normally diffusing particles, and bound polarons as long-hopping particles. By using appropriate theoretical tools [5], this allow us to compute explicitly the rate constants $K_{FT}$ and $K_{PT}$ for eq. 2(b) and 2(c).

Eq. 2(a) is harder to deal with. A first simplification arises from the observation that the reaction is a reversible one, thus at equilibrium it must obey the detailed balance law: $\frac{K_{\mathrm{PF}}(r)}{K_{\mathrm{FP}}(r)} = \exp(\frac{U_{\mathrm{FP}}-U_{\mathrm{PF}}}{k_B T}) = \gamma$. Next, the solution for $K_{FP}$ is found as a complex expression in terms of material parameters, which however can be computed explicitly. From the knowledge of the rate constants, we can compose for the reactions 2 (a – c) the following kinetic equations for the time-dependent survival probability of F and P polarons:

$$\frac{dN_{\mathrm{F}}(t)}{dt} = -K_{\mathrm{FP}}[\rho_{\mathrm{A}} N_{\mathrm{F}}(t) - \rho_{\mathrm{B}} \gamma N_{\mathrm{P}}(t)] - K_{\mathrm{FT}} c N_{\mathrm{F}}(t), \tag{3a}$$

$$\frac{dN_{\mathrm{P}}(t)}{dt} = K_{\mathrm{FP}}[\rho_{\mathrm{A}} N_{\mathrm{F}}(t) - \rho_{\mathrm{B}} \gamma N_{\mathrm{P}}(t)] - K_{\mathrm{PT}} c N_{\mathrm{P}}(t). \tag{3b}$$

Where $\rho_A$, $\rho_B$ and $c$ are the concentrations of empty antisites, empty regular Nb sites and traps, respectively.

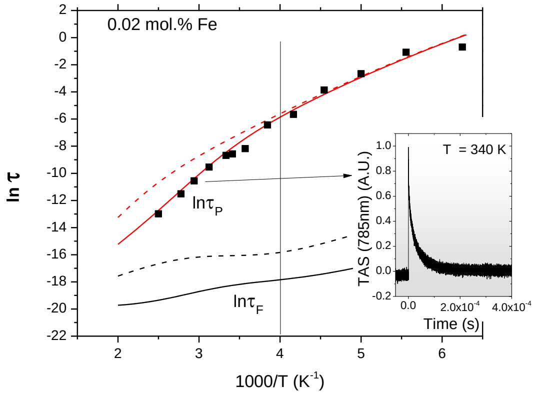

*Fig. 1 Experimental bound polaron lifetimes (black dots) measured by TAS at different temperatures in a 0.02 mol% Fe:LN sample and theoretical calculation (red line). The inset is an exemplary LIA decay.*

The polaron lifetime can be immediately computed by Laplace transforming eqs. (3), obtaining:

$$\tau_{\mathrm{F}} = [cK_{\mathrm{FT}} + \rho_{\mathrm{A}} K_{\mathrm{FP}} (\frac{cK_{\mathrm{PT}}}{cK_{\mathrm{PT}} + \gamma \rho_{\mathrm{B}} K_{\mathrm{FP}}})]^{-1}, \quad \tau_{\mathrm{P}} = \frac{\rho_{\mathrm{A}} K_{\mathrm{FP}}}{cK_{\mathrm{PT}} + \gamma \rho_{\mathrm{B}} K_{\mathrm{FP}}} \tau_{\mathrm{F}}. \tag{4}$$

and compared with experimental TAS data in Fig. 1. As it can be seen a nice fitting can be obtained by refining some poorly known microscopic parameters. In particular here we found: $L_{FF} = 6.4$ Å, $L_{PP} = 4$ Å , $L_{FP} = L_{PF} = 3.2$ Å, $L_{FT} = 4.4$ Å, $L_{PT} = 4.4$ Å. Notice that those parameters cannot change the slope of the curve in Fig. 1, but only shift it in different regions.

## References

[1] Volk, Tatyana, and Manfred Wöhlecke. Lithium niobate: defects, photorefraction and ferroelectric switching. Vol. 115. Springer Science & Business Media, 2008.

[2] Imlau, Met al., (2015) Applied Physics Reviews, 2(4).

[3] Guilbert, L., et al., (2018). Journal of Physics: Condensed Matter, 30(12), 125701.

[4] Holstein, Th., *Annals of physics* 8.3 (1959): 343-389.

[5] Fedorenko, S.G, Russ. J. Phys. Chem. B 18, 210–219 (2024).

# Optical control of ferroelectric liquids on ferroelectric solid substrates

S. Marni[a], R. Barboza[a], A. Zaltron[c], G. Nava[b], T. Bellini[b] and **L. Lucchetti[a]**,

[a] Dipartimento SIMAU, Universita` Politecnica delle Marche, via Brecce Bianche, 60131 Ancona, Italy
[b] Department of Biomedical Science and Translational Medicine, Università di Milano, Via F.lli Cervi 91, 20090 Segrate, Italy
[c] Dipartimento di Fisica e Astronomia G. Galilei, Università di Padova, via Marzolo 8, Padova, Italy

* l.lucchetti@univpm.it

In this talk I will report on the optical control of the electromechanical instability of ferroelectric liquid droplets exposed to the photovoltaic field of a lithium niobate ferroelectric crystal substrate. The ferroelectric liquid is a nematic liquid crystal in which almost complete polar ordering of the molecular dipoles generates an internal macroscopic polarization locally collinear to the mean molecular long axis.

Upon entering the ferroelectric phase, droplets irradiated by an unfocused beam undergo an electromechanical instability and disintegrate by the explosive emission of fluid jets. The regions of jets emission can be controlled by focusing the light beam in areas close to the droplet's edge. Once emitted, the fluid jets can be walked by moving the beam up to millimeter distance from the mother droplet. Reverting the lithium niobate substrate, jets become thinner and show the tendency of being repelled by the beam instead of being attracted, thus offering an additional tool for their optical manipulation. Coating the ferroelectric substrates with fluorolink and decreasing the droplet size, the same focused light beam can be used to obtain optically controlled droplet motion. Ferroelectric droplets are again either attracted toward the center of the beam or repelled, depending on the side of the lithium niobate exposed to light irradiation. Moreover, moving the beam results in walking the ferroelectric droplet over long distances on the substrate.

We understand these effects as due to the coupling between the polarization of the ferroelectric droplet and the polarization photoinduced in the irradiated region of the lithium niobate substrate. Indeed, the effect is not observed in the conventional nematic phase, suggesting the crucial role of the ferroelectric liquid crystal polarization.

The reported results may pave the way to intriguing applications of ferroelectric nematic fluids related to manipulation, actuation, and control of soft, flexible materials.

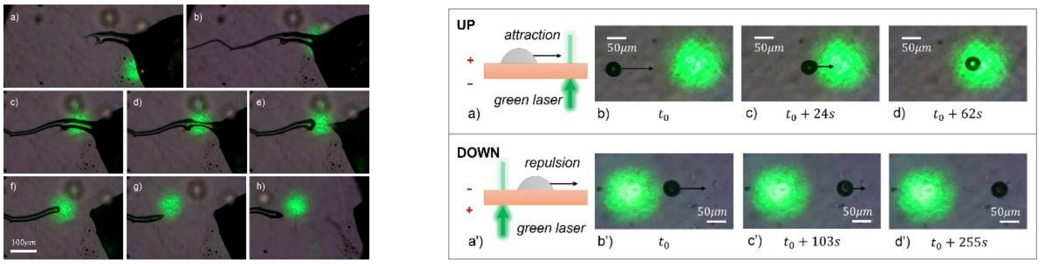

Figure 1: Example of optical manipulation of ferroelectric fluid jets and optical control of ferroelectric droplet motion

## References

[1] R. Barboza et al., Proc. Natl. Acad. Sci. U. S. A., 2022, 119, e2207858119

[2] S. Marni et al., Adv. Mat., Adv. Mater., 2023, 35, 2212067

[3] S. Marni et al., J. Mol. Liq., J. Mol. Liq., 2023, 384, 122287